Università degli Studi di Palermo

AREA RICERCA E TRASFERIMENTO TECNOLOGICO
SETTORE DOTTORATI E CONTRATTI PER LA RICERCA
U. O. DOTTORATI DI RICERCA

Corso di Dottorato di Ricerca in Scienze della Terra e del Mare
Dipartimento di Scienze della Terra e del Mare
Settore Scientifico Disciplinare GEOS-01/C

Invisible Threats: Assessment of Trace Element Contamination and Environmental Impact from a Heavily Industrialized Area. A Statistical Perspective

IL DOTTORE
Federica Lo Medico

IL COORDINATORE
Prof. Christian Conoscenti

IL TUTOR
Prof.ssa Daniela Varrica

CO-TUTORS
Prof.ssa Maria Grazia Alaimo

Prof. Edoardo Rotigliano

CICLO XXXVIII
2025

Index

Abstract

Trace element pollution represents one of the most complex and rapidly growing environmental issues in recent decades. Although these elements are naturally present in the environment as an integral part of geological and geochemical processes, their distribution is also influenced by anthropogenic activities that increase their concentrations in various environmental compartments. The main challenge in assessing environmental contamination is therefore to distinguish between geogenic and anthropogenic contributions. Regulatory limits, defined both nationally and internationally, are generic and poorly representative of local conditions. This highlights the need to define site-specific geochemical baseline values that consider natural variability and local processes. The project presented here fits precisely into this perspective, aiming to develop an integrated methodological framework for defining geochemical baselines in highly complex environmental contexts, where natural and anthropogenic signals tend to overlap and interact. The Valle del Mela district, designated as a Site of National Interest for Remediation (SIN) due to its well-known environmental and health concerns, has been selected as a suitable case study for the development and validation of this approach. The area, in fact, is characterized by the coexistence of two main types of trace element sources. The concentrations of these elements may be ascribable to geogenic sources, linked to the local geology, as well as the role of human activities, primarily of industrial and urban type. These activities have exerted significant pressure on the environment over the years, resulting in a substantial increase in contamination levels. This study employs a multi-matrix approach (water, topsoil, and pine needles) to account for the system's complexity and develop an interpretative model capable of reliably assessing the extent of environmental contamination. The sampling strategy was tailored to the matrix under investigation. In the case of water, planning considered the characteristics of the hydrogeological setting to ensure the representativeness of the sampling points. The study area corresponds to a coastal plain along the Tyrrhenian coastline of eastern Sicily, which is hydrogeological connected to the Peloritani ridge. Sampling of the topsoil layer was planned considering both the lithological variability of the study area and the main wind patterns, which determine exposure to contaminants carried by air masses from the main local emission sources. The same criterion was adopted for sampling Pinus needles, favoring areas located along the prevailing wind directions. Through this sampling framework, which considers the hydrogeological, lithological, and anthropogenic characteristics of the study area, a preliminary identification of samples was carried out into potentially natural and potentially anthropogenic. The elements determined are major elements (Ca, K, Mg, Na, Si), trace elements (Al, As, B, Ba, Cd, Co, Cr, Cu, Fe, Mn, Mo, Ni, Pb, Sb, Se, V, Zn), and Rare Earth Elements (REEs). In this regard, the application of advanced statistical techniques such as compositional data analysis (CoDA) serves as

a tool for interpreting complex environmental data, enabling the identification of potential contamination patterns and the link between specific sources of elements and their concentrations across diverse environmental matrices. Compositional analysis involves transforming data through log-ratio transformations (arl, clr, irl), which can then be appropriately processed with traditional statistical methods, including multivariate techniques. The 79 water samples were analyzed using a clr-biplot, which explained 86% of the total variability. The samples clustered in a region dominated by Ni, Cd, Se, Zn, Cu, Cr, Co, Pb, Sb, Ba, and Mo were classified as anthropogenic, consistent with contamination from industrial and/or traffic-related sources. In contrast, the samples associated with rare earth elements as natural. For the 74 topsoil samples, the clr-biplot explains 68% of the total variability. Samples influenced by anthropogenic sources show stronger associations with elements such as Ba, Cd, Cr, Mo, Pb, Sb, Se, and Zn. In contrast, samples of mainly natural origin tend to close with REEs. The clr-biplot for 40 pine needle samples accounted for 64% of the total variability, the anthropogenic samples were characterized by elements such as Ba, Cd, Cu, Mo, Sb, Se, and Zn, whereas REEs and As dominated the natural group. By comparing the variables that distinguish natural from anthropogenic samples across each environmental matrix, three Compositional Pollution Indices (CPI) were developed. These indices provide a robust measure of anthropogenic pressure, represented through spatial probability maps. The maps created using Sequential Gaussian Simulation (SGS) geostatistical modelling allow for the detection of pollution hotspot clusters within the study area. High CPI values highlighted areas with a strong anthropogenic influence, particularly within the SIN and along the coastline. In contrast, low CPI values marked zones of natural origin, extending towards the western hinterland and along the Peloritani ridge. The Local G test was employed to statistically validate the clusters delineated by the SGS model, confirming that the observed concentrations of high and low CPI values correspond to significant spatial patterns rather than random variability.

The consistency between the Local G map results across the three matrices analyzed and the Pb isotopic data strengthens the reliability of the interpretative model for source discrimination. Therefore, considering the results of Local G for water and topsoil, the samples based on the domains identified as *cold spot* and *hot spot* were divided into two subdatasets, *natural* and *anthropogenic*. To statistically validate these groups, a Sparse Linear Discriminant Analysis (sLDA) was performed. The sLDA returned excellent separation between natural and anthropogenic samples, with accuracies of 83.5% and 78.4% for water and soil, respectively. Local G tests and sLDA analyses for water and soil samples statistically robustly confirmed the distinction between anthropogenic and natural domains, providing a solid basis for defining geochemical baseline values in the water and topsoil matrices. The overlap of Local G test maps for water and soil samples reveals anthropogenic and

natural domains, with a 77% concordance. The domains where a perfect match in the results between water and topsoil are included the SIN area and the coastal strip (anthropogenic area), and in the western sector of the hinterland up to the Peloritani ridge (natural area). The high concordance in these areas provides a solid foundation for establishing the natural and anthropic geochemical baseline values. The Bias-Corrected and Accelerated Bootstrap (BCA) method was used to determine the natural and anthropic geochemical baseline values, using Upper Tolerance Limit 95-95 (UTL95-95).

Two baseline values were therefore defined: a Natural Baseline (NB), and Anthropic Baseline (AB), The resulting baseline values reflect the specific geochemical characteristics of the study area. High NB values of Al, As, Mn, and Sb in water samples, and of Al, As, Mn, Pb, Sb, and Zn in topsoil samples, are consistent with the mineralogical composition of the area. Conversely, higher AB values of Ba, Cr, Cu, Mo, Se, V, and Zn in water samples, as well as of Ba, Cu, Mo, Ni, and V in topsoil samples, indicate anthropogenic inputs.

The comparison between calculated baseline values and proposed national limits revealed significant deviations, highlighting the risk that the use of generic thresholds may lead to biased or misleading interpretations and confirming the importance of establishing site-specific geochemical reference values. The spatialization of elemental concentrations of water and topsoil samples, together with the delineation of baseline values (AB and NB), provides a robust framework for classifying samples that fall outside the concordance domains. For these samples, there is no clear distinction between natural or anthropogenic origins; instead, their categorization is element-dependent.

To assess the contamination status of these blended samples, several contamination indicators were employed, including the geo-accumulation Index (I_{geo}), Enrichment Factor (EF), Contamination Factor (CF), Contamination degree (Cd), Ecological Risk Index (ERI), and Pollutant Load Index (PLI). Natural geochemical baselines were adopted as reference values, ensuring a consistent and site-specific framework for comparison. Overall, the results highlight the presence of potential contamination of hotspots. To evaluate air quality through biomonitoring, enrichment factors (EF) were calculated in pine needle samples. The spatial distribution of EF values revealed contamination hotspots in proximity to major anthropogenic sources for several elements (As, Cd, Cr, Cu, Fe, Mo, Ni, Pb, Sb, V, and Zn). For Cu, Fe, and Zn, however, a possible geogenic contribution linked to the mineralization occurring within the study area cannot be excluded.

Based on the results obtained, the site-specific approach adopted here to determine geochemical baseline values proved effective in preventing biased interpretation. Even in a complex framework, geogenic and anthropogenic sources have been recognized and discriminated.

The study provides a scientifically robust basis to support environmental monitoring strategies, risk assessment procedures, and remediation planning, ensuring that such actions are more precise, targeted, and effective.

This research not only proposes an innovative method but also contributes to establishing a new framework for defining geochemical baselines, coherent with the complex and dynamic nature of contemporary environmental systems. This proposed approach represents a step toward a more integrated, contextualized, and sustainability-oriented applied geochemistry.

1. Introduction

Trace element pollution represents a growing and insidious environmental hazard, posing serious risks to ecosystems and human health in today's industrialized world. Unlike more visible or immediately perceptible pollutants, heavy metals and other trace contaminants can accumulate over time, silently infiltrating soil, water, and food chains, often without apparent symptoms until critical thresholds are reached. Industrial pollution remains a predominant driver of environmental degradation (De Bartolomeo et al., 2004; Landajo et al., 2004; Miró et al., 2004). Despite existing regulatory frameworks (European Union, 2020, 2010, 2000; USEPA, 2024, 1995; World Health Organization, 2017), communities located near industrial zones continue to experience disproportionate exposure to these contaminants (Ordonez et al., 2003). Among the diverse toxicants discharged through industrial processes, heavy metals have emerged as key indicators of contamination due to their stability, persistence, and ability to be reliably analyzed across most environmental media, in contrast to organic pollutants, which are susceptible to biodegradation or chemical transformation into less harmful derivatives (Amiard et al., 1995). The sources of trace elements are primarily anthropogenic, and their presence, distribution, and environmental impact have been central topics in environmental sciences. It is important to note that several metals and metalloids concern human and animal health occur naturally in geological materials. These elements are of relevance in the disciplines of environmental geochemistry and medical geology, where their natural distribution, mobility, and bioavailability are critical to understanding their environmental and health-related impacts. Consequently, the issue is further complicated by the contribution of natural sources-such as geological alteration, volcanic emissions, and sea spray to the background concentrations of potentially toxic elements across various environmental matrices (Bini et al., 2011; Briffa et al., 2020; Cabral Pinto et al., 2017; Cannon et al., 1978; Qiao et al., 2023; Qu et al., 2020). The overlap between natural and anthropogenic inputs poses considerable challenges in accurately determining the provenance of contaminants and in evaluating the true extent of environmental risk. The effectiveness of environmental monitoring relies not only on the quantitative assessment of trace element contamination but also on a comprehensive understanding of the geo-environmental context, which is essential for distinguishing between natural and anthropogenic sources (Gałuszka and Migaszewski, 2011; Kicińska and Turek, 2017; Kowalska et al., 2018). In this regard, the application of advanced statistical techniques serves as a valuable tool for interpreting complex environmental data, enabling the identification of potential contamination patterns and the link between specific sources of trace elements and their concentration across diverse environmental matrices. Therefore, it has become increasingly clear that accurately defining the degree of contamination of a territory requires a deep understanding of the geo-environmental context because environmental reference

thresholds at the national or European level often fail to reflect the specificities of local realities. The most effective method for assessing the contamination status of an area involves acquiring data on the concentration levels of trace elements under conditions free from anthropogenic influences. This approach is particularly applicable in contexts where it is possible to sample environmental matrices that provide a temporal distribution of trace element concentrations, such as sediment cores or cores extracted from glaciers or bedrock. However, in most cases, it is more realistic and operational to refer to the values that define the geochemical background of the area (Matschullat et al., 2000; Reimann and De Caritat, 2017). The concept of geochemical background was first introduced in the context of geochemical prospecting (Hawkes and Webb, 1962). The application of the concept of geochemical background in environmental research has begun to assume an increasingly relevant role in the early 21st century (Gałuszka, 2006, 2007a, 2007b; Matschullat et al., 2000; Reimann et al., 2005; Reimann and Garrett, 2005).

All environmental compartments, air, water, soil, and biota, reflect a complex interaction between natural processes and human activities. Although anthropogenic pollution sources, such as vehicular traffic, industrial plants, and landfills, are often clearly identifiable, distinguishing between anthropogenic contamination and natural background levels remains a complex task. High concentrations of elements can also be of natural origin in areas where geochemically anomalous rock types are present, such as volcanic rocks, metamorphic rocks, or areas with the presence of mineral deposits. Being able to separate the different causes of anomaly found requires, therefore, an in-depth knowledge of the potential sources of contamination (cities, metal foundries, power plants, industries), of the geology and of the dispersion processes of the elements which, together with the use of advanced statistical techniques in the analysis and processing of data, can contribute to the estimation of background values (Ambrosino et al., 2025; Reimann et al., 2018). Determining the natural background levels of trace elements still represents a significant challenge. It is also very difficult to fully exclude the influence of metals and metalloids from pervasive processes like atmospheric deposition, which can introduce exogenous elements into the environment, thereby altering or masking natural geochemical signatures (Albanese et al., 2007; Briffa et al., 2020; Cicchella et al., 2005). Given the increasing need for environmental monitoring and impact assessment, it is essential to introduce and elaborate on the concept of the geochemical baseline, as established in 1993 within the framework of the International Geological Correlation Program through the initiative known as the Global Geochemical Baselines (Galán et al., 2008; Salminen and Gregorauskiene, 2000; Salminen and Tarvainen, 1997). This concept refers to the natural spatial and temporal variation in the concentration of a chemical element within surface environmental media, either in the absence or presence of anthropogenic influence (Santos-Francés et al., 2017).

Accordingly, the geochemical baseline encompasses both the natural geogenic content commonly referred to as the background value, and any anthropogenic contribution that may be present in each environmental sample (Albanese et al., 2007; Cicchella et al., 2005; Frattini et al., 2006; Galán et al., 2008; Salminen and Gregorauskiene, 2000). The determination of the geochemical baseline represents a pragmatic and operationally relevant approach for evaluating the element concentrations, particularly within the context of contemporary global environmental pressures. It serves as a fundamental tool for establishing reference values and quality standards that inform environmental legislation and policy-making (Chen et al., 1999; Facchinelli et al., 2001; Sappa et al., 2020; Wei and Wen, 2012). A critical distinction must be made between two types of geochemical baselines: the natural baseline, derived from samples collected in areas considered free from significant anthropogenic pressures, and the anthropic baseline, which reflects conditions in areas where human activity has altered elemental concentrations. This distinction is essential for accurate interpretation of geochemical data and environmental contamination assessment. The integration of advanced statistical tools combined with spatial analysis techniques provides a highly effective methodological approach in environmental assessment (Charlesworth et al., 2011). This synergy not only enhances the accuracy and reliability of risk evaluations but also supports the development of targeted and efficient management strategies to mitigate impacts caused by potentially toxic elements in environmental media.

The identification of appropriate and scientifically rigorous experimental methods for assessing exposure to metals and metalloids in populations living in complex environmental settings, characterized by both natural geochemical variability and human activities, is the main objective of this study. This necessity arises from the fundamental need to develop analytical and interpretative tools capable of providing accurate, consistent, and comparable assessments of human exposure to environmental contaminants. Such an approach is essential for conducting more reliable risk assessments and for effectively guiding strategies for environmental prevention, mitigation, and sustainable management.

In this context, it is essential to develop a comprehensive, integrated, and systemic understanding of the processes that have historically contributed to, and still cause, environmental degradation across different geographic areas. Achieving this requires a joint analysis of the interactions among the main environmental components that define terrestrial ecosystems namely, air, soil, water, and biota. These components not only reflect the current environmental condition of a system but also actively participate in the contaminant cycle, acting simultaneously as sources, reservoirs, and transporters of potentially toxic elements.

Analyzing the dynamics of contaminant transport, accumulation, and mobilization is essential for understanding how pollutants distribute and persist across environmental compartments. This knowledge is crucial for developing effective, evidence-based strategies to protect human health and support environmental remediation.

This study proposes an integrated operational procedure aimed at providing a detailed characterization of the spatial distribution patterns of trace elements in areas subject to intense anthropogenic pressure. The adopted methodological approach relies on the combined use of environmental matrices, including soils, pine needles, and water, to offer a more comprehensive and multidimensional representation of contamination processes and the dynamics of mobilization and accumulation of potentially toxic elements. The Valle del Mela district, located in north-eastern Sicily, provides a particularly suitable context for the application of environmental geochemical assessments, characterized by the presence of high-impact industrial settlements.

The industrial activities there have caused significant contamination in environmental compartments over time. In 1998, the Italian Government declared the study area to be at high risk of environmental crisis, designating it among the 57 Sites of National Interest (SIN) for environmental remediation (Italian Law n. 426/1998). Furthermore, the area receives several contributions of trace elements linked to the presence of metallic mineral deposits. The topic of this thesis is to develop and refine a methodological approach for assessing the concentrations of metals and metalloids in various environmental matrices, including soil, pine needles, and water, in order to accurately delineate the spatial distribution patterns of trace elements across the study area. Specifically, the study aims to:

I) Discriminate between geogenic and anthropogenic sources of trace elements through multivariate statistical analysis and geochemical indicators.

II) Define site-specific baseline values for the investigated trace elements in water and topsoil samples.

III) Characterize and apportion potential contamination sources using lead (Pb) isotopic ratios as geochemical tracers.

IV) Provide, through this integrated approach, a rigorous scientific foundation for future environmental monitoring programs and remediation strategies, thereby supporting both environmental management and public health decision-making.

2. Materials and methods

2.1. Site description

The Valle del Mela district is in the north-eastern part of Sicily (Italy) and it extends along the Tyrrhenian coast from the small town of Capo Tindari to Villafranca Tirrena, inside delimited by the crest of the Peloritani mountains, between latitudes 38°08'44''N and 38°14'00''N and longitudes 15°02'23''E and 15°26'00''E (Fig.2.1).

Figure 2.1 – Study area. The industrial plant is marked in red, and the boundary of the Site of National Interest for remediation (SIN) is outlined in yellow.

Since the 1960s, the industrial area of Milazzo has been characterized by the development of a wide range of industrial facilities, including an oil refinery, thermoelectric power plants, petroleum product storage terminals, and industrial waste landfills. The high concentration of industrial activities, along with the associated environmental risks, led to the designation of the area in 2006 as one of the 57 Sites of National Interest (SINs) to be remediated, as per Law No. 426 of 1998 (L. 426/1998). Over the years, the refinery has undergone a progressive process of technological modernization, aimed at improving operational efficiency and mitigating polluting emissions. The Milazzo Refinery is still regarded as one of the most significant plants at both the national and international levels. It transforms crude oil into fuels, energy products, and raw materials. With a balanced processing capacity of more than 10 million tons of crude oil per year, it ranks third in Italy in terms of production capacity. A substantial share of finished and semi-finished products is shipped by sea from the oil port of Milazzo.

2.1.1. Geological framework

The Peloritani Mountains represent the southern sector of the Calabro–Peloritan Arc, a segment connecting the southern Apennines and the eastern Sicilian Maghrebid Chain (Bonardi et al., 1980; Ferla et al., 1983; Tortorici, 1982). It is essentially made up of a Paleozoic crystalline basement overlain by Mesozoic–Cenozoic sedimentary successions, emplaced during the Late Oligocene to Early Miocene (Giunta and Nigro, 1999; Lentini and Carbone, 2014). The upper part, known as the ‘‘North Peloritani Complex”, which comprises the study area, consists of two main tectonic units: the Aspromonte Unit, characterized by Hercynian amphibolite-*facies* metamorphic rocks with micaschist, marble, paragneiss, and granite, with intercalated sialic magmatite and carbonate rocks, and the underlying Mandanici Unit, made up of polymetamorphic greenschist-*facies* rocks with graphite–rich phyllite, marble, and micaschist. Marble and micaschist, occurring as bodies or lenses, are interbedded in the main phyllitic complex (Ferla, 2000; Punturo et al., 2005). Tertiary and Quaternary deposits cover most of the whole metamorphic sequence (Bonardi et al., 1980). The coastal sector is made up of Holocene alluvial deposits, reaching a maximum thickness of 90–100 m in the southern part of the Milazzo Peninsula (Carbone et al., 2011). Several polymetallic mineralizations are located within the Mandanici unit, in lithologic packages characterized by marble layers and graphitic schists with intercalations of ankerite [$Ca(Fe,Mg,Mn)(CO_3)_2$], often associated with fluorite, barite, galena, and pyrite. Above, and laterally to the marble layers, Cu–Sb–Ag (As, Ni, and Bi) sulphosalt/sulphide mineralization with traces of Pb, Zn, W, and Au are found in phyllitic bodies (Ferla and Omenetto, 2000). The most abundant minerals are galena, pyrite, chalcopyrite, sphalerite, pyrrhotite, arsenopyrite, the tetrahedrite group of minerals [$(Cu,Fe,Ag,Zn)_{12}Sb_4S_{13}$] and stibnite (Baldanza, 1949). From a geochemical exploration survey conducted on stream sediments was recognisable anomalies for As, Hg, Sb, Zn, and Pb, located in the polymetallic mineralization of the Mandanici Unit and at the tectonic contact with the overlying Aspromonte Unit, prevalently dominated by As–Sb–Hg and Pb–Zn associations (De Vivo et al., 1999). A hydrothermal system has also been recognized along the Tyrrhenian coastline, in the Terme Vigliatore area. The geological framework is reported in Figure 2.2.

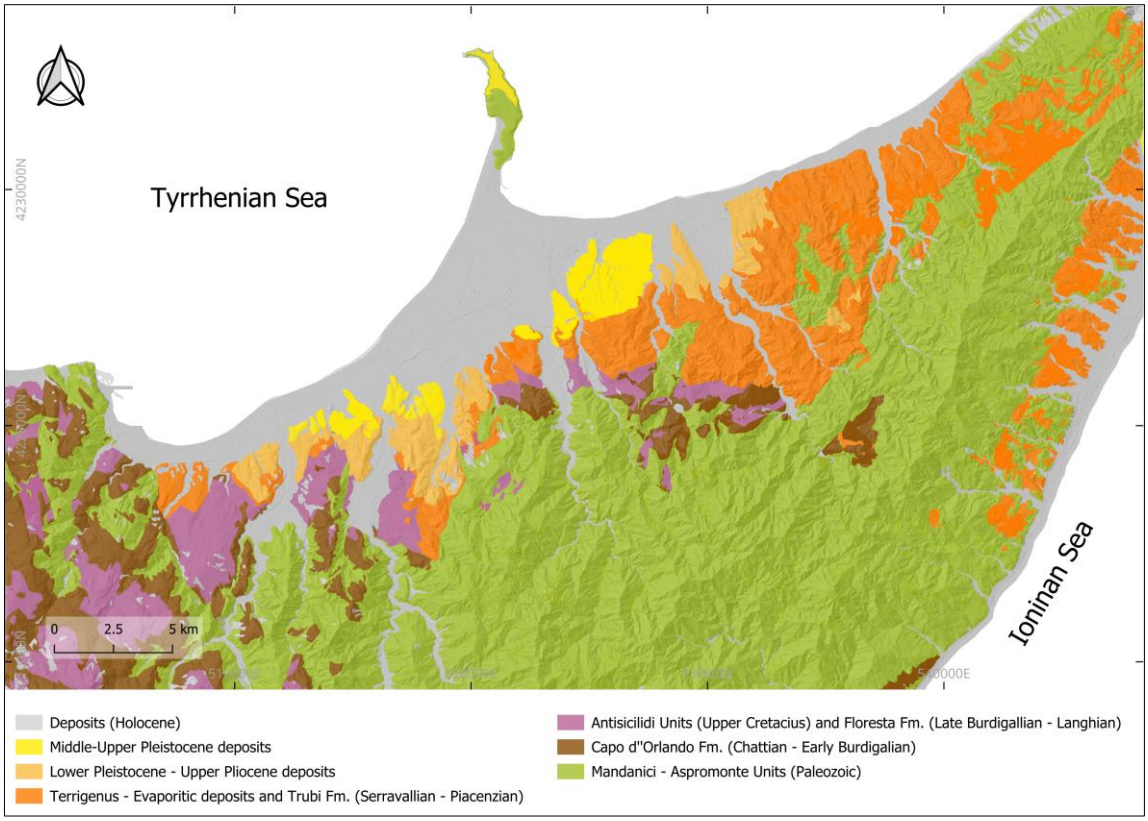

Figure 2.2 – Geological settings (modified from Gasparo Morticelli et al., 2015 and Cangemi et al., 2019).

2.1.2. Hydrogeological Setting

The study area falls on the Tyrrhenian side of the drainage basin of the Peloritan ridge. The hydrographic system of the area consists of torrential watercourses, called "Fiumare", with incisions of an average length of less than 25 km that develop orthogonally to the coastline and the Peloritan ridge and with hydrographic basins of modest size. For several months of the year, the Fiumare are dry due to the low rainfall that characterizes the area's climate. In the rainy season, the flow increases significantly, though for short periods. During intense and concentrated meteorological events, sudden floods of considerable intensity can occur, posing potential dangers to the surrounding inhabited areas. The complex stratigraphic-structural setting that characterize the study area result in heterogeneous hydrogeological conditions, leading to a non-homogeneous distribution of underground water resources. The permeability characteristics detected in the study area are strictly connected to the lithology and structural variations of outcropping soils, which significantly influence both the infiltration processes of rainwater and the dynamics of underground water circulation (Bergallo et al., 1993; Carbone et al., 2023; Coltro et al., 1980; Ferrara, 1987). A differentiation can be recognized, in terms of underground water circulation and presence of aquifers, between the altimetric bands that characterize the study area. In the higher altitude areas, where there is an alternation between metamorphites and terrigenous deposits, permeability is discontinuous, depending on the type and distribution of discontinuities, as well as the degree of surface alteration

of the rocks. The result is the absence of aquifers and a highly fragmented underground water circulation, characterized by a high number of springs with variable and often seasonal flow rates that are strongly dependent on rainfall. In hilly areas, characterized by high lithological heterogeneity, permeability differs in degree and type, resulting in localized underground water circulation within levels or aquifer networks of generally limited extension. In flat areas, where alluvial deposits are consistent, conditions of high permeability due to porosity are found that favor the existence of extensive aquifers and appreciable water resources. The notable lithological variability that characterizes the analyzed territory leads to substantial differences in the distribution of underground water resources.

2.1.3. Climatic setting

According to the Köppen climate classification (Kottek et al., 2006), the study area is categorized as Csa, indicating a Mediterranean climate with dry summers. The Valle del Mela district, although it generally exhibits the characteristics of a maritime Mediterranean climate, along the coast, experiences very hot summers and short, typically mild winters, with precipitation concentrated in the autumn and winter periods. In the more inland areas, winters tend to be colder, while summer temperatures remain largely consistent with those along the coast. Precipitation is predominantly concentrated during the winter months, with the highest values recorded in December (104.6 mm). In contrast, the summer months are characterized by significantly reduced rainfall, reaching a minimum in July (12.4 mm). Mean annual temperatures exhibit maximum values of 27.5 °C in July and minimum values of 12 °C in January (Fig. 2.3a), based on data from the Milazzo meteorological station (Annali idrogeologici: https://www.regione.sicilia.it/istituzioni/regione/strutture-regionali/presidenza-regione/autorita-bacino-distretto-idrografico-sicilia/annali-idrologici).

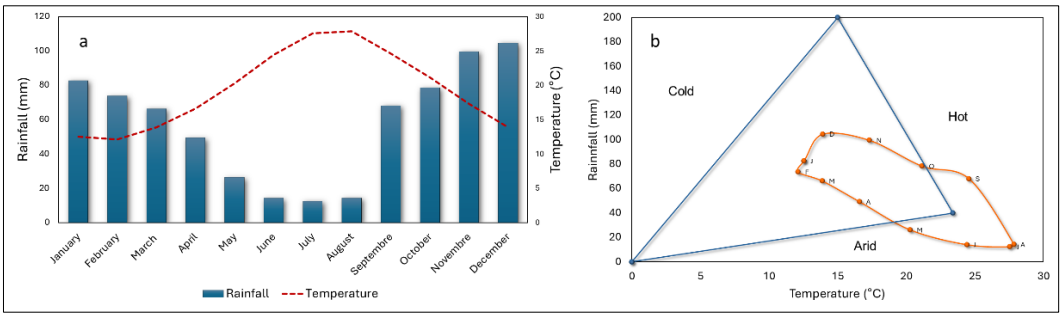

Figure 2.3 - (a) Average monthly precipitation (blue histograms) and temperature (red dashed line) trends in the study area; (b) Peguy climograph, which provides a synthetic representation of the thermo-pluviometric conditions of the study area.

Figure 2.3b presents the Peguy climograph, which provides a synthetic representation of the thermo-pluviometric conditions of the study area. The polygonal shape, formed by connecting monthly average values, illustrates the site's climatic characteristics in terms of both form and scale. The diagram also includes a triangular reference area, defined by Peguy, which distinguishes temperate

climates (within the triangle) from cold, arid, or hot conditions (outside the triangle). The relative position of the polygon to the reference triangle allows for an immediate assessment of the local climate. The graph indicates that from October to April, the area exhibits characteristics of a temperate climate, whereas from May to September, it displays features typical of a hot-arid environment. The wind analysis reveals regime predominantly influenced by local breeze patterns, originating from W-WNW and SSE directions (Fig.2.4). These data provide valuable insights into the dispersion of atmospheric pollutants in the study area.

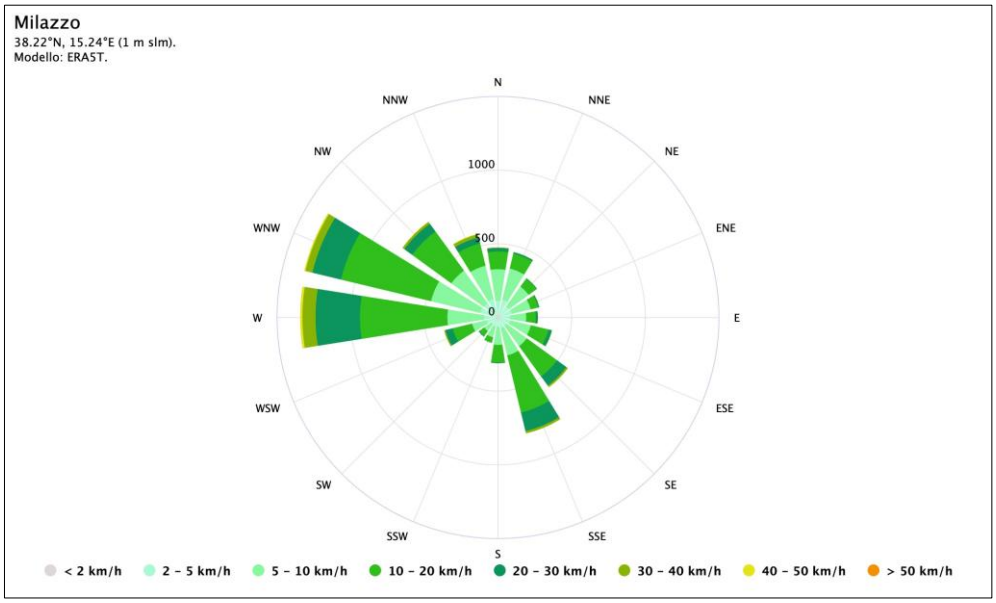

Figure 2.4 - Wind roses of study area. https://www.meteoblue.com/it/tempo/historyclimate/climatemodelled/milazzo_italia_2524155.

2.2.Sampling design and Analytical methods

In order to achieve a comprehensive environmental characterization that encompasses the main environmental matrices, we sampled groundwaters, topsoils, and pine needles (Tab.2.1).

Table 2.1 – Sampling of groundwaters, topsoils, and pine needles.

		Sampling Location
Water samples (79)	PE2-PE11, PE24-PE27 PE61-PE74, PE76-PE79	Peloritani
	PE1, PE12-PE23, PE28-PE60, PE75	Milazzo Plain
Topsoil samples (74)	SP2-SP10, SP26-SP28, SP32, SP44, SP46, SP48, SP49, SP55, SP,62, SP64, SP65, SP67-SP72, SP74	Peloritani
	SP1, SP11-SP25, SP29-SP31, SP33-SP43, SP45, SP47, SP50-SP54, SP56-SP61, SP63, SP66, SP73	Milazzo Plain
Pine needle samples (40)	PN1, PN2, PN8, PN13, PN22, PN23	Peloritani
	PN3-PN7, PN9-PN12, PN14-PN21, PN24-PN40	Milazzo Plain

This multidisciplinary approach was adopted to provide an integrated assessment of quality, considering both abiotic compartments, water and topsoil, and biological indicators, thereby ensuring a holistic understanding of the studied ecosystem.

2.2.1. Water samples

A total of 79 groundwater samples were collected between June and December 2023. Groundwater was sampled from natural springs and private wells in static conditions. The groundwater system of the study area includes a highly permeable coastal alluvial aquifer, connected to two main hydrogeological systems: a shallow aquifer developed in the weathered surface layer of the rocks, and a basal aquifer hosted in the deep fractured portions.

The distribution of water samples is shown in Figure 2.5. All samples were filtered in the field through 0.45 µm Millipore MF filters and stored in new polypropylene bottles, which had been pre-rinsed with HNO_3 and then rinsed with deionized water. Two water samples were collected at each sampling site, one acidified with HNO_3 (1% v/v, ultrapure) immediately after filtration to prevent metal precipitation. The acidified sample was used for cation and trace element analyses, while the non-acidified sample was used for anion and total alkalinity determinations.

Figure 2.5 – Distribution of groundwater samples in the study area. The industrial plant is marked in red, and the boundary of the Site of National Interest for remediation (SIN) is outlined in yellow.

Field measurements included water temperature (T, °C), pH, electrical conductivity (EC, µS/cm), and redox potential (E_H, mV). pH measurements were performed using a glass electrode connected to a VWR pH100 pH meter, calibrated with buffer solutions at pH 4.01 and 7.00. Electrical conductivity was measured with a VWR EC300 instrument, calibrated with the standard conductivity solution

1413 μS/cm. EC values are reported at 25 °C. A SenTix platinum ORP combination electrode, calibrated daily, was used to measure the redox potential.

The main cations and anions, Ca, K, Na, Mg, SO_4, Cl, F, and NO_3, were analyzed through ion chromatograph (930 Compact IC Flex - Metrohm). Total alkalinity was determined, within 24 hours of sampling, in two ways: by titration with 0.01 M HCl using a manual titrator, repeating the measurement three times and using methyl orange as an indicator, and by using the automatic titrator (888 Titrando – Metrohm). Total dissolved solids (TDS) were calculated with the PHREEQCI software (McCleskey, 2018; McCleskey et al., 2012a, 2012b). Silica was determined at Activation Laboratories Ltd. (Ontario, Canada). Trace elements (Al, As, B, Ba, Cd, Co, Cr, Cu, Fe, Mn, Mo, Ni, Pb, Sb, Se, V, Zn) were determined by ICP-MS (Perkin Elmer, Elan 6100 DRC-e), after the addition of internal standards Re–Sc–Y. All standard solutions were prepared with ultrapure deionized water, using ICP Multi Element Standard Solutions XXI CertiPUR standard solutions and Mo and Sb CertiPUR standards (MERCK). The precision of the analytical results was estimated by performing triplicate analyses on every 7th sample, in the range of 1–10% for all the analyzed elements, except for As and Se, which resulted in 12%. The accuracy (±10%) was evaluated using standard reference materials SRM-1640 (groundwater) and TMRAIN-95 (rainwater). The Rare Earth Elements (Y, La, Ce, Pr, Nd, Sm, Eu, Gd, Tb, Dy, Ho, Er, Tm, Yb, Lu) were measured at Activation Laboratories Ltd. by ICP-MS. A total of 12 water samples were selected for isotopic analysis of $^{206}Pb/^{207}Pb$ and $^{208}Pb/^{206}Pb$ ratios. The selection criteria were based on both lithological heterogeneity and spatial distribution, to ensure a representative and comprehensive characterization of the hydrochemical variability within the study area. The Pb isotopic ratios were measured by ICP-MS (Element II, Thermo elemental), at the laboratory of Institut de Physic du Globe de Paris (IPGP), Universitè Paris Cité. Instrumental mass bias was corrected by sample-standard bracketing techniques, using a NBS 981 lead solution as standard every four unknown samples. The intensity ratio correction factor never exceeded 4‰. Solutions were adjusted to produce a signal of about 400,000 cps on the 208Pb isotope (Monna et al., 2000, 1998). The duplicates showed that the $^{206}Pb/^{207}Pb$ and $^{208}Pb/^{206}Pb$ ratio measurements are quite reproducible, considering the analytical precision at 0.1%-0.15%for $^{206}Pb/^{207}Pb$ and $^{208}Pb/^{206}Pb$ ratio, respectively.

The geochemical modelling program PHREEQC (Parkhust and Appelo, 1999), implemented with the MINTEQ.V4.dat database (Allison et al., 1991), was used to calculate the theoretical partial pressure of dissolved CO_2 in water (pCO_2) and the partial pressure of dissolved O_2 in water (pO_2). The calculation of solution speciation and thermodynamic equilibrium conditions of water for the main mineral phases present in the aquifer was determined using the WATEQ4F version 2.0 software (Plummer et al., 1976) and the PHREEQC software. The saturation indices, defined as SI = log

(IAP/Kt), where IAP is the ionic activity product of the mineral-water reaction and Kt is the thermodynamic equilibrium constant at the measured temperature, were calculated using the ionic activities. Thus, an SI = 0 indicates a state of thermodynamic equilibrium, values >0 indicate supersaturation, and values <0 indicate undersaturation.

2.2.2. Topsoil samples

A total of 74 topsoil samples (depth of 0–20 cm) were collected in the Valle del Mela district. The distribution of the samples is shown in Fig. 2.6.

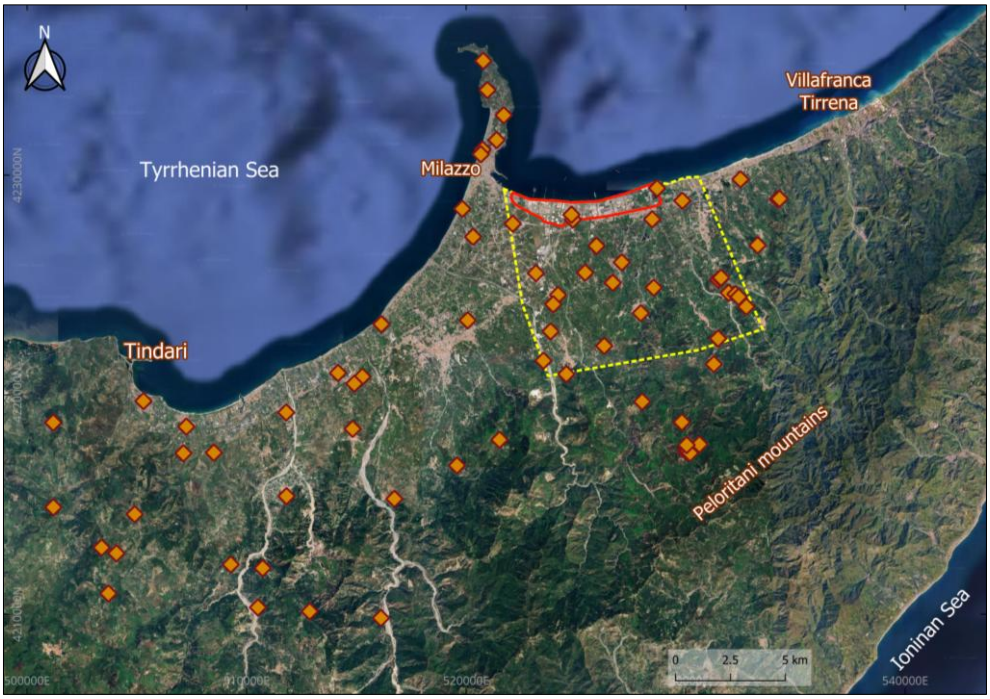

Figure 2.6 – Distribution of topsoil samples in the study area. The industrial plant is marked in red, and the boundary of the Site of National Interest for remediation (SIN) is outlined in yellow.

The samples were collected to ensure adequate coverage across the area, paying particular attention to geological heterogeneity and prevailing wind directions, which influence the dispersion of contaminant plumes from the Milazzo industrial complex. Samples were collected with a plastic scoop, stored in PVC containers, and transported to the laboratory. They were dried overnight at 105 °C in an AG System G- Therm stove. Particle size analysis was conducted according to ASTM D422-63 - Standard Test Method for Particle-Size Analysis of Soils (ASTM Committee D-18 on Soil and Rock., 1963) at the geotechnical laboratory of the Polytechnic Institute of Castelo Branco, Portugal. The method combined grain size analysis through sieving and sedimentation analysis. The gravel-sand fraction was separated using a series of ASTM sieves with mesh sizes decreasing from 2 mm to 0.075 mm. The silty and clay fractions (<0.075 mm) were determined by sedimentation in an aqueous suspension with an anti-flocculating agent, sodium hexametaphosphate. The suspension was left to sit for 16 hours to facilitate disintegration and separation of fine particles, afterwards, the suspension

was brought to a final volume of 1 L with deionized water and transferred into a graduated cylinder. Hydrometer readings were taken at 2, 5, 15, 30, 60, 250, and 1440 minutes after the start of the test. Stones and plant debris were removed, and each sample was sieved through a 500 μm nylon mesh before being ground in an agate mortar. Topsoil analysis was performed at Activation Laboratories Ltd. in Ontario, Canada. The samples were digested using a mixture of 3 ml hydrochloric acid and 1 ml nitric acid. Activation Laboratories automated the digestion process with a microprocessor-controlled hotbox to ensure consistent conditions. The samples were analyzed for elements including Ca, Mg, Na, K, Al, As, B, Ba, Cd, Co, Cr, Cu, Fe, Mn, Mo, Ni, Pb, Sb, Se, V, Zn, Y, La, Ce, Pr, Nd, Sm, Eu, Gd, Tb, Dy, Ho, Er, Tm, Yb, and Lu. The recovery rates for certified elements in standard reference materials (OREAS- 45 d, OREAS- 922, OREAS- 907, OREAS- 263, OREAS − 130, OREAS- 521, OREAS-620, OREAS-610) ranged from 95% to 107%. Analytical precision, evaluated through duplicate analyses of every tenth sample, ranged from 10% to 15% for all elements, except for samarium, which had a precision of 14%. Nine topsoil samples were selected for isotopic analysis of $^{206}Pb/^{207}Pb$ and $^{208}Pb/^{206}Pb$ ratios based on lithological variability and spatial distribution criteria to ensure representative coverage of the study area. These isotopic ratios were measured at the laboratory of Institut de Physique du Globe de Paris (IPGP), Université Paris Cité. Duplicate measurements showed that the ratios of $^{206}Pb/^{207}Pb$ and $^{208}Pb/^{206}Pb$ were highly reproducible, with an analytical precision between 0.1% and 0.0.12%. The mineralogical characterization of the topsoils was determined semi-quantitatively using X-ray powder diffraction (XRD) with a Philips PW14 1373 equipped with Cu-Kα radiation at the Department of Earth and Marine Sciences (DiSTeM), University of Palermo. Topsoil pH was measured potentiometrically on suspensions prepared by adding 25 ml of 1 M potassium chloride to 10 g of dry topsoil. The mixture was stirred for at least two hours and then allowed to sit for 30 minutes. For semi-quantitative assessment of total organic carbon (TOC), the dried sample (at 105 °C overnight) was weighed, and the loss on ignition (LOI) was determined by heating the sample to 450 °C in a muffle furnace for 6 hours. The LOI percentage, obtained by reweighing the samples, indicates the organic matter content, with a conversion factor of 1.724 used to estimate total organic carbon (Nelson and Sommers, 1996).

2.2.3. Pine Needle samples

Among Mediterranean conifers, *Pinus pinea* L. was selected as the model species for this investigation. The choice of this conifer is based on its wide distribution across different environments, its ease of identification, and its suitability for studying the presence of metals in atmospheric aerosol (Alaimo et al., 2000; Bertolotti and Gialanella, 2014; Zsigmond et al., 2021).
Conifers are commonly considered, according to the literature, to be among the most characteristic spontaneous species of the montane belt in Italy, where they often form extensive forests. In urban

green areas, by contrast, they are typically found as isolated specimens or planted in orderly rows. They are not native species but were introduced over time. Thanks to their needle-like leaves-thin and leathery-pines can withstand both the cold climates of mountainous areas and the more arid conditions of the Mediterranean. The stone pine is one of the most iconic conifers in the Italian landscape: it can grow up to 30 meters tall, is highly resinous, usually has a twisted trunk, and features a sparse and irregular crown, either conical or umbrella-shaped.

The needles, ranging from 6 to 12 cm in length, are slender, flexible, and light green or yellow-green in colour (Ferrari and Medici, 1996). This species is a thermophilic, xerophilic, and heliophilous, preferring calcareous soils, particularly in coastal areas. The sampled *Pinus pinea* leaves were homogeneous in appearance and clipped using pruning shears. A total of 40 pine needle samples were collected during the autumn-winter season of 2023 in the Valle del Mela district. Sampling locations were selected based on the presence of *Pinus pinea* L. trees, which were randomly distributed in both areas near the petrochemical plant and in urban areas (26 samples), as well as in areas far from pollution sources, serving as control sites (14 samples). The analysis focused on mature leaves, excluding older ones with long-term pollutant deposition. Leaf sampling was carried out randomly throughout the entire tree crown, preferably from branches not shaded by higher ones. It included green or partially chlorotic leaves to obtain a representative sample. The samples were stored in PVC packages and transported to the laboratory. Bark samples were sampled simultaneously, where possible, for a total of 20. The sampling sites are indicated in Fig.2.7.

Figure 2.7 – Distribution of pine needle samples (in green) and bark samples (in brown) across the study area. The industrial plant is marked in red, and the boundary of the Site of National Interest for remediation (SIN) is outlined in yellow.

They were placed in an oven at 40°C for one week to dry. Afterward, they were cut into 5 mm fragments with a surgical scalpel. The chemical analyses were performed at Activation Laboratories Ltd. (Ontario, Canada). The samples were digested in aqua regia and analyzed by ICP-OES and ICP-MS for Ca, K, Mg, , Na, Al, As, B, Ba, Cd, Co, Cr, Cu, Fe, Mn, Mo, Ni, Pb, Sb, Se, V, Zn, Y, La, Ce, Pr, Nd, Sm, Eu, Gd, Tb, Dy, Ho, Er, Tm, Yb, Lu. Recovery rates for the certified elements ranged from 96% to 106% when using the standard reference materials CLV-1 (spruce twigs) and CLV-2 (spruce needles). Analytical precision, assessed through duplicate analyses performed on every tenth sample, ranged between 10% and 16% for all analyzed elements. A total of 24 pine needle samples, selected based on spatial distribution criteria, were analyzed for their lead isotopic composition ($^{206}Pb/^{207}Pb$ and $^{208}Pb/^{206}Pb$ ratios). The samples were first subjected to acid digestion using a mixture of 5mL of HNO_3. The mineralization process was performed using a Mars X-Press CEM microwave digestion system. The digested samples were sent to the Institut de Physique du Globe de Paris (IPGP), Université Paris Cité, for isotopic analysis. The analytical precision of the $^{206}Pb/^{207}Pb$ and $^{208}Pb/^{206}Pb$ isotopic ratio measurements ranged from 0.1% to 0.2%.

2.3. Statistical perspective

Data were analyzed statistically by the software XLSTAT (Lumivero, 2024), R, Rstudio (R Core Team, 2023), and CoDaPack (Comas-Cufí and Thió-Henestrosa, 2011). All the tests were considered significant at $p < 0.05$. The Shapiro–Wilk test was used to verify the normality of data distributions.

2.3.1. Compositional Data analysis (CoDa) and Compositional Pollution Index (CPI)

Compositional data analysis (CoDA) is a statistical framework specifically developed to handle data expressed in relative terms and constrained by a constant sum. Aitchison (Aitchinson, 1986; Aitchison, 1983, 1982) laid the theoretical foundations of CoDA by defining compositional data as vectors $x=(x_1,\ldots,x\_D)$ with $x\_i \geq 0$ and $\sum x\_i=1$. These vectors consist of strictly positive values that represent the relative contribution of each component to the whole. In the environmental sciences, CoDA is particularly relevant because the relative concentrations of chemical elements often carry more meaningful information than their absolute values. Traditional statistical methods, which disregard the constrained and interdependent nature of compositional data, can lead to misleading interpretations. CoDa addresses this issue by applying log-ratio trasformations (centered log-ratio (CLR), additive log-ratio (ALR) (Aitchison, 1983, 1982) and isometric log-ratio (ILR) (Egozcue et al., 2003), which allow statistical analysis within the appropriate mathematical space while respecting the geometry simplex.

This study adopts a CoDa approach because the measured concentrations in environmental samples are compositional data, as they represent parts of a whole and are subject to a constant sum constraint

(e.g. mg kg^{-1}) (Buccianti and Pawlowsky-Glahn, 2005; Filzmoser et al., 2018; Filzmoser and Hron, 2011; Pawlowsky-Glahn et al., 2019; Pawlowsky-Glahn et al., 2015; Pawlowsky-Glahn and Buccianti, 2011; Pawlowsky-Glahn and Egozcue, 2020; Van Den Boogaart and Tolosana-Delgado, 2013). Given this compositional structure, the functions used in analysis must satisfy two fundamental principles (Boente et al., 2022):

Scala invariance: the results of analysis must remain unchanged if the composition is multiplied by a positive constant. This mean that absolute magnitude of components is irrelevant, and any composition can be expressed in proportions summing to one, without loss or distortion of information.

Sub-compositional coherence: any subset of components (a sub-composition) should yield consistent results with those obtained from the full composition. The coherence of relationships among parts must be preserved, even when focusing on a reduced number of variables.

By adhering to these principles, CoDA ensures that the analysis reflects the true structure of the data and provides reliable insights, especially in contexts like environmental geochemistry where interpreting proportional relationships is crucial. CoDA analysis involved two main phases: preprocessing and statistical analysis: (i) Preprocessing includes the treatment of values below the detection and the imputation of missing data, using methods that are coherent with the compositional structure of the dataset. Once cleaned, the data are transformed using log-ratio transformations, such as the additive log-ratio (arl), centered log-ratio (clr), or isometric log-ratio (ilr). These transformations project the data from the constrained simplex space to real Euclidean space, where standard statistical methods can be appropriately applied; (iii) In the analysis phase, conventional multivariate techniques such as Principal Component Analysis(PCA), cluster analysis and regression models, can be applied the transformed data while preserving the compositional integrity. The particularly informative tool is the CoDa-biplot, a graphical representation that simultaneously displays the observations and the clr-transformed components (Aitchison, 1983; Aitchison and Greenacre, 2002). This biplot is constructed via Singular Value Decomposition (SVD) of the centred clr transformation dataset, effectively performing a PCA on clr(X) after centering, often known as CoDa-PCA. Unlike traditional PCA biplots based on raw data, the interpretation of CoDa-biplot emphasizes the relationship between the rays representing the CLR variables, capturing the relative structure among parts more faithfully.

A key concept in CoDa is the use of *balance*, a logarithmic transformation that allows to compare two groups of components in a robust and interpretable way. A balance is defined through the following relationship (Boente et al., 2022):

$$Balance_{\frac{G}{H}} = \sqrt{\frac{nG \,.\, nH}{nG + nH}} . ln\left(\frac{gm(xG)}{gm(xH)}\right)$$

where n is the number of components in groups G and H respectively, gm is the geometric mean of the components in each group. The square root term is a normalization factor that ensures orthonormality of the resulting in Euclidean space. Balances are especially useful for constructing compositional indicators of contamination (CI) that are both scientifically interpretable and statistically valid. These indicators (CI) increase as the relative contribution of polluting elements grows, while maintaining compositional coherence. In contrast to simple arithmetic ratio, balance takes into account the geometric and log-relative properties of the data. The construction of these indicators can be done following various approaches, the preferable one is obtained on the basis of expert criteria, taking into account a selection of elements (Boente et al., 2022), some of which are considered polluting while others are not. The advantages of the CoDa approach with balances are that it makes the data statistically tractable and consistent, allowing a direct comparison between groups and ensuring a robust environmental interpretation even in the presence of partially missing or abundant data (e.g. many zeros, detection limits or large variability).

2.3.2. Spatial distribution-geostatistical approach

This study employed advanced geospatial modelling techniques to characterize spatial variability, interpolate unsampled values, and assess spatial clustering of geochemical data. The methodological workflow involved spatial interpolation using sequential Gaussian simulation (SGS), followed by spatial cluster detection through local statistical methods. The analysis began with the exploitation of spatial dependencies in the data using the semivariogram (or variogram), which quantifies how spatial correlation changes with distance (Journel and Huijbregts, 1978). Identifying this spatial structure is essential for informing the interpolation and simulation procedures. Although Ordinary Kriging (OK) is widely acknowledged as the best linear unbiased estimator (Isaaks and Srivastava, 1989). Several limitations have been identified, most notably its tendency to smooth spatial variability, underestimate extreme values, and its inability to quantify inherent uncertainty. These shortcomings render Ordinary Kriging less suitable for applications that demand realistic spatial representations (Bai and Tahmasebi, 2022; Yamamoto, 2005). To address these shortcomings, Sequential Gaussian Simulation (SGS) was selected. SGS is a stochastic geostatistical method that generates multiple realizations of the spatial variable, preserving both histogram and spatial correlation of the input data (Deutsch and Journel, 1998). The SGS process used in this study involved the following steps: *Normal score transformation* - the original geochemical data were transformed into a standard normal distribution using a normal score transformation to satisfy the assumption of normality required by

SGS (Goovaerts, 1997); *Simulation procedure* – simulation was carried out on a 150 × 150 km grid using SpaceStat software (BioMedware). For each grid node, values were simulated sequentially using simple kriging (SK), with a zero mean, conditioned on both observed data and previously simulated values; *Back-trasformation* - Once the simulation was complete, the results were back-trasformed to the original data scale, resulting in realizations than retain the empirical distribution and spatial continuity of the data; *Multiple realizations* - Several simulation runs were perfomed to produce a range of equally probable spatial scenarios, enabling the assessment of spatial uncertainty and variability. Following the interpolation and simulation steps, spatial cluster analysis was conducted to identify potential zones of localized contamination. Spatial clustering refers to the tendency of similar values to occur near each other more often than expected by chance. Cluster detection methods were selected based on the classification proposed by Besag and Newell (1991), which distinguishes between "general" and "focused" approaches. "General" methods do not assume prior knowledge about the location of clusters and are further divided into "global" and "local". While global tests evaluate overall clustering across the study area, local tests identify clusters confined to smaller geographic regions. In this study local general methods were employed, which are particularly suitable for detecting localized contamination and assessing whether cases in proximity to a specific case are more spatially clustered than would be expected by chance. Specifically, the Local G statistic was used to measure the degree of spatial association between an observation and its neighbors within a defined distance (Getis and Ord, 1992; Ord and Getis, 1995). The Local G statistics allows for the identification of statistically significant clusters of high or low values, even in the absence of global spatial autocorrelation. The combination of SGS for spatial prediction and Local G for cluster detection provided a robust methodological framework for producing realistic geochemical maps and identifying spatial patterns of environmental concern.

2.3.3. Geochemical baseline

In environmental geochemistry, the geochemical background value, also referred to as the natural background, denotes the concentration of an element that arises solely from natural, geogenic processes in each environment. It serves as a reference point for assessing deviations caused by external influences. In contrast, the geochemical baseline encompasses both natural and anthropogenic inputs, reflecting the total concentration of an element at a specific location and time. As such, the baseline is inherently dynamic and may vary over time due to human activities. In pristine, uncontaminated areas, the background value and baseline coincide. However, in areas subject to anthropogenic impact, the baseline includes a humans-induced component, thereby diverging from the purely natural background only. There are several statistical methods to determine geochemical background/baseline values, robust statistical methods (e.g. Me±MAD, Boxplot,

Iterative 2σ-technique, UTL95-95, cumulative frequency distribution analysis) and spatial statistical methods (Polechońska and Klink, 2023). In this study, data analysis was conducted using a robust statistical approach: the UTL95-95 BCA Bootstrap. This method was selected due to its suitability for estimating upper tolerance limits, particularly in the context of quality control and environmental monitoring, where accurate delineation of threshold values is essential (Lo Medico et al., 2025; Varrica et al., 2024). This method combines the Upper Tolerance Limit (UTL) approach with the BCA bootstrap method. UTL is a statistical value that estimates the upper limit of a certain percentage of a population with a given level of confidence. In particular, the UTL95-95 represents the value below which 95% of the population is expected to fall with a confidence level of 95%. When geochemical data are not normally distributed, non-parametric methods are preferable for the calculation of UTLs and, in this case, the BCA bootstrapping is used. Bootstrapping, which originated in the late 19th century, is a powerful and versatile statistical resampling technique that allows you to estimate the distribution of a statistic when you have a single sample of data. The fundamental principle of bootstrapping involves repeatedly generating many bootstrap samples, typically ranging from 1000 to 10,000 times by randomly the original dataset with replacement, each sample having the same size as the original data. The latter is a crucial point of the method because each data point in the original set has the same probability of being selected for a bootstrap sample and can appear more than once in the same sample. This procedure allows you to capture sampling variability and estimate standard errors and confidence intervals without making assumptions about the shape of the population distribution. Each bootstrap sample represents a possible realization of a sample that could have been drawn from the underlying population. The Bias-Corrected and Accelerated (BCA) method is an advanced variant of the bootstrap method that corrects for both bias and skewness in the simulated sampling distribution, thus yielding more accurate results (Efron and Tibshirani, 1994; Manly, 1997). This technique is particularly useful for environmental data that often have highly skewed and noisy distributions. While bootstrapping constructs confidence intervals directly from the percentiles of the bootstrap distribution, the BCA method makes corrections to improve accuracy, especially when the distribution of the statistic of interest is not symmetric or when the original estimate might be biased. The BCA method introduces two fundamental parameters: the bias correction factor (z0) and the acceleration parameter (a). The bias correction factor (z0) quantifies the discrepancy between the median of the bootstrap replicates and the observed statistic. The acceleration parameter (a) is related to the skewness of the bootstrap distribution and measures the rate of change of the standard deviation of the estimate as the data varies. Once z0 and a have been estimated, they are used to adjust the edges of the confidence interval. The combination of UTL95-95 with BCA bootstrapping is considered a robust approach to establish regional geochemical

backgrounds, especially when the data do not follow a normal distribution. This method offers several advantages over traditional statistical approaches. It is robust to non-normal data distributions, performs well with small sample sizes, and provides more accurate estimates confidence intervals. Its flexibility and broad applicability make it particularly well-suited for the complexities of environmental data analysis. Notably, software such as ProUCL 5.1 (Singh and Maichle, 2015) incorporates the BCA bootstrap method for calculating upper tolerance limits (UTLs), underscoring its relevance and refinement in environmental monitoring contexts.

2.3.4. Geochemical indices

The *Geo-accumulation Index (I_{geo})* is used to assess the accumulation of chemical elements in sediments or soils over time. The I_{geo} is calculated as follow (Muller, 1969; Suresh et al., 2012):

$$I_{geo} = \log_2 \left[\frac{C_i}{1.5B_i}\right]$$

where C_i is the measured concentration of the i^{th} chemical element examined in the topsoil sample, and B_i is the baseline level of the i^{th} chemical element. In this thesis, it used the baseline calculated. Factor 1.5 was used to correct possible variations in the background values of a particular elements in the environment (Santos-Francés et al., 2017). According to Müller classification (1969), the I_{geo} consists of 7 classes: uncontaminated ($I_{geo} \leq 0$), uncontaminated to moderately contaminated ($0 < I_{geo} \leq 1$), moderately contaminated ($1 < I_{geo} \leq 2$), moderately to heavily contaminated ($2 < I_{geo} \leq 3$), heavily contaminated ($3 < I_{geo} \leq 4$), heavily to extremely contaminated ($4 < I_{geo} \leq 5$) and extremely contaminated ($Ig_{eo} > 5$) (Muller, 1969).

The *Enrichment Factor (EF)* is defined as (Sutherland, 2000; Yongming et al.,2006):

$$EF = \frac{\left(\frac{X}{Ref}\right)_{sample}}{\left(\frac{X}{Ref}\right)_{baseline}}$$

where X represents the element of interest and Ref the reference element respectively in the sample (numerator) and in the calculated regional baseline (denominator). In this thesis, it used aluminum as a reference element based on these considerations: (1) it is a high natural abundance, (2) it is considered a conservative element undergoing minimal disturbance by biological, diagenetic, and redox processes (Rollinson, 2014), and (3) it is easily determined by conventional techniques. The categories based on Enrichment Factor (EF) were (Yongming et al., 2006): $EF < 2$ Deficiency to minimal enrichment; $2 < EF < 5$ Moderate enrichment; $5 < EF < 20$ Significant enrichment; $20 < EF < 40$ Very high enrichment; $EF > 40$ Extremely high enrichment.

The Contamination Factor (CF) is the ratio obtained by dividing the element concentration in the investigated site by the background values (Rutkowski et al., 2020). The CF was calculated using:

$$CF = \frac{c_m}{c_b}$$

where C_m is the concentration of an element measured and C_b is the baseline level of the element calculated. The contamination factor of each metal was classified as follows Rutkowski et al. (2020): CF 0–1 No contamination; CF 1–2 Suspected contamination CF 2–3.5; Slight contamination CF 3.5–8; Moderate contamination; CF 8–27 Severe contamination; CF > 27 Extreme contamination.

The *Contamination Degree (C_d)* suggested by Hakanson (1980) is calculated as the sum of the CF for each sample as:

$$C_d = \sum_{i=1}^{i=n} CF$$

Hakanson (1980) proposed the following classification: $C_d < 6$ low degree of contamination; $6 < C_d < 12$ moderate degree of contamination; $12 < C_d < 24$ considerable degrees of contamination; $C_d > 24$ high degree of contamination, indicating serious anthropogenic pollution (Hakanson, 1980).

The *Pollution Load Index (PLI)* originally proposed by Tomlinson et al. (1980) was also used to evaluate for the entire sampling site and it is calculated by the following formula:

$$PLI = (CF_1 \times CF_2 \times CF_3 \times CF_4 \times ... \times CF_n)^{1/n}$$

where CF is a contamination factor and n is number of studied elements. The PLI was classified as follows: PLI=0 background concentration; $0 > PLI \leq 1$ unpolluted to moderately polluted; $1 > PLI \leq 2$ moderately to highly polluted; $3 > PLI \leq 4$ Highly polluted; $PLI \geq 5$ very highly polluted (Tomlinson et al., 1980).

The *Ecological risk index (ERI)* is used for quantitatively expressing the potential ecological risk of investigated metals and is calculated as shown (Hakanson, 1980; Rutkowski et al., 2020):

$$ERI = T_{ri} \times CF$$

where T_{ri} is the toxic response factor for the metals/metalloids and CF is the contamination factor. The T_{ri} values of metals/metalloids (As=10, Cd=30; Cr=2, Co=5; Cu=5, Fe=1; Mn=1; Ni=5, Pb=5, Sb=5; V = 2, Zn=1) were reported in literature (Akoto and Anning, 2021; Hakanson, 1980; Islam et al., 2015; Mgbenu and Egbueri, 2019; Xu, 2008; Yi et al., 2020). The ERI values can be classified as per the following: $ERI < 40$ Low risk; $40 \leq ERI < 80$ Moderate risk; $80 \leq ERI < 160$ Considerable risk; $160 \leq ERI < 320$ High risk; $ERI \geq 320$ Very high risk (Chen et al., 2024).

3. Results and Discussion

This chapter presents the results of comprehensive geochemical analyses performed on different environmental matrices, water, topsoil, and pine needles, in order to assess spatial clustering of geochemical data across the study area and to differentiate between natural geogenic signatures and anthropogenic contributions.

3.1 Water samples: analytical results and statistical evaluation

Seventy-nine water samples were collected in the Valle del Mela district study area. A univariate statistical summary of the field measurements is presented in Table 3.1. The water temperature ranges from 11.2 to 26.4 °C, with a mean temperature of 17.9 °C. The Total Dissolved Solids (TDS) values range from 65 mg L^{-1} to 2871 mg L^{-1}. However, within this range, only two water samples (PE32 and PE58) show values higher than 1000 mg L^{-1} (1167 and 2871 mg L^{-1}, respectively), while the remaining ones range from 65 mg L^{-1} to 648 mg L^{-1}. All waters show redox potentials (E_H) characteristic of an oxygenated environment, with E_H values ranging from 100 mV to 330.50 mV. All samples have pH values between 6.2 and 8.6, indicating conditions from weakly acidic to basic. The partial pressures of CO_2 in the water range between $10^{-3.40}$ and $10^{-0.84}$ atm. All samples except one (PE78) have pCO_2 values higher than atmospheric levels, indicating the possible contribution of respiration and organic decomposition. The partial pressures of O_2 in the water range between $10^{-51.3}$ and $10^{-35.6}$ atm.

Table 3.1 - Statistical summary of the field measurements. MAD: Median Absolute Deviation, rCV%: robust Coefficient of Variation, Q: Quartile, P: Percentile.

	T (°C)	*pH*	*E_H (mV)*	*EC (µS cm^{-1})*	*TDS (mg L^{-1})*	*LogPCO_2*	*Log PO_2*
AVERAGE	18.0	7.14	215	480	314	-2.03	-42.3
MEDIAN	17.1	7.18	210	505	283	-2.01	-41.8
MINIMUM	11.2	6.21	100	75.7	65.2	-3.40	-51.3
MAXIMUM	26.4	8.64	331	1370	2871	-0.84	-35.6
MAD	2.4	0.32	29.0	212	112	0.36	2.70
rCV%	13.4	4.48	13.45	44.1	35.6	-17.70	-6.39
KURTOSIS	-0.6	0.22	-0.01	0.05	42.1	0.21	-0.45
SKEWNEES	0.4	0.28	-0.01	0.50	5.79	-0.61	-0.18
Q_1	15.6	6.83	189	221	165	-2.29	-44.9
Q_3	21.1	7.41	253	628	370	-1.64	-40.0
P10	13.7	6.43	160	120	93.3	-2.85	-46.4
P90	22.7	7.72	276	851	486	-1.35	-38,0

3.1.1. Major elements

The results of the chemical analyses of major elements are reported in Table 3.2. To assess the normality of the data, the Shapiro-Wilk test was applied. This test is particularly suitable for small to moderate sample sizes due to its high statistical power (Razali and Eah, 2011). The results indicated a significant deviation from normality for all analytes considered. Analysis of the skewness index revealed values > 1 for most elements, indicating a strong positive right-skew in distribution, except for Ca, Si and HCO_3^- which show a weakly asymmetric distribution. Similarly, the kurtosis coefficient suggested that many distributions are leptokurtic, characterized by heavier tails compared to a normal distribution. However, Ca and HCO_3^- exhibited platykurtic distributions, with lighter tails, while Si showed a nearly mesokurtic behavior.

Table 3.2 - Descriptive statistics of major elements concentrations in water samples. MAD: Median Absolute Deviation, rCV%: robust Coefficient of Variation, Q: Quartile, P: Percentile, Data in mg L^{-1}.

		AVERAGE	*MEDIAN*	*MINIMUM*	*MAXIMUM*	*MAD*	*rCV%*	*KURTOSIS*	*SKEWNEES*	*Q_1*	*Q_3*	*P10*	*P90*
Major elements (mg L^{-1})	Na	1.81	2000	46.8	20.3	7.76	17	79	8.9	12.5	27.9	9.37	37.4
	Ca	3.70	149	63.1	62.4	26.4	42	-0.8	0.2	35.7	88.8	7.84	120
	Mg	1.07	90.8	11.5	6.71	3.89	34	14	3.5	4.10	12.85	3.03	18.6
	Si	0.07	17.2	4.2	2.30	2.00	48	0.2	1.0	0.60	7.60	0.38	9.38
	K	0.52	41.5	7.4	6.10	4.11	56	7.6	2.3	1.98	10.0	1.62	15.4
	F	0.21	2.2	0.8	0.68	0.30	38	2.0	1.4	0.50	0.90	0.35	1.40
	Cl	9.40	2100	56.9	24.5	7.60	13	78	8.8	17.4	38.7	13.0	53.2
	Br	0.02	7.4	0.2	0.03	0.03	17	59	7.7	0.03	0.10	0.02	0.15
	NO_3	0.08	7.5	1.5	0.91	0.49	33	4.5	2.1	0.50	1.80	0.28	3.31
	PO_4	0.01	0.3	0.03	0.02	0.01	26	49	6.8	0.02	0.03	0.01	0.03
	SO_4	7.80	711	77.5	67.3	33.7	44	30	4.8	24.9	96.7	16.0	115
	HCO_3	6.00	485	176	155	93.4	53	-0.8	0.5	92.9	276	26.4	360

To identify different water types and understand the process affecting water chemistry, the concentrations of the ion species Ca^{2+}, Mg^{2+}, Na^+, K^+, Cl^-, SO_4^{2-} and HCO_3^- were interpreted by projecting samples point onto several graphical tools: Langelier-Ludwing square diagram (Langelier and Ludwig, 1942) (Fig. 3.1), the Durov diagram (Fig. 3.2), Schoeller diagram (Fig.3.3), the Gibbs diagram: $(Na^+ + Ca^+)$/Na–TDS plot (Fig. 3.4). The Langelier-Ludwig diagram (Fig. 3.1) characterizes the analyzed waters as: I) chloride-sulphate alkaline waters II) bicarbonate earth-alkaline waters and III) chloride-sulphate earth-alkaline waters.

Comparing the *facies*, the group of chloride-sulfate alkaline waters, consisting of 15% of total samples, has low salinity (median TDS = 92.3 mg L^{-1}), except for sample PE58, which shows a TDS value of 4881 mg L^{-1}. This sample differs significantly from the others belonging to the same *facies*, both in the concentrations of cations and anions and in the hydrochemical parameters. These characteristics suggest possible interactions with seawater, consistent with the geographical location of the sampling site in the Milazzo Plain. The order of ion abundance in meq L^{-1} is as follow:

$Na^+ > K^+ > Ca^{2+} > Mg^{2+}$ $Cl^- > HCO_3^- > SO_4^{2-}$

The low degree of mineralisation of these group samples suggests that the contact time with soil and host rocks may have been short. A significant feature of these waters is their weakly acidic character, with pH values in the range of 6.2–7.5. The Cl^- median concentration is 15.5 mg L^{-1}, which is probably derived from atmospheric precipitation, except for sample PE58 that shows a very high Cl^- concentration (2100 mg L^{-1}).

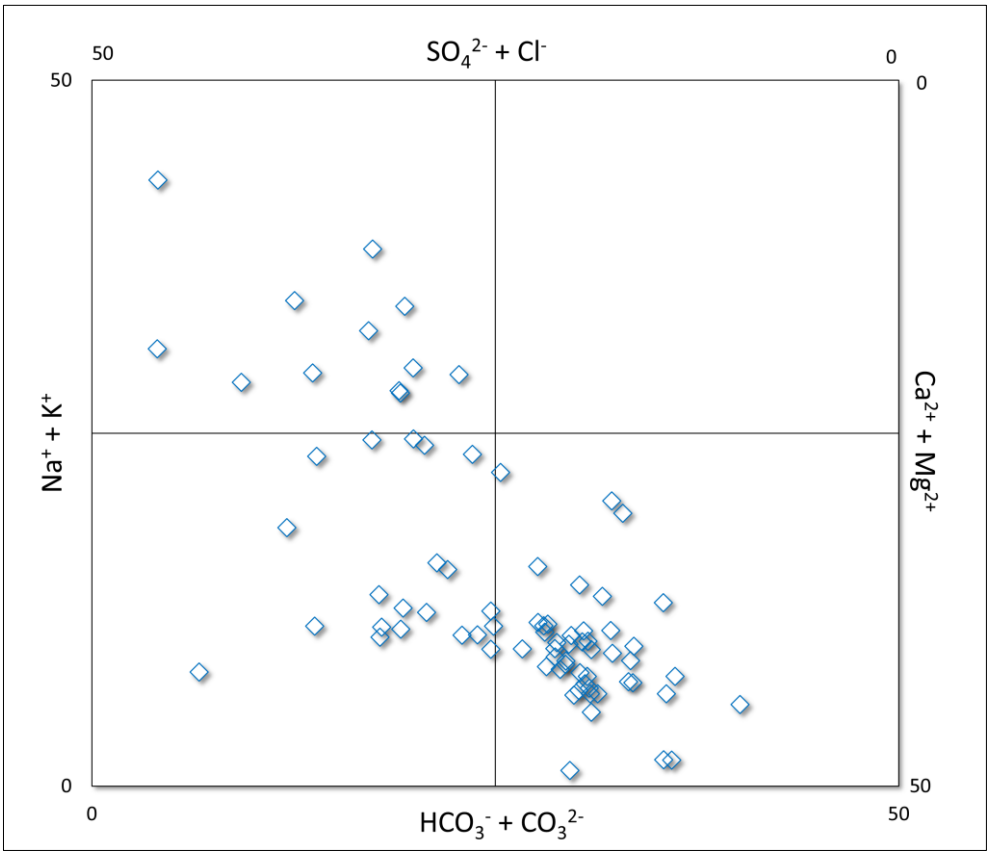

Figure 3.1 - Langelier–Ludwig diagram.

The group of bicarbonate earth-alkaline waters consists of 58% of total samples, has high salinity values (median TDS = 340.3 mg L^{-1}) and an ionic composition with the following order of abundance (meq L^{-1}):

$Ca^{2+} > Mg^{2+} \geq Na^+ > K^+$ $HCO_3^- > SO_4^{2-} > Cl^-$

The TDS levels are significantly higher than those of the chloride-sulfate alkaline waters group, indicating a more effective weathering process. Measured pH values are close to neutral and alkaline, ranging from 6.3 to 8.6.

The group of chloride-sulfate earth-alkaline waters consists of 27% of the total samples. This group is characterized by the following ion abundances (meq L^{-1}):

$Ca^{2+} > Na^{+} > Mg^{2+} > K^{+}$ $SO_4^{2-} \geq HCO_3^{-} > Cl^{-}$.

The pH range is 6.2 - 8.1. The median TDS value is medium-high salinity (median TDS = 298.6 mg L^{-1}). Samples within this *facies* have SO_4^{2-} values ranging from 10 to 266 mg L^{-1}, indicating the presence of multiple processes that have contributed to the chemistry of all water samples. Comparing SO_4^{2-} concentrations detected in the water groups shows an increasing trend from waters with lower TDS to waters with higher TDS. This increase may result from both gypsum dissolution and oxidation of sulfide minerals. In this group, the PE32 sample has TDS value of 1167 mg L^{-1}, differing from the other samples for the concentrations of Ca^{2+} and SO_4^{2-} ions, suggesting an evaporitic rock interaction process. It follows that within this quadrant, waters follow different evolutionary pathways. According to the Durov diagram (Fig. 3.2), most samples are dominated by Ca^{2+}, indicating interaction with carbonate rocks.

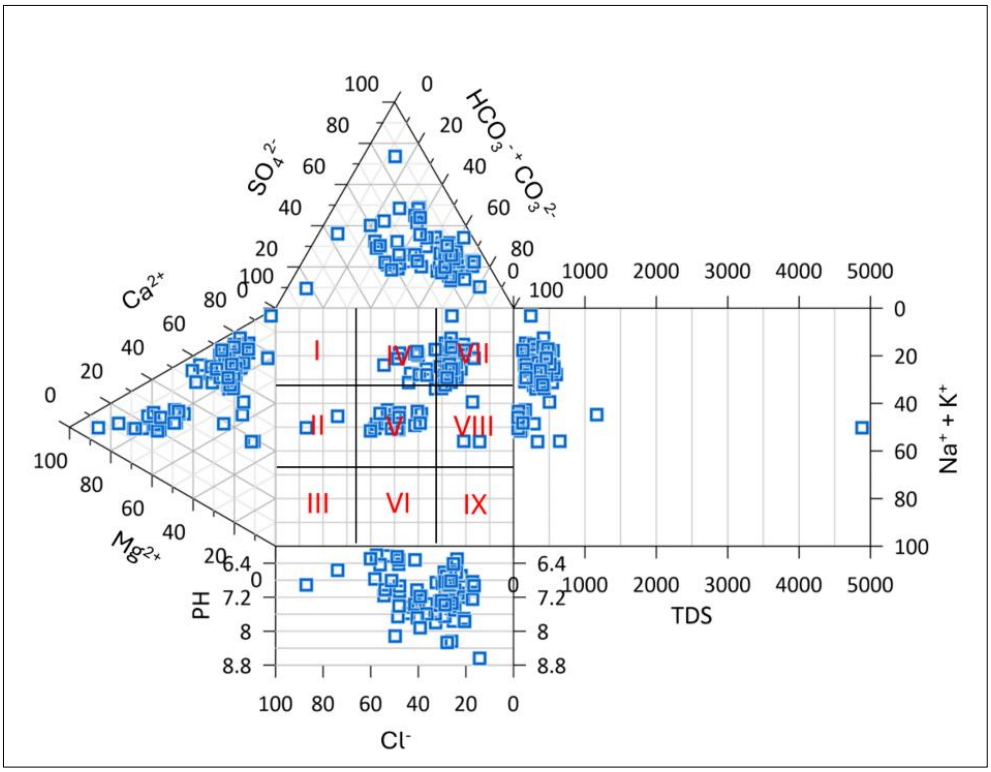

Figure 3.2 - Durov diagram. I: mixing and reverse cation exchange waters of Cl-Ca type; II: mixing and reverse cation exchange reactions; III: mixing with sea waters; IV: calcite and gypsum dissolution; V: mixing reactions from various origin; VI: mixing and cations exchange waters; VII: infiltration waters of HCO_3-Ca type; VIII: cation exchange reactions; IX: cation exchange waters of HCO3-Na type. Data in meq L^{-1}%.

A group of samples is separate from the main cluster and presents variable concentrations of Mg^{2+} and higher concentrations of Na^{+} and K^{+}. Confirming an interaction with carbonate rocks, a high percentage of samples dominated by HCO_3^{-}-CO_3^{2-} is observed, followed by some with an intermediate percentage of Cl^{-}. The concentration of sulfates is variable. In the central diagram, the distribution of points highlights two main hydrochemical *facies*: bicarbonate-calcic (Ca-HCO_3) and cationic ion exchange processes and aluminosilicate alteration. Regarding the side panel of the Durov

plot, the analysis of total dissolved solids (TDS) shows that most samples fall within the low TDS range (TDS < 1000 mg L^{-1}). However, some isolated samples have higher TDS values, suggesting different chemical evolution or possible contamination from marine ingression. The pH generally trend toward neutral or slightly alkaline values (between 7.2 and 8.4). The Schoeller diagram (Fig. 3.3) displays the absolute concentrations of major dissolved ions on a logarithmic scale for each sample. The lines connecting ion values create a distinctive "geochemical signature", which enables rapid comparison of the ionic composition of the waters analyzed.

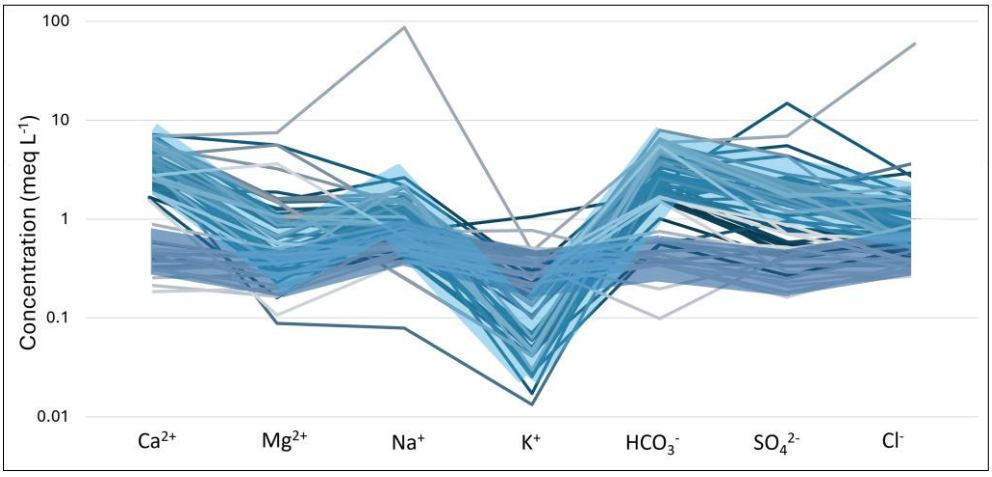

Figure 3.3 – Schoeller diagram. Data in meq L^{-1}.

The simultaneous plotting of multiple samples allows for direct visual comparison: similar patterns suggest a common origin or analogous hydrogeochemical processes, whereas divergent trends indicate differences in water-rock interaction mechanisms or the influence of external inputs. Data analysis reveals two distinct groups of samples, each associated with different hydrogeochemical processes. The first group is characterized by a systematic predominance of Ca^{2+} and HCO_3^-, along with low concentrations of K^+, consistent with a calcium-bicarbonate water type, indicative of interaction with carbonate lithologies. The second group, in contrast, shows overall lower ion concentrations but marked peaks in Na^+ and Cl^-, suggesting possible influence from marine intrusion and/or alteration of aluminosilicate minerals. Two samples (PE58 and PE32) deviate significantly from the main trends. Specifically, sample PE58 shows elevated concentrations of Na^+ and Cl^-, while PE32 exhibits anomalous values for SO_4^{2-} and Ca^{2+}. These patterns, when considered alongside the corresponding TDS values, support the hypothesis of marine intrusion in the case of PE58 and the sulfate mineral dissolution, such as gypsum, in the case of PE32. The molar ratio $Na^+/ (Na^+ + Ca^{2+})$ is commonly used to evaluate the main geochemical processes governing water evolution, particularly mineral dissolution, evaporation, and precipitation. Figure 3.4 shows a clear separation of the samples into two distinct groups. One group is characterized by moderate to high values of the $Na^+/(Na^+ + Ca^{2+})$ ratio and relatively low TDS concentrations, which may reflect ion exchange processes or the

weathering of aluminosilicate minerals. The second group consists of waters with significantly higher TDS values and lower $Na^+/(Na^+ + Ca^{2+})$ ratios. The relative enrichment in Ca^{2+} in this group suggests different water–rock interaction mechanisms, likely associated with the dissolution of carbonate lithologies. Therefore, this dichotomy indicates the coexistence of two distinct hydrogeological circuits within the study area. Moreover, the position of local precipitation samples (Brugnone et al., 2023) suggests a geochemical evolution gradient, ranging from younger to more mature waters. Chemical processes such as carbonate dissolution and aluminosilicate mineral hydrolysis characterize the area of investigation (Dongarrà et al., 2009).

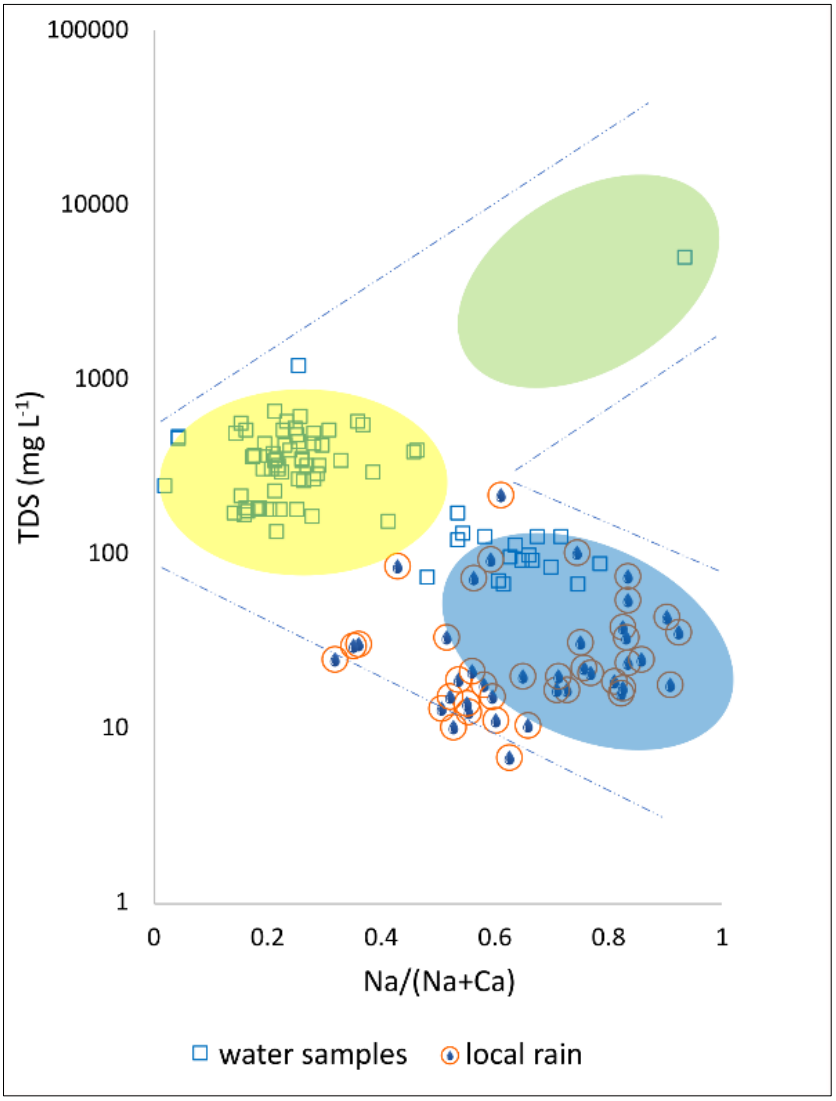

Figure 3.4 –Gibbs diagram: Na/(Na + Ca) vs. TDS plot. Blue area: precipitation domain (Brugnone et al., 2023), yellow area: water-rock interaction domain; green area: evaporation domain.

The dissolution of carbonate minerals in the study area is certainly one of the most important chemical processes. Figure 3.5 reports the activity of Ca^{2+} as a function of pH, illustrating the saturation state of the analyzed waters with respect to calcite and dolomite minerals. The waters appear to have evolved in open-system conditions at CO_2 pressures ranging from 10^{-2} to 10^{-3} bars. With respect to

calcite, a group of water samples is mainly undersaturated, with Saturation Index (SI) values below 2. These samples correspond to those classified as chloride-sulfate alkaline waters. The other samples are close to equilibrium saturation or supersaturated. However, it is possible to observe different trends. Some samples fall within the range of ±0.5 for calcite (-0.5<SI<0.5), indicating that they are close to equilibrium. Others, characterized by a more basic pH (7.7<pH<8.7), are supersaturated with respect to dolomite. Most samples occupy the left sector of the graph, characterized by slightly more acidic pH values.

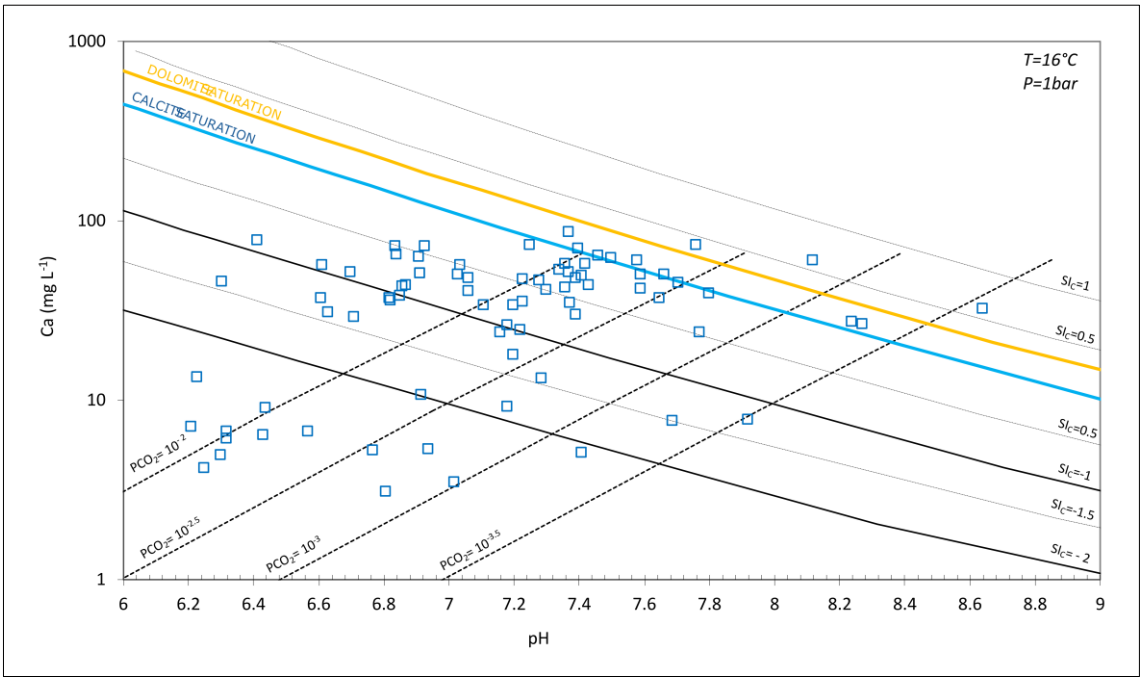

Figure 3.5 - Graph of Ca concentration vs pH. The black dotted lines represent the dissolution of calcite under open-system conditions at various values. The solid blue and yellow lines represent the theoretical solubility curves for calcite and dolomite at 16 °C. The solid black lines indicate different saturation states with respect to calcite.

All these data are consistent with a reaction scheme where meteoric waters flowing through the soil zone gain high CO_2 pressure, even well above 10^{-2} bar, and are then driven toward saturation by reacting with carbonate minerals in the soil and host rocks following these reactions:

$CaCO_2 + H_2O + CO_2(g) = Ca^{2+} + 2HCO_3^-$

$CaMg(CO_3)_2 + H_2O + CO_2(g) = Ca^{2+} + Mg^{2+} + 2HCO_3^-$

The continuous supply of CO_2, linked to rainwater infiltration through the soil, the pH value, and potential kinetic constraints, makes the weathering process appear faster than calcite precipitation. The water, therefore, accumulates Ca^{2+} (and HCO_3^-) while remaining undersaturated with respect to mineral formation. Furthermore, in this study, the main saturation indices of mineral phases were calculated using the WATEQ4F software (Plummer et al., 1976). As shown in Table 3.3, the results indicate that all water samples are undersaturated with respect to anhydrite, gypsum, albite, and anorthite, while exhibiting saturation or oversaturation with respect to clay minerals. This suggests

that the incongruent weathering of feldspar is a kinetically slow geochemical process (Berg and Banwart, 2000), during which silica and alkali metals are released into solution, contributing to the formation of secondary aluminosilicate minerals such as clays. The concentration range of dissolved silica in the waters studied is between 0.067 and 17.20 mg L^{-1}, with a median value of 2.3 mg L^{-1}.

Table 3.3 - Average Saturation Index (SI) values for mineralogical phases.

	AVERAGE	*MEDIAN*
Albite	-4.33	-3.59
Anhydrite	-2.30	-2.05
Anorthite	-5.77	-5.58
Chlorite	-12.4	-12.0
Gypsum	-2.06	-1.81
Illite	-1.74	-1.11
Kaolinite	1.97	2.10
Montmoril Ca	-0.62	-0.09
Quartz	-0.11	0.15
Silica	-1.43	-1.16

Although all samples are undersaturated with respect to amorphous silica (-1.43<SI<-1.16), most exhibit equilibrium relative to quartz (-0.11<SI<-0.15) (Tab.3.3). Given the low dissolution rate of quartz under environmental conditions (Lasaga, 1984), and despite its abundance in the local lithology, it is unlikely to be the primary contributor to acqueous silica. Instead, the data suggest that the principal sources of silica are the weathering of aluminosilicate minerals or the dissolution of amorphous silica (Feth et al., 1964). All the analyzed waters are close to equilibrium or supersaturated with respect to kaolinite (Tab.3.3). To further evaluate the geochemical controls on acqueous chemistry, the activity of major cations were plotted on stability diagrams for the $Na_2O–SiO_2–Al_2O_3–H_2O$, $K_2O–SiO_2–Al_2O_3–H_2O$, $CaO–SiO_2–Al_2O_3–H_2O$, and $MgO–SiO_2–Al_2O_3–H_2O$ systems. In these diagrams (Fig. 3.7a–f), the majority of samples plot within the kaolinite stability field, strongly suggesting that equilibrium with kaolinite is a dominant geochemical process controlling solute composition and mineral-water interactions in the system. This arrangement is consistent with the reaction pathways expected for solutions interacting with carbonate and silicate rocks (Garrels, 1967; Marini, 2007). The attack of H_2CO_3 produced by the reaction between CO_2 and water or of H_2SO_4 produced by the oxidation of sulphides on primary aluminosilicates releases Al and Si, with consequent formation of Gibbsite, which is altered into kaolinite by reaction with silica or feldspar, according to the reactions:

$NaAlSi_3O_8 + H^+ + 7H_2O = 3H_4SiO_4 + Al(OH)_3 + Na^+$

$CaAl_2SiO_8 + 2H^+ + 6H_2O = Ca^{2+} + 2H_4SiO_4 + 2Al(OH)_3$

$KAlSi_3O_8 + H^+ + 7H_2O = 3H_4SiO_4 + Al(OH)_3 + K^+$

$2Al(OH)_3 + 2H_4SiO_4 = Al_2Si_2O_5(OH)_4 + 5H_2O$

$4Al(OH)_3 + NaAlSi_3O_8 + H_2O = 3Al_2Si_2O_5(OH)_4 + 2Na^+ + 2OH^-$

The diagrams in Figure 3.6 show that the water samples invade the stability fields of Na-montmorillonite, Ca-montmorillonite, and Mg-montmorillonite. This indicates that the water-rock interaction time was sufficient for kaolinite to react with silica and cations (Na, Ca, and K) to form smectites (Na, Mg, or Ca montmorillonite) or illite.

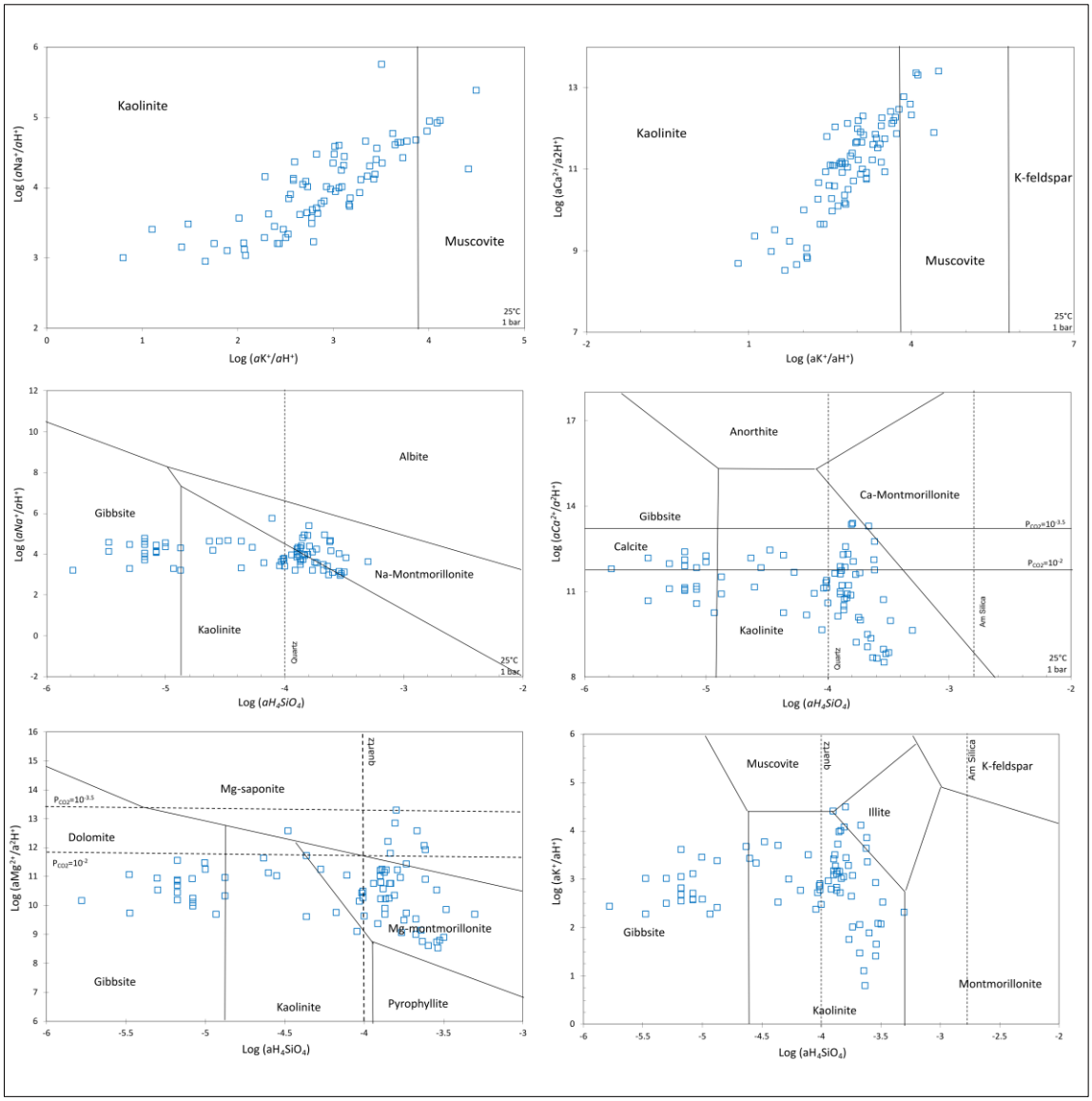

Figure 3.6 - Selected activity diagrams in $CaO–SiO_2–Al_2O_3–H_2O$, $MgO–SiO_2–Al_2O_3–H_2O$, $Na_2O–SiO_2–Al_2O_3–H_2O$ and $K_2O–SiO_2–Al_2O_3–H_2O$ systems at 25 °C and 1 bar. Activity plots of (a) log (aNa^+/aH^+) vs. log (aK^+/aH^+), (b) log (aCa^{2+}/a^2H^+) vs. log (aK^+/aH^+); (c) log (aNa^+/aH^+) vs. log (aH_4SiO_4); (d) log (aCa^{2+}/a^2H^+) vs. log (aH_4SiO_4), (e) log (aMg^{2+}/a^2H^+) vs. log (aH_4SiO_4); (f) log (aK^+/aH^+) vs. log (aH_4SiO_4). Saturation lines for calcite and dolomite, at CO_2 partial pressures of $10^{-3.5}$ and $10^{-2.0}$ atm, are also shown in (d) and (e), respectively.

3.1.2 Trace elements and Rare Earth Elements (REEs)

The results of chemical analyses for trace elements in water samples are presented in Table 3.4. The geochemistry of trace elements in water typically reflects the interactions between water and the surrounding lithology. Highly variable elemental concentrations for some elements may indicate the presence of external inputs that contribute to the total concentration (Table 3.4).

The average distribution of trace elements is classified as follows:

>30 μg L^{-1} Zn

30-10 μg L^{-1} Ba, Fe

10-1 μg L^{-1} Al, Cu, Mn, Mo, Ni

<1 μg L^{-1} As, Cd, Co, Cr, Pb, Sb, Se, V

Table 3.4 - Descriptive statistics of major elements concentrations in water samples. MAD: Median Absolute Deviation, rCV%: robust Coefficient of Variation, Q: Quartile, P: Percentile. Data in μg L^{-1}.

		AVERAGE	*MEDIAN*	*MINIMUM*	*MAXIMUM*	*MAD*	*rCV%*	*KURTOSIS*	*SKEWNEES*	*Q_1*	*Q_3*	*P10*	*P90*
Trace elements (μg L^{-1})	Al	9.61	5.000	0.145	58.00	2.613	27	5.8	2.4	3.000	10.00	2.002	24.51
	As	0.62	0.290	0.015	6.213	0.220	35	18	3.6	0.125	0.695	0.060	1.464
	Ba	32.7	20.00	1.128	164.0	12.78	39	3.7	1.8	11.90	51.25	5.623	70.76
	Cd	0.03	0.012	0.002	0.270	0.008	29	18	3.9	0.008	0.031	0.003	0.060
	Co	0.04	0.021	0.005	0.345	0.011	28	18	3.9	0.014	0.042	0.008	0.087
	Cr	0.26	0.170	0.046	1.693	0.049	18	14	3.2	0.167	0.332	0.096	0.600
	Cu	4.31	1.800	0.200	75.00	1.099	26	53	6.8	0.950	5.500	0.563	9.420
	Fe	14.74	10.00	0.769	90.00	7.19	49	8.7	2.7	3.578	20.00	2.284	30.00
	Mn	1.59	0.500	0.011	40.50	0.300	19	61	7.5	0.207	1.275	0.171	2.775
	Mo	1.14	0.653	0.051	10.20	0.503	44	22	3.8	0.200	1.650	0.105	2.320
	Ni	1.92	0.900	0.075	19.40	0.593	31	19	4.1	0.550	1.813	0.249	3.466
	Pb	0.31	0.240	0.002	1.780	0.160	51	7.5	2.1	0.095	0.465	0.040	0.632
	Sb	0.13	0.030	0.0001	4.879	0.020	16	76	8.6	0.020	0.090	0.010	0.214
	Se	0.72	0.523	0.170	6.300	0.223	31	29	4.8	0.300	0.800	0.170	1.120
	V	0.83	0.700	0.033	5.200	0.300	36	12	3.1	0.347	0.911	0.138	1.351
	Zn	69.9	12.30	0.800	2010	9.12	13	48	6.6	5.127	27.60	1.917	90.70

The distribution, mobility, and persistence of trace elements in aqueous systems are governed by physico-chemical parameters, with pH and redox potential (E_H) being among the most influential. These parameters play a crucial role in controlling the geochemical speciation of trace elements, as they govern both their solubility and their ability to form complexes with inorganic and organic ligands. Trace elements that stay dissolved can bind to mineral surfaces or precipitate as solid phases. The main aqueous chemical forms of trace elements (Tab. 3.5) have been predicted by the geochemical modeling program PHREEQC, which is implemented with the MINTEQ.V4.dat database (Allison et al., 1991), considering the most common inorganic ligands in water (such as OH, Cl, F, SO_4, HCO_3, and CO_3). Among all water samples analyzed, the predominant free ions were Cd^{2+}, Fe^{2+}, Mn^{2+} and Zn^{2+}. Dissolved Cd mainly exists as a free hydrated ion (66.81%), consistent with findings reported in previous studies (Dongarrà et al., 2009; Korfali and Davies, 2004; Tipping et al., 1998; Turner et al., 1991). However, Cd also forms complexes with hard bases, such as $CdSO_4$ (6.43%) and $Cd(HCO_3)^+$ (4.90%), as well as with weak bases, such as $CdBr^+$ (17.25%). Thermodynamic calculations predict that Mn^{2+} dominates among free ions, accounting for 73.8%, with $Mn(HCO_3)^+$ at 15.24%, and a smaller amount of $MnCO_3$ at 7.51% and $MnSO_4$ at 3.22%. Iron mainly exists as Fe^{2+} ion (58.52%), followed by $FeHCO_3^+$ at 13.56% and $FeHPO_4$ at 10.34%, with

lesser quantities of $Fe(OH)_3$, $Fe(OH)_2^+$, $FeSO_4$, $FeCO_3$ and $FeH_2PO_4^+$, $FeCO_3$ (under 10%). Dissolved Zn is primarily represented as Zn^{2+}(56.87%), with $Zn(HCO_3)^+$ at 21.57%, $Zn(CO_3)$ at 13.70%, and a smaller proportion of $ZnSO_4$ at 6.16%. Aluminum predominantly exists as $Al(OH)_4^-$ (89.79%). Water speciation data indicate that 51.56% of the total copper is present as the ion pair $CuCO_3$, followed by 29.85% as $Cu(OH)_2$, with the remaining percentages comprising $Cu(HCO_3)^+$, Cu^{2+}, and $CuOH^+$. Chromium mainly appears as $Cr(OH)_2^+$ (80.38%) and $Cr(OH)^{2+}$ (16.96%), contrasting with elements like Zn and Cu, which have a moderate association with carbonate species. Carbonate complexes, such as $NiCO_3$ (83.20%) are predominant for nickel, accounting for a major part of dissolved nickel, with 12.54% existing as free Ni ions. Lead primarily exists as $PbCO_3$ (82.74%) with only 7.08% as Pb^{2+}. Arsenic and antimony are present in their oxidized forms, As^{5+} and Sb^{5+}. Chemical speciation calculations forecast the arsenate hydrolysis products, $HAsO_4^{2-}$ (48.06%) and $H_2AsO_4^-$ (51.94%), predominate as arsenic species, with As^{5+} strongly adsorbed onto Fe oxyhydroxides (Sadiq, 1997). current redox conditions, PHREEQC predicts the presence of SbO_3^- (99.88%) and the oxyanion $Sb(OH)_6$ (0.12%). Similar to arsenic, Sb^{5+} can be strongly adsorbed onto charged Fe oxyhydroxide surfaces (Belzile et al., 2001; Casiot et al., 2007).

Tab. 3.5 - Trace elements: principal aqueous chemical forms predicted by PHREEQC (Parkhurst and Appelo, 1999) and MINTEQ.V4.dat database (Allison et al., 1991).

PRINCIPAL AQUEOUS CHEMICAL FORMS	
Al →	**$Al(OH)_4^-$** (89.79%), $Al(OH)_3^0$ (3.73%), $Al(OH)_2^+$ (3.17%), $AlF2^+$(2.28%), others (<1%)
As →	**$H_2AsO_4^-$ (51.94%), $HAsO_4^{2-}$ (48.06%),** others (<1%)
Cd →	**Cd^{2+} (66.81%), $CdBr^+$ (17.25%),** $CdSO_{4aq}^0$ (6.43%), $Cd(HCO_3)^+$ (4.90%), $CdCl^+$ (4.41%), others (<1%)
Cr →	**$Cr(OH)_2^+$ (80.38%), $Cr(OH)^{2+}$ (16.96%),** $Cr(OH)_3^0$ (2.54%), others (<1%)
Cu →	**$CuCO_{3aq}^0$(51.56%), $Cu(OH)_2^0$ (29.85%),** $Cu(HCO_3)^+$ (8.71%), Cu^{2+} (7.50%), $CuOH^+$ (1.04%), others (<1%)
Fe →	**Fe^{2+} (58.52%), $Fe(HCO_3)^+$** (13.56%), **$FeHPO_{4aq}^0$ (10.34%),** $Fe(OH)_3^0$ (5.62%), $Fe(OH)_2^+$ (4.34%), $FeSO_4^0$ (3.18%), $FeH_2PO_4^+$ (2.37%), $FeCO_{3aq}^0$ (1.80%), others (<1%)
Mn →	**Mn^{2+}** (73.8%), **$Mn(HCO_3)^+$** (15.24%), $MnCO_{3aq}^0$ (7.51%), $MnSO_{4aq}0$ (3.22%), others (<1%)
Ni →	**$NiCO_3^0$ (83.20%), Ni^{2+} (12.54%),** $Ni(HCO_3)^+$ (3.27%), others (<1%)
Pb →	**$PbCO_{3\,aq}$** (82.74%), Pb^{2+} (7.08%), $Pb(HCO_3)^+$ (6.67%), $Pb(OH)^+$ (1.36%), others (<1%)
Sb →	**SbO_3^-** (99.88%), **others** (<1%)
Zn →	**Zn^{2+}** (56.87%), **$Zn(HCO_3)^+$ (21.57%), $Zn(CO_3)^0$** (13.70%), $ZnSO_{4aq}^0$ (6.16%), others (<1%)

Rare earth elements are valuable tools for assessing water-rock interaction processes that influence the chemistry of natural waters (Bau, 1999; Cidu et al., 2013; Gammons et al., 2005; Göb et al., 2013; Johannesson et al., 2000, 1997, 1996; Liu et al., 2016; Möller et al., 2016, 2003; Siebert et al., 2012; Smedley, 1991; Tang and Johannesson, 2010; Willis and Johannesson, 2011; Yan et al., 2013). These elements occur in minerals at varying concentrations (Chakhmouradian and Wall, 2012; Jordens et al., 2013; Ramos et al., 2016), and their availability in the environment under natural conditions depends on the source material as well as geochemical and biological processes (Cidu et al., 2013; Zhang et al., 2001). The determination of these elements in natural waters is also important

considering the rapid environmental changes driven by human activity (Bau et al., 2006; Bau and Dulski, 1996; Kulaksız and Bau, 2013, 2011; Migaszewski and Gałuszka, 2016; Möller, 2002; Otero et al., 2005; Wysocka et al., 2023; Zalasiewicz et al., 2021). In recent decades, their use has increased in the industrial production of high-tech devices, fertilizers, and animal feed additives (Laveuf and Cornu, 2009; Schwabe et al., 2012).

The average and median concentrations of rare earth elements (REEs) in water samples are presented in Table 3.6. The median concentrations of individual REEs and Y decrease in the following order: Y>La>Ce>Nd>Pr>Gd>Dy>Yb>Sm>Er> Eu> Ho> Tb>Tm>Lu.

Y, La, Ce, and Nd are the most abundant REEs, with median concentrations of 31 ng L^{-1}, 11 ng L^{-1}, 8 ng L^{-1}, and 7 ng L^{-1}, respectively. The remaining REEs show significantly lower median contents, ranging from 2 ng L^{-1} for Pr to 0.33 ng L^{-1} for Lu.

Table 3.6 - Average and median REE concentrations in water samples. Data in ng L^{-1}.

	REE elements (ngL^{-1})														
	Y	*La*	*Ce*	*Pr*	*Nd*	*Sm*	*Eu*	*Gd*	*Tb*	*Dy*	*Ho*	*Er*	*Tm*	*Yb*	*Lu*
AVERAGE	114.32	93.44	92.96	89.01	91.00	84.40	83.31	84.70	83.10	84.41	83.13	83.95	83.02	84.04	83.15
MEDIAN	31.00	11.00	8.00	2.00	7.00	1.00	0.33	2.00	0.29	2.00	0.30	1.00	0.26	2.00	0.23

The data were normalized for the using the values proposed by Anders and Ebihara (1982). REEs have been divided into three groups (Chen et al., 2015; Dubinin, 2004; Migaszewski and Gałuszka, 2019): light (LREEs), medium (MREEs), and heavy (HREEs). (Tab. 3.7).

Table 3.7 - Average and median values of total, light (LREE), medium (MREE), heavy (HREE) Rare Earth Element (REE) concentrations and the LREE/HREE ratio. Data in ng L^{-1}.

	∑REE	*∑LREE*	*∑MREE*	*∑HREE*	*∑LREE/∑HREE*
AVERAGE	0.26	0.13	0.07	0.06	1.93
MEDIAN	0.15	0.06	0.03	0.04	1.30

In the analyzed water samples, LREEs are more abundant than MREEs and HREEs. This distribution pattern also matches the typical ratio between these groups in the Earth's crust (Migaszewski and Gałuszka, 2015), indicating that water-rock interaction processes mainly influence REE signatures in aquatic systems. The REE profiles (Fig. 3.7) appear to be driven by the composition of the parent material. The pattern of the water samples appears to follow the geochemical signature of carbonate rocks, showing an enrichment of light rare earth elements (LREEs) compared to heavy rare earth elements (HREEs), which is typical of carbonate rocks. A significant negative anomaly in Ce is also observed.

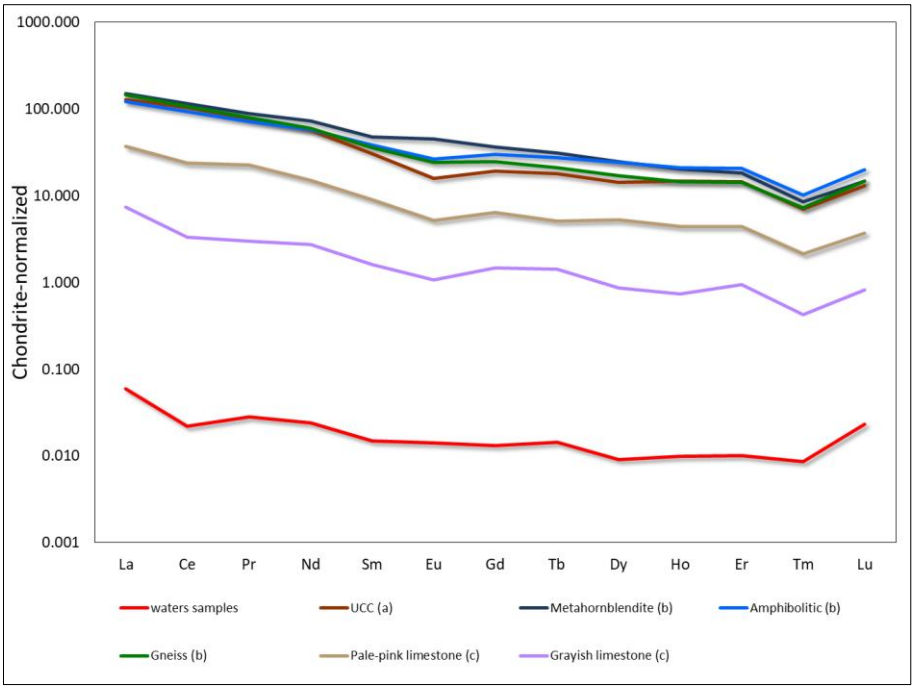

Figure 3.7 - Chondrite-normalized rare-earth element spider diagram for median of water samples and reference about: (a) Upper Continental Crust (UCC) (Taylor and McLennan,1985; McLennan, 2001); (b) Metamorphic substrate (Duplay et al., 2014; Messina, unpublished), (c) sedimentary substrate (Messina et al.,2004).

Deviations from expected REE patterns can provide insights into specific geochemical behaviors or the influence of human activities (Smedley, 1991; Willis and Johannesson, 2011). Among these, Ce and Eu anomalies are significant because of their high redox sensitivity, which distinguishes them from other REEs (Brookins, 1983). The anomalies were calculated using the following formulas (Cao et al., 2022; Chang et al., 2019; Ion and Cosac, 2023; Lawrence et al., 2006; Noack et al., 2014; Rétif et al., 2023; Wilkin et al., 2021):

$$Ce/Ce^* = \frac{Ce^*}{\left(\frac{\rho_r\ {}^{*2}}{Nd^*}\right)}$$

$$Eu\ /\ Eu^* = \frac{2 \times Eu^*}{(Sm^* + Gd^*)}$$

Asterisks (*) are used to indicate normalized concentrations. Both positive and negative Ce anomalies were observed in the analyzed waters, serving as indicators of prevailing redox conditions. These patterns are consistent with Ce anomalies previously reported in soils from the same study area (Saiano et al., 2024). Negative Ce anomalies are generally associated with oxidizing environments, such as surface waters, where Ce^{3+} is oxidized to Ce^{4+}. This oxidation promotes the precipitation of cerium as $CeO_{2(s)}$ and increases its adsorption onto Fe/Mn oxyhydroxide particles (Bau, 1999; Bozau et al., 2013; Dia et al., 2000). The negative anomaly may also result from the dissolution of host rocks, such as limestones and dolomites (Willis and Johannesson, 2011; Yan et al., 2013). A similar redox-dependent behavior is observed for Eu, which also exhibits both positive and negative

anomalies. Negative Eu anomalies generally indicate reducing conditions, where Eu^{3+} is reduced to Eu^{2+}, a form that can be preferentially incorporated into plagioclase feldspars (Brookins, 1989; Lee et al., 2023). Conversely, positive Eu anomalies may occur due to the dissolution of Eu-enriched minerals, like clays (Sousa et al., 2022; Tirumalesh et al., 2012). Chemical weathering and alteration processes can mobilize Eu from these minerals, leading to its enrichment in waters. Similar anomalies have been specifically noted in clay-rich carbonate rocks (Siebert et al., 2012; Tostevin et al., 2016). Another significant anomaly is Gd, calculated as follows (Gao et al., 2023):

$$Gd\ /\ Gd^{*} = \frac{G\,d^{*}}{(0.33Sm^{*} + 0.67Tb^{*})}$$

Where asterisks (*) are used to indicate normalized concentrations, overall, the samples do not show positive Gd anomalies except for two samples (PE18-PE42) with values ranging from 2.2 to 4.8, suggesting potential anthropogenic input (Gao et al., 2023). Among all chemical parameters, pH has the most significant effect on the abundance of dissolved rare earth elements (Gammons et al., 2005; Kaczor-Kurzawa et al., 2022; Migaszewski and Gałuszka, 2015; Noack et al., 2014; Ogawa et al., 2021; Wood et al., 2006). Generally, rare earth elements (REEs) mainly occur as free ions in acidic waters (Dia et al., 2000; Gosselin et al., 1992; Janssen and Verweij, 2003; Leybourne et al., 2000; Miekeley et al., 1992; Migaszewski and Gałuszka, 2015; Noack et al., 2014; Ogawa et al., 2021; Smedley, 1991; Worrall and Pearson, 2001), whereas in more alkaline conditions they are largely removed from solution through adsorption onto oxides and clays, or by co-precipitation with carbonates and phosphates.. The pH values measured in the water samples range from 6 to 8. Within this pH range, REE distribution patterns are influenced by water–rock interactions and complexation with inorganic ligands, particularly carbonates. At these pH levels, LREEs mainly form monocarbonate complexes ($LREECO_3^{+}$), whereas HREEs tend to form more stable dicarbonate complexes, such as $[HREE(CO_3)_2^{-}]$ (Liu et al., 2016; Möller and Bau, 1993; Noack et al., 2014; Tang and Johannesson, 2010; Wei et al., 2022). These behaviors significantly affect the mobility and speciation of REEs in water. In this pH range, the proportion of REEs present as free ionic species (REE^{3+}) is typically low, approximately 5% to 30%, with the rest existing as carbonate or other complexes (Kaczor-Kurzawa et al., 2024; Ogawa et al., 2021). Under more reducing conditions, REEs are released from mineral and organic substrates, resulting in their remobilization into the water. This process often involves the dissolution of Fe/Mn oxyhydroxides and the breakdown of particulate matter that previously sequestered REEs (Johannesson et al., 2011; Liu et al., 2016). Regarding the redox conditions observed in this study, REEs exhibit distinct behaviors depending on the oxidation state of the water. In more oxygen-rich waters, REEs are predominantly removed from solution by adsorption onto mineral surfaces and organic matter, as well as co-precipitation with

colloids and suspended particles (Bau, 1999; Quinn et al., 2004; Tang and Johannesson, 2010; Tweed et al., 2006).

3.1.2. Compositional Data analysis (CoDa), Compositional Pollution Index (CPI), and Multivariate spatial statistics – stochastic approach

To identify atypical observations within the geochemical dataset, the atypicality index was used (Aitchinson, 1986). Within the framework of Compositional Data (CoDA), this index is particularly effective in identifying samples that significantly deviate from the main multivariate pattern, i.e., outliers. The application of this method identified the following samples as potential outliers: PE5, PE17, PE18, PE43, PE51, PE71, PE72. Considering local knowledge of the area regarding hydrography, hydrogeology, urban infrastructure, and human activity, the samples were identified into potentially natural or potentially anthropogenic. To explore these differences visually and statistically, the samples were projected onto a centered log-ratio biplot (Fig. 3.8), which displays the results of principal components analysis (PCA) on compositional data (log-ratio clr transformation) (Aitchison and Greenacre, 2002). The CLR biplot displays differences in the ratios between components for each sample. In this space, the orientation and length of variable vectors (red arrows) show the directions and magnitude of compositional variability. Samples located far from the origin indicate strong associations with specific elements, while those near the origin have more balanced compositions with minimal dominance of individual components. In this case, the first three components (PC1-PC2-PC3) account for 92% of the overall variability. Notably, samples classified as potentially anthropogenic and natural formed distinct clusters, reflecting different geochemical signatures. Natural samples were mainly characterized by REE elements, while anthropogenic samples formed two subgroups: one, consisting of PE43 and PE17, characterized by Cd, Pb, Sb, and Zn; and the second, consisting of PE51 and PE18, characterized by Ni, Mo, Fe, and Cu. The sample PE5, although classified as natural, was excluded from interpretation due to its proximity to the origin, indicating limited compositional variability and low dispersion in clr-space. This multivariate arrangement of the samples supports two important points: 1) the identified outliers reflect true heterogeneity in the study area; 2) the hypothesis that the samples can be classified into natural and anthropogenic groups is supported. To extend this analysis, a clr-biplot including all samples was

generated (Fig. 3.9) with the first three components (PC1-PC2-PC3) explaining 86% of the total variability.

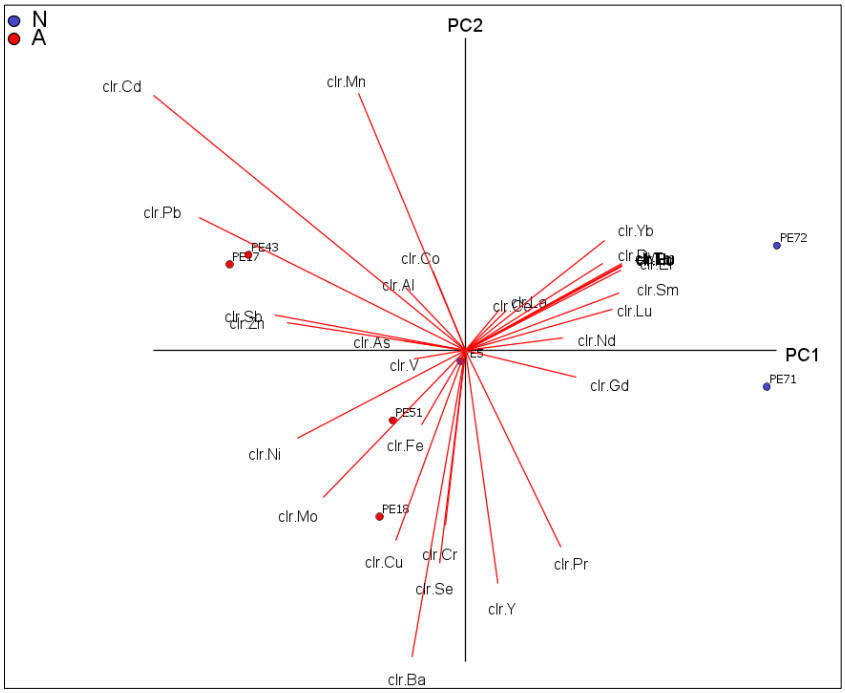

Figure 3.8 – clr-biplot (clr: Centered Log-Ratio transformation) with atypical water samples. Blue: natural samples; red: anthropogenic samples.

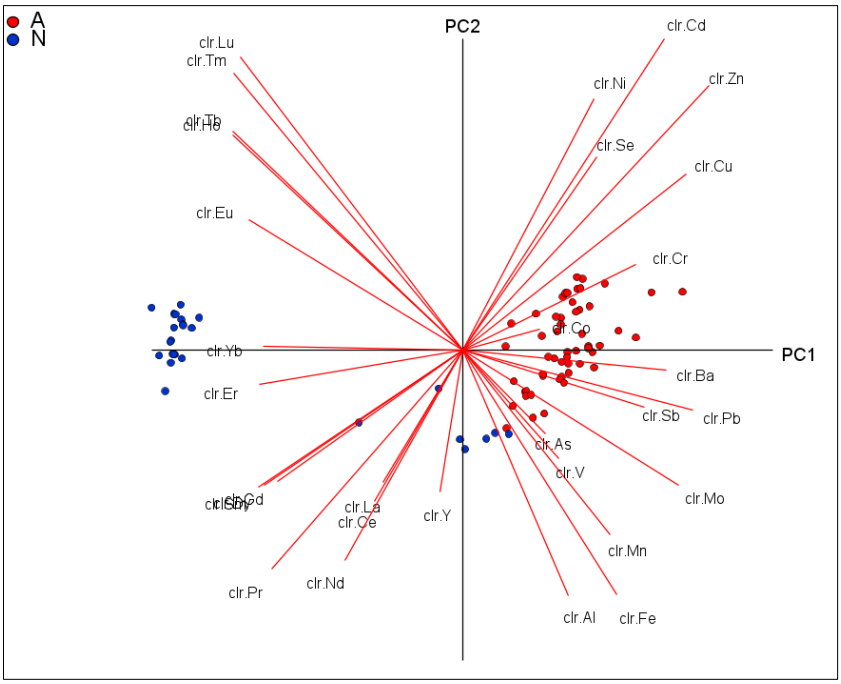

Figure 3.9 - clr-biplot (clr: Centered Log-Ratio transformation) with all water samples. Blue: natural samples; red: anthropogenic samples.

This visualization reinforced the separation between anthropogenic and natural samples. Anthropogenic samples clustered in a region dominated by Ni, Cd, Se, Zn, Cu, Cr, Co, Pb, Sb, Ba, and Mo, indicating contamination from industrial and/or traffic-related sources. In contrast, natural samples were associated with REEs and with a sub-dataset characterized by Al and Fe. Interestingly,

these latter samples were spatially close to anthropogenic samples characterized by As, V, and Mn, suggesting possible overlap in geochemical signatures due to different sources (natural vs. anthropogenic). Based on the evidence from the clr-biplot, a new compositional pollution index (CPI) was created using the criteria proposed by Boente et al. (2022). Elements classified as natural are REEs, and those classified as anthropogenic include Ba, Cd, Co, Cr, Cu, Mo, Ni, Pb, Sb, Se, Zn. The CPI was then calculated as follows:

$$CPI = \sqrt{\frac{NG * NH}{NG + NH}} ln \frac{gm(G)}{gm(H)}$$

Where N represents the number of variables, G and H are the two groups (anthropogenic and natural), and gm is the geometric mean of the variables characterizing each group. This index was calculated for each sample, yielding values ranging from -1.9 (natural conditions) to 20.9 (anthropogenic conditions). The calculated compositional pollution Index (CPI), as a real random variable, meets the assumptions underlying a conventional geostatistical approach (Albuquerque et al., 2024). Spatial probability maps of CPI were generated using the geostatistical modelling method of Sequential Gaussian Simulations (SGS). The new CPI can be considered a regionalized variable (Matheron, 1971), as it is a spatial function that varies across space, influenced by spatial position, but not in a completely random manner. Its value depends on the location's coordinates. This means that the CPI at a specific point is not independent of its surroundings; an expected value for unmeasured points can be inferred based on nearby values (Albuquerque et al., 2017, 2024; Rivoirard, 2005). The spatial continuity of CPI was modelled using an experimental isotropic variogram (Journel and Huijbregts, 1978), and the best-fit model is shown in Fig. 3.10.

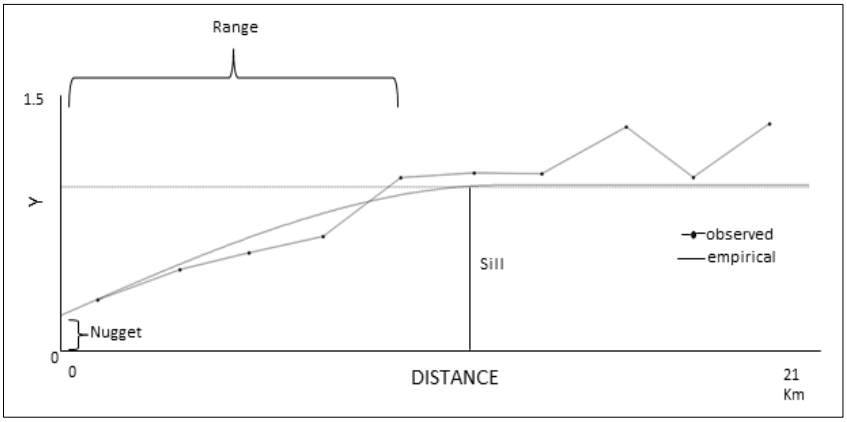

Figure 3.10 - Experimental variogram (points) and theoretical model (solid line). The x-axis shows the distance between pairs of samples, while the y-axis represents the semivariance. The nugget indicates the variance at zero distance, the sill is the maximum value of the semivariance, and the range is the distance beyond which the semivariance stabilizes, indicating the absence of spatial autocorrelation.

To evaluate spatial uncertainty, 100 simulations were conducted using Sequential Gaussian Simulations (SGS) as a conditional stochastic method to model the spatial distribution of CPI values,

generating 100 equally likely scenarios. These simulated maps allowed visualization of spatial variability and identification of pollution hotspot clusters within the study area. Figure 3.11 shows the results of some simulations to demonstrate observed spatial variability. To classify the data into distinct groups while minimizing intra-class variance and maximizing inter-class variance, the Jenks Natural Break classification (Jenks, 1967) was used. This technique provided an optimal arrangement of values for interpreting spatial patterns. The analysis was performed using Space-Stat v.4.0.18 software (BioMedware), as described by Boente et al. (2022) and Albuquerque et al. (2017).

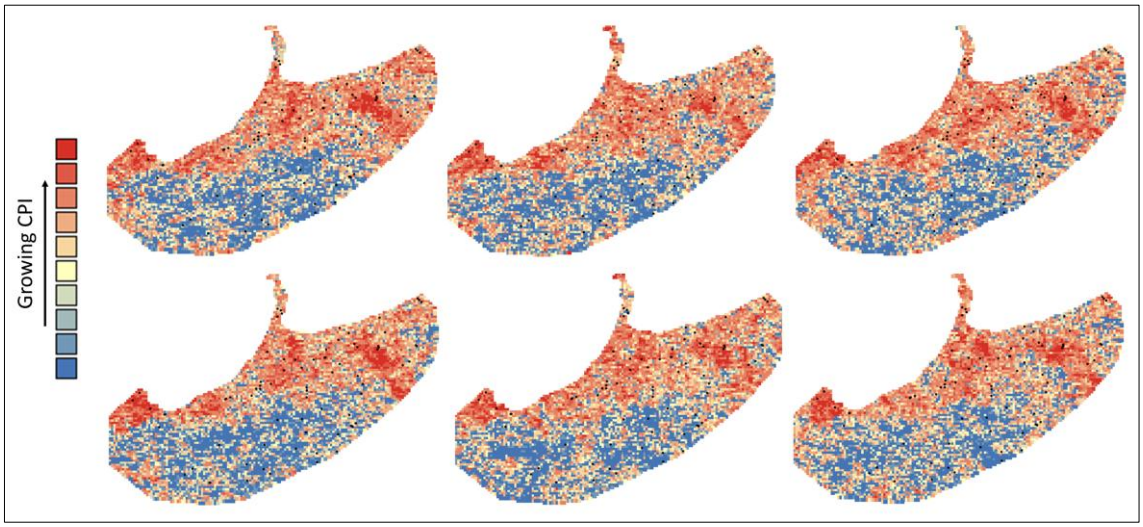

Figure 3.11 - Six different scenarios obtained by sequential Gaussian simulation (SGS) of CPI values.

All simulations consistently identify a primarily natural area (shown in blue) in the western most part of the study area, aligned with the crest of the Peloritani Mountains, as well as a predominantly anthropogenic area (shown in red) along the coastline and within the Sites of National Interest (SIN). Figure 3.12 shows the mean values (MI) and standard deviations, ranging from 1.34 to 8.06, based on the results of 100 simulations.

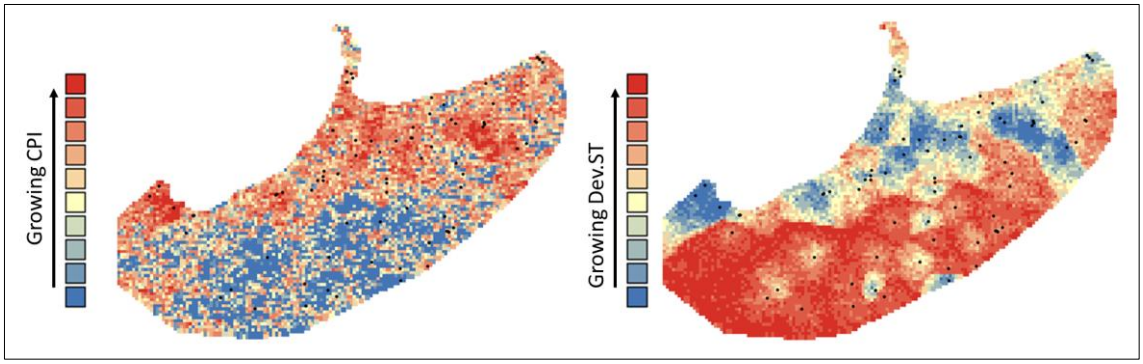

Figure 3.12 – left: Average of 100 Sequential Gaussian Simulation (SGS) of CPI values; right: standard deviation of CPI values.

Overall, areas with high CPI values tend to show low standard deviation, indicating strong agreement among the simulations and limited compositional variability. A similar pattern appears in areas with low CPI values, except some samples display a higher standard deviation, signalling the presence of

compositional variability. The probability maps for exceeding the third quartile (Q3) and falling below the first quartile (Q1), as shown in Figure 3.13, provide valuable insights into the spatial distribution of the CPI and help identify risk clusters. The CPI effectively highlights critical zones, especially along the coastline and within SIN-designated areas, confirming high contamination levels. The two probability maps are complementary and consistent, reinforcing the understanding of the index's spatial distribution.

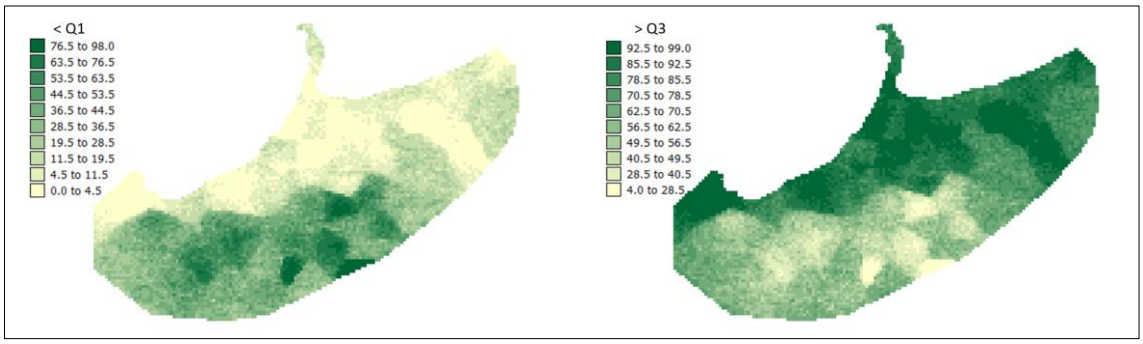

Figure 3.13 - Maps of the probability of not exceeding Q_1 and exceeding Q_3 of CPI values.

To assess the presence of spatial clustering of CPI, the Local G test was applied. This spatial test evaluates the degree of association between a variable and its surrounding neighborhood, making it a robust tool for identifying localized patterns of spatial autocorrelation. The results are displayed on a grid, where each cell takes on a specific color based on the significance and type of clustering (Figure 3.14).

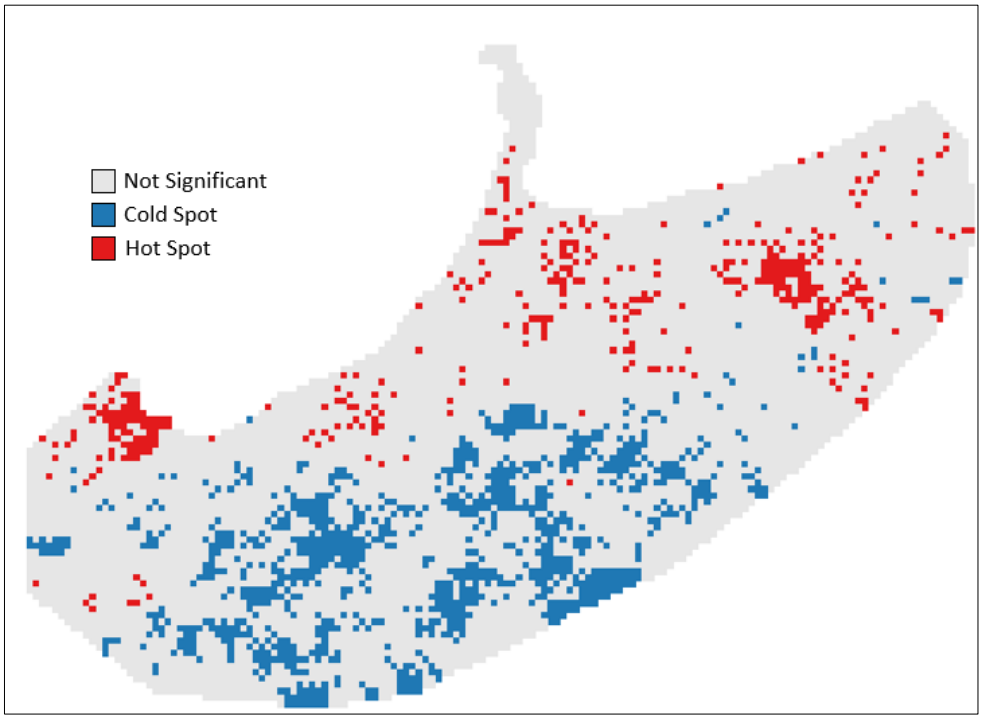

Figure 3.14 - Map of spatial clusters calculated with the Local G test. The red areas indicate hot spots (significantly high values surrounded by high values), while the blue areas represent cold spots (significantly low values surrounded by low values). Neutral values (gray) indicate the absence of significant spatial autocorrelation. The test considers the local spatial structure to identify statistically significant aggregations.

Gray areas indicate that the CPI values in those positions do not show a significant spatial relationship with the surrounding values. These may be transitional zones or areas where local variability is more stochastic. The blue areas represent statistically significant cold spots, indicating clusters where CPI values are markedly lower than the overall mean of the study area. These zones correspond to areas of minimal contamination. In contrast, red areas denote hotspots, where CPI values are significantly higher, highlighting regions of intense contamination. The use of the Local G test provides strong geostatistical evidence of spatial clustering within the CPI dataset. The clustering patterns identified are highly consistent with those revealed by the CPI probability maps, reinforcing the delineation of low-contamination zones in the hinterland and high-contamination areas along the coastline and other localized sectors. This spatial analysis is fundamental for a deeper understanding of the distribution of contamination and could help in targeted environmental monitoring strategies.

After identifying natural areas of low (natural) and high contamination (anthropogenic), a geographical division of the samples was carried out to analyze concentration patterns. The comparison results between the two zones are shown through box plots (Fig. 3.15). Some elements show significant differences in concentration between samples from the heavily contaminated area and those from the natural one, while others display similar distributions across both groups. Elements such as Ba, Cd, Cr, Cu, Mo, Pb, Sb and Zn display greater variability and significantly higher maximum values in the highly contaminated samples. This pattern suggests a direct influence of anthropogenic activities common in the study area (e.g., industrial petrochemical operations, vehicular traffic, urban development). Conversely, elements like Al and Co are more plentiful in samples from the low-contamination area, suggesting a likely geogenic origin. Other elements, including As, Fe, Mn, Ni, Se, and V, exhibit minimal differences in absolute concentrations between the two groups, implying limited discriminatory power. For these elements, a mixed origin is hypothesized, involving both anthropogenic sources and lithological background, especially related to formations in the Aspromonte/Mandanici Unit. Notably, despite their limited significance in absolute concentrations, some of these elements (Ni, and Se) demonstrate strong discriminatory ability within the compositional data analysis (CoDa) framework, based on relative concentrations. Furthermore, it is important to note the consistency between the results obtained from absolute concentration analysis and those from the compositional approach. Many elements that characterize anthropogenic samples in terms of absolute values (Ba, Cd, Cr, Cu, Mo, Pb, Sb, Zn) also serve as discriminating variables in the compositional framework. This agreement between the two methods enhances the reliability of the interpretation. While analyzing absolute concentrations provides a useful initial overview by highlighting potential tracers of human activity, it also has limitations since

many elements exhibit overlapping distributions between the two areas, which reduces their ability to distinguish between them.

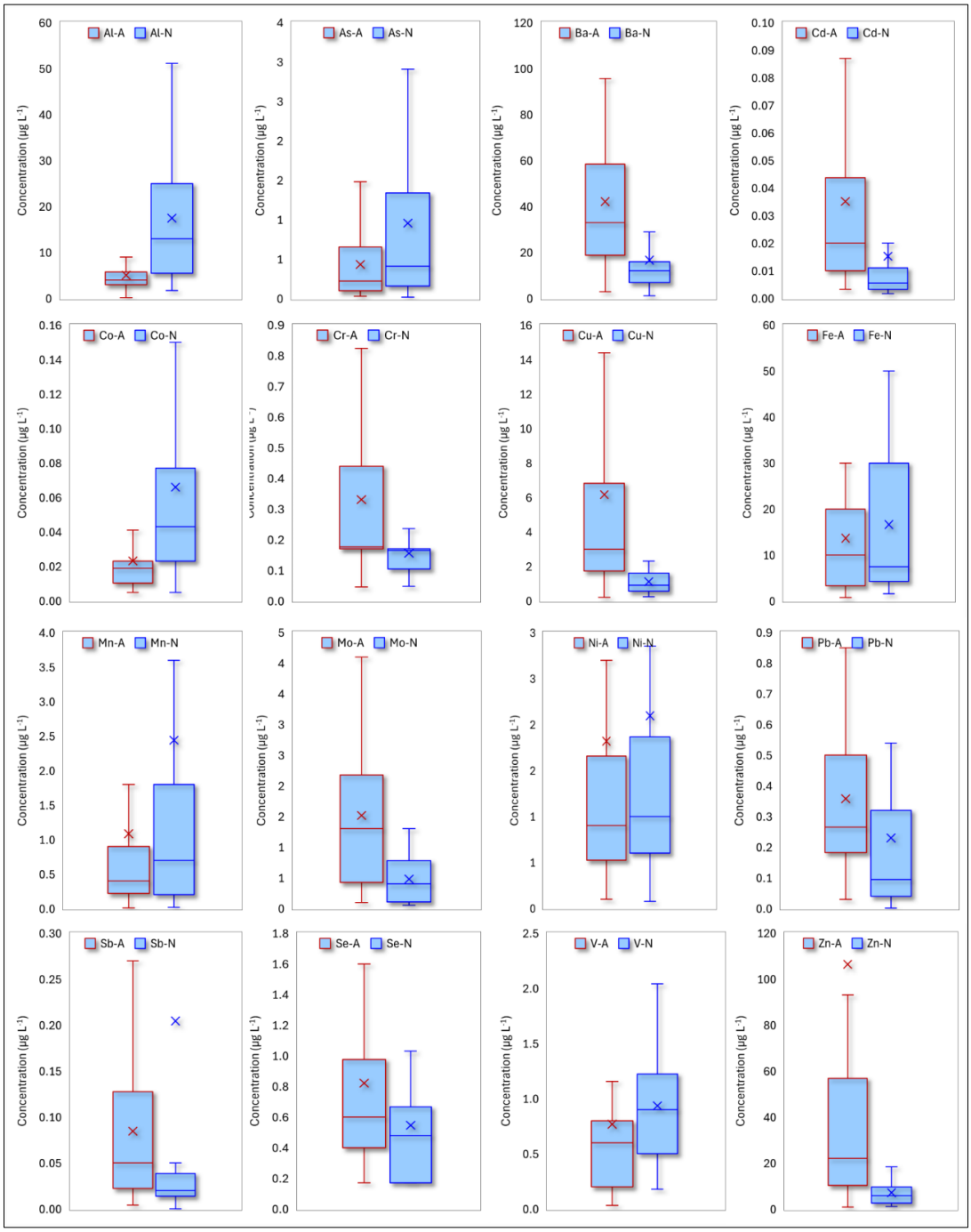

Figure 3.15 – Boxplot of trace element concentrations in water samples. N: Natural zone; A: Anthropogenic zone. The concentrations are expressed in µg L^{-1}.

In contrast, the compositional approach (CoDa) has proven to be more robust and informative, enabling a clearer separation between natural and human sources, even for elements with minimal absolute variation. Notably, elements like Ni, and Se, which are relatively insignificant in absolute concentrations, stand out as highly discriminating when using compositional data. These results show that compositional data analysis provides a more coherent and reliable framework for interpreting complex geochemical datasets, rendering it a preferred tool for identifying contamination sources.

3.2.Topsoil samples: analytical results and statistical evaluation

A total of 74 topsoil samples were collected and analyzed in the Valle del Mela district to characterize the principal geochemical properties governing soil functioning and environmental dynamics. Total organic content (TOC) and pH are critical parameters because they influence nutrient availability, mineral weathering, trace element mobility, and microbial activity (Kobina Mensah and Amoakwah, 2024; Petruzzelli et al., 2025). The pH values ranged from 4.9 to 7.9, reflecting a high degree of variability linked to differences in underlying bedrock (Fabian et al., 2014; Gruba and Socha, 2016; Reuter et al., 2008). According to the USDA soil pH classification (USDA, 2017), 56% of the samples are within the neutral range (6.6-7.3), 28% are slightly acidic (6.1-6.5), and 10% are slightly alkaline (7.4-7.8). About 5% show moderate to extremely acidity (pH < 6) and 1% show a moderately alkaline (7.9-8.4). TOC content, measured following the method of Storer (1984), indicates that 27% of samples have a high organic matter content (>5%), 54% fall within a medium range (2–4%), and the remaining 19% have TOC values below 2%. Particle size analysis further characterizes the soil's physical properties, showing a dominant sand fraction ranging from 55% to 99%, which indicates poor cohesion and high permeability. Gravel content is minimal (1-2%), while the proportions of silt and clay vary across the samples, reflecting some heterogeneity in the processes. Soil grain size varies with geological origin: sandy, gravel-rich textures dominate in metamorphic formations like Aspromonte and Mandanici, while finer textures with higher silt and clay content characterize soils from flysch units such as Capo d'Orlando and Antisicilide-Floresta, reflecting their sedimentary nature. The relative abundance of minerals identified in the soil samples highlights the heterogeneity of the soil types and the diversity of parent geological environments. Table 3.8 summarizes the results of the semi-quantitative X-ray diffraction analysis of topsoil samples, grouped by bedrock lithology, to assess the relationship between the mineralogical composition of surface soils and the petrographic features of the underlying rock units.

*Table 3.8 - Semi-quantitative mineralogical composition of the topsoil samples related to main geological units and deposits. *Clay minerals: mixed-layer clay minerals (Hiller, 2003)*

	Calcite	K-Feldspar	Plagioclase	Quarz	Muscovite	Chlorite	Illite	*Clay minerals	Kaolinite	Gypsum
Aspromonte-Mandanici	1-23%	6-43%	3-45%	16-38%	5-20%	1-36%	5-17%			
Antisicilide-Floresta	1-6%	0-21%	6-27%	27-59%	0-17%	0-11%	4-13%	0-33%	0-3%	
Flysch di Capo d'Orlando	1-30%	4-33%	1-10%	17-38%			2-11%	19-43%	2-6%	
Post orogenic	1-65%	8-38%	0-15%	11-54%	0-29%		0-13%	0-34%	0-8%	0-5%
Deposits	0-36%	17-20%	3-8%	26-38%	0-26%	0-13%	0-24%		0-3%	0-2%

Soils developed on metamorphic bedrock show high and variable levels of feldspars and quartz, along with a significant presence of muscovite, chlorite, and illite as alteration products. These mineral assemblages reflect the lithological complexity of underlying formations, including phyllites, gneisses, amphibolites, mica schists, quartzites, and metabasalts (Barbera et al., 2009; Bonardi et al., 1982; Carbone et al., 2023, 2011; De Vivo, 1982). Soil samples from an Antisicilide-Floresta complex

contain quartz and plagioclase, consistent with clastic sedimentary lithologies. The high percentage of mixed clay minerals, including illite and kaolinite, confirms the clay-rich nature of the parent material, while the presence of calcite indicates a calcarenite component. Conversely, soil overlying the Capo d'Orlando Flysch is dominated by quartz and feldspar, with a significant presence of illite, kaolinite, and other mixed clay minerals, reflecting the turbiditic origin of flysch. Post-orogenic units display a broader mineralogical spectrum, characterized by notably high levels of calcite and quartz, along with feldspars, clays, and occasional gypsum. This variability reflects the heterogeneous composition of these units, which include conglomerates, sands, clays, and evaporitic layers. Younger soils, formed on depositional materials, show a mineralogical signature that mirrors the heterogeneity of their source materials. These soils are mainly composed of quartz and feldspars, with lesser amounts of clay, calcite, and gypsum, indicating inputs from multiple lithologies. The mineralogical data highlight a direct relationship between soil mineralogy and substrate lithology, even considering the influence of pedogenic, weathering, and transport processes. The widespread presence of mixed-layer (interstratified) clays across nearly all units may suggest advanced weathering, associated with the development of mature pedogenic profiles. The radar plot (Fig. 3.16) illustrates the average mineralogical composition of surface soils, grouped by lithological unit. The visualization shows a distinct pattern based on the geological substrate.

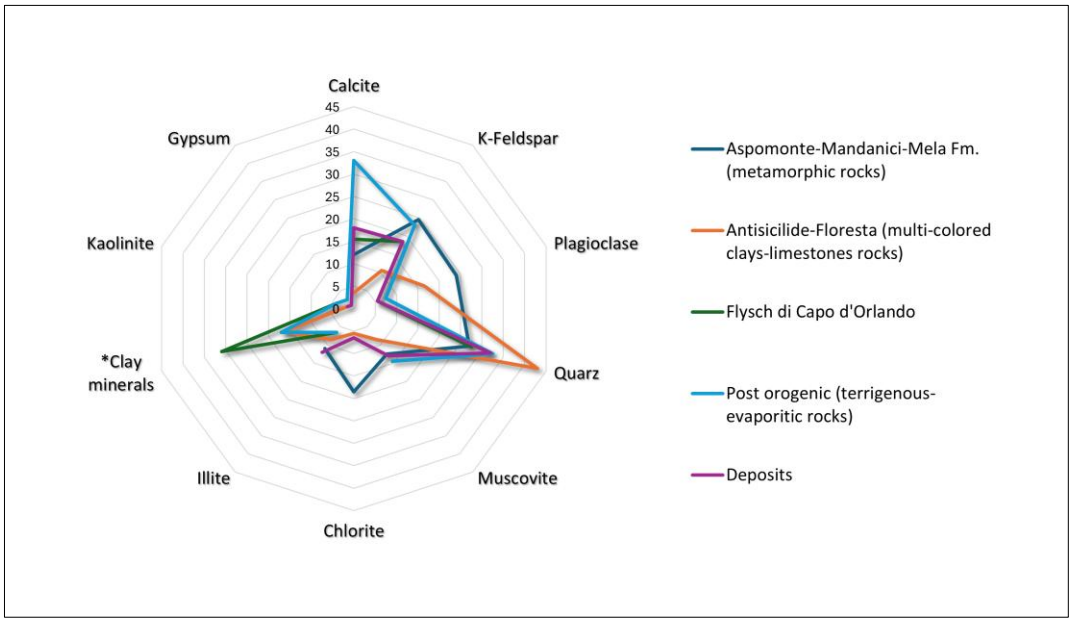

Fig.3.16 - Average mineralogical composition of topsoils, based on semi-quantitative analysis and grouped by bedrock lithology.

Quartz serves as a marker for mature siliciclastic lithologies (e.g., Antisicilide, Flysch), while higher abundances of feldspars and micas characterize metamorphic units (Aspromonte-Mandanici). The presence of interstratified clays is most prominent in finer, more mature sediments. The mineralogical

diversity of post-orogenic and recent soils underscores their polygenic origin and different pedogenic evolution.

3.2.1. Major elements

Table 3.9 reports the main statistical parameters of the major elements measured in surface soil samples. The Shapiro-Wilk test ($p < 0.05$) indicated that the distribution of all analyzed elements is non-normal.

Table 3.9 - Descriptive statistics of major concentrations (%) in topsoil samples. MAD: Median Absolute Deviation, rCV%: robust Coefficient of Variation, Q: Quartile, P: Percentile.

		AVERAGE	*MEDIAN*	*MINIMUM*	*MAXIMUM*	*MAD*	*rCV%*	*KURTOSIS*	*SKEWNEES*	*Q_1*	*Q_3*	*P10*	*P90*
Major elements (%)	Al	2.10	1.89	1.01	5.39	0.40	19	3.9	1.5	1.63	2.48	1.36	3.12
	Ca	2.58	1.28	0.28	17.90	0.74	28	8.5	2.6	0.65	3.46	0.53	6.13
	Fe	3.13	2.97	1.46	4.98	0.61	20	-0.6	0.4	2.55	3.71	2.16	4.33
	K	0.50	0.48	0.21	1.12	0.11	21	1.4	1.0	0.37	0.58	0.30	0.74
	Mg	0.82	0.79	0.37	1.59	0.18	21	0.1	0.7	0.63	0.98	0.52	1.16
	Mn	0.001	0.001	0.0001	0.01	0.0002	27	59	7.3	0.0004	0.0008	0.0002	0.0013
	Na	0.06	0.043	0.023	0.51	0.01	18	46	6.3	0.03	0.05	0.03	0.08
	P	0.11	0.09	0.04	0.33	0.02	19	4.7	1.9	0.08	0.12	0.07	0.18
	Ti	0.08	0.07	0.001	0.20	0.03	42	-0.2	0.5	0.04	0.11	0.02	0.13

The major elements that make up the bulk of the soil matrix exhibit the highest concentrations. Their variability reflects differences in mineralogical composition, parent rock type, weathering processes, as well as broader environmental and climatic factors influencing soil formation. All elements exhibit positive skewness values. Similarly, most elements demonstrate positive kurtosis values, indicating that their distributions are mostly leptokurtic. Figure 3.17 shows a comparison of soil samples categorized by lithological type. Soils developed on metamorphic bedrock show elevated contents of Fe, Mn, Mg, and Al, consistent with a mineralogical composition rich in phyllosilicates. Low levels of Ca and Na indicate feldspar weathering, while moderate Al and K concentrations suggest the presence of muscovite, chlorite, or illite. Soils overlying flysch lithologies are depleted in Ca, Na, K, Mn, and P, reflecting the siliciclastic nature of the substrate, which is poor in carbonates and alkaline elements. Intermediate levels of Al, Fe, Mn, and Ti are characteristic of silicate minerals, such as clays, quartz, micas, and feldspars. Soils over Antisicilidi Units and the Floresta Formation show low concentrations of most elements, especially Ca, Fe, Mg, Mn, Ti, and P, indicating limited alteration or development on already depleted substrates. The near-total absence of carbonate minerals, despite the calcareous bedrock, suggests that decarbonation processes and the selective mobilization of Ca occurred during the initial stages of surface weathering (Dupré et al., 2003; Egli et al., 2008). Slightly elevated concentrations of Al and K suggest the presence of resistant clay minerals, such as illite.

Finally, post-orogenic soils exhibit variable compositions, particularly in Ca, Mg, and Na, due to the alternating presence of evaporitic (gypsum, halides) and detrital components.

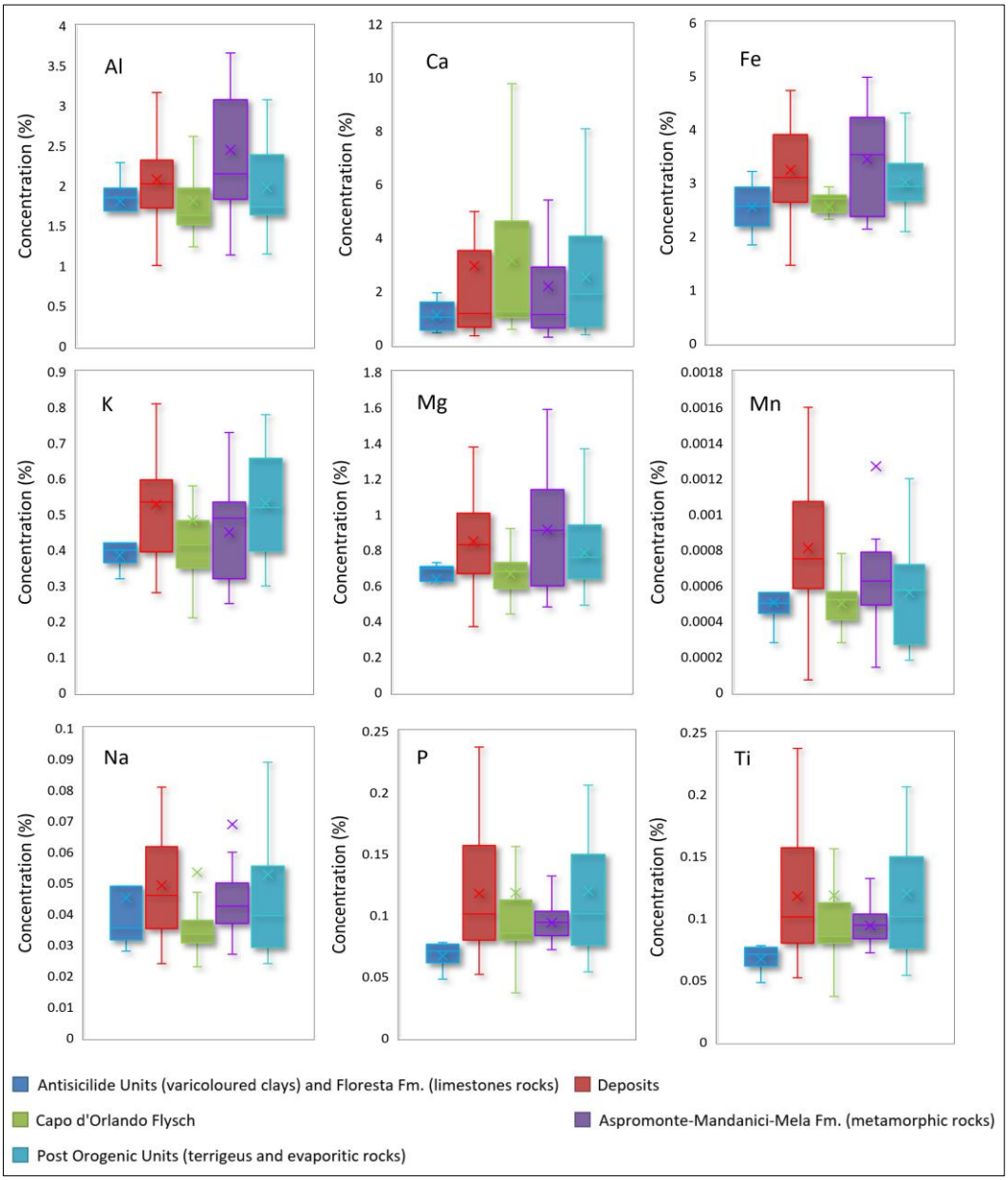

Figure 3.17: Box plot of major element concentrations (Al, Ca, Fe, K, Mg, Mn, Na, P, Ti) in soil samples, divided by bedrock lithology. Median: horizontal line; first and third quartiles: box limits; minimum and maximum values: whiskers; mean: x.

These soils reflect the heterogeneous composition of the substrate and the variability of local pedogenic processes. The Chemical Index of Alteration (CIA), proposed by Nesbitt and Young, (1982), is widely used to assess the intensity of chemical weathering in soils. The CIA was calculated as follows:

$$CIA = \frac{m\,Al_2O_3}{(mAl_2O_3 + mCaO + mNa_2O + mK_2O)} * 100$$

where “m” denotes molar concentrations. The index is dimensionless, with values typically ranging from 0 to 100. CIA values below 50 indicate low weathering intensity. In contrast, values between 80 and 100 are indicative of advanced chemical weathering, characterized by significant depletion of mobile base cations (Ca, Na, and K) and relative enrichment of Al-bearing phases (Algeo et al., 2025; Fedo et al., 1995; Nesbitt and Young, 1982). Topsoil samples revealed that 53% exhibit CIA values below 50, reflecting limited chemical weathering. About30% of the samples fall within the 60-80 range, indicating moderate weathering and increased mobility of Na and Ca. The 15% display values between 50-60, suggesting that initial weathering mainly affects Ca and Na depletion. Only 3% of the samples showed CIA values above 80, consistent with intense weathering and residual Al enrichment. The distribution of CIA values by lithology underscores the significant influence of parent material composition on the extent and progression of chemical weathering processes.

3.2.2. Trace Elements and Rare Earth Elements (REEs)

Unlike major elements, the distribution pattern of trace elements reflects not only the geogenic influence of local lithology but also significant anthropogenic contributions from multiple inputs within the study area. Table 3.10 reports the main statistical parameters for trace elements. Trace element concentrations exhibit marked variability across the study area, indicating substantial spatial heterogeneity. This variation, often spanning several orders of magnitude between samples, can be attributed to multiple, overlapping factors. These include the presence of specific accessory minerals, the influence of localized pedogenic processes, or the impact of human activities.

Table 3.10 - Descriptive statistics of trace element concentrations in topsoil samples. MAD: Median Absolute Deviation, rCV%: robust Coefficient of Variation, Q: Quartile, P: Percentile. Data in μg g^{-1}.

		AVERAGE	*MEDIAN*	*MINIMUM*	*MAXIMUM*	*MAD*	*rCV%*	*KURTOSIS*	*SKEWNEES*	*Q_1*	*Q_3*	*P10*	*P90*
Trace elements (μg g^{-1})	As	8.11	6.15	0.70	112	2.15	27	59	7.3	3.68	7.98	2.36	12.6
	Ba	130	118	50.9	418	27.0	21	7.2	2.1	95.4	147.5	76.3	195
	Cd	0.17	0.16	0.03	0.64	0.06	36	6.8	1.9	0.10	0.22	0.08	0.28
	Co	12.4	11.6	5.90	26.6	2.65	21	0.5	0.8	9.33	15.7	7.69	18.4
	Cr	41.5	38.0	15.0	95.0	10.5	25	0.6	0.9	29.0	52.0	23.0	63.7
	Cu	50.8	44.2	15.3	122	16.7	33	0.0	0.8	29.5	66.6	23.8	85.8
	Mo	1.04	0.97	0.15	3.43	0.31	29	4.7	1.9	0.64	1.23	0.49	1.66
	Ni	29.3	26.6	11.9	76.8	4.90	17	2.6	1.3	21.9	35.5	16.8	45.2
	Pb	28.6	18.8	6.8	219	5.95	21	19	3.9	13.8	31.7	11.2	45.8
	Sb	0.67	0.34	0.04	9.24	0.16	24	30	5.1	0.21	0.60	0.13	1.13
	Se	0.51	0.50	0.07	1.30	0.10	20	0.9	0.3	0.40	0.60	0.10	0.87
	V	59.4	52.5	25.0	146	14.5	24	1.6	1.2	40.3	73.8	36.0	88.4
	Zn	119	95.7	37.3	1120	16.9	14	54	6.9	79.7	113	68.4	148

Many of the analyzed elements show high variability, with rCV% values over 20%. This suggests the presence of significant outliers, which may result from a mix of geogenic processes (such as

variations in parent material or mineralogy) and anthropogenic inputs (including industrial emissions, historical contamination, or vehicle traffic). The Kurtosis coefficients for several elements, especially As, Ba, Cd, Pb, Sb, and Zn, exceed 7, indicating leptokurtic distributions. This means that the datasets for these elements have heavier tails than a normal distribution. Conversely, the remaining elements exhibit platykurtic distributions, suggesting more consistent data dispersion with fewer extreme values. Similarly, the skewness index for the same group of elements (As, Ba, Cd, Pb, Sb, and Zn) is greater than +2, indicating strong right skewness in their distributions. This asymmetry implies a long tail toward higher concentrations, likely due to localized enrichment from human activities or specific geochemical anomalies.

A comparative analysis was conducted and summarized in the heatmap in Figure 3.18, which displays the median concentrations of trace elements in topsoil samples, categorized by the lithology of the underlying bedrock.

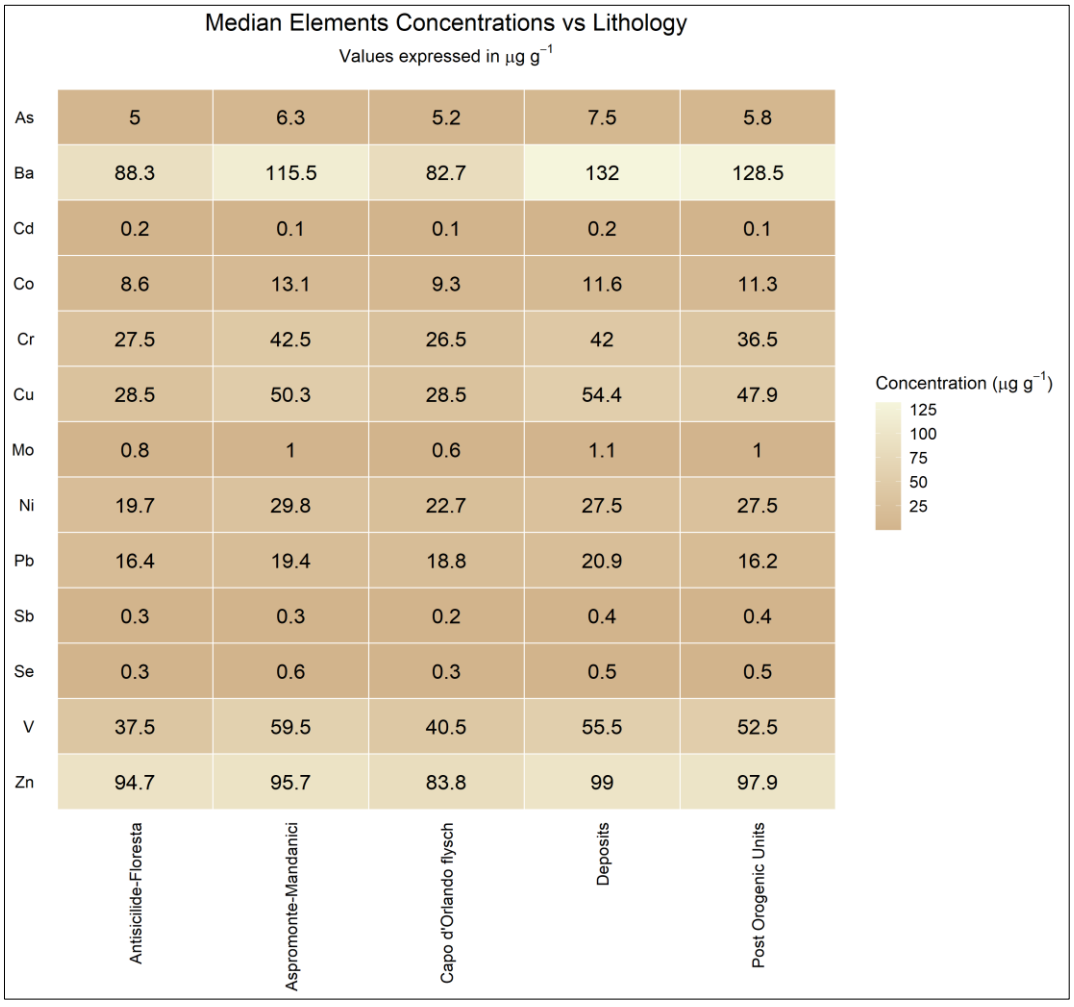

Figure 3.18 - Heatmap of median element concentrations in topsoil samples by lithological unit. Data in μg g^{-1}.

The highest concentrations are observed for elements like Ba, Cr, Cu, Ni, Pb, V, and Zn. Notably, the Aspromonte-Mandanici lithological formation (metamorphic rocks), along with the post-orogenic

units (terrigenous and evaporitic rocks), exhibit the highest median concentrations for most of these elements. In contrast, the Varicolored Clays (Antisicile Formation) and the Capo d'Orlando Flysch display lower concentrations. This differentiation supports the role of bedrock composition as a primary source of trace elements, released through chemical weathering and pedogenesis processes. However, analyzing absolute concentrations alone does not allow for a clear distinction between lithogenic and anthropogenic sources. Elements such as Pb, Zn, Cu, Ni, and Cr are also known to originate from anthropogenic activities, including vehicular emissions, industrial processes, and agricultural practices. From this perspective, the observed spatial heterogeneity likely reflects the superimposition of geogenic and anthropogenic signals linked to local environmental pressures.

The distribution and availability of rare earth elements in the environment depend on the source material, as well as geochemical and biological processes (Cidu et al., 2013; Zhang et al., 2001). The median total REEs content (ΣREEs from La to Lu) in the analyzed soils is 107.6 μg g^{-1} (Table 3.11).

Table 3.11 - Average and median REE concentrations in topsoil samples.

	Rare Earth Elements (μg g^{-1})														
	Y	La	Ce	Pr	Nd	Sm	Eu	Gd	Tb	Dy	Ho	Er	Tm	Yb	Lu
AVERAGE	11.9	23.7	46.3	5.24	20.8	4.04	0.70	3.66	0.49	2.63	0.45	1.23	0.16	0.90	0.11
MEDIAN	11.5	22.8	46.1	5.00	20.0	3.90	0.70	3.55	0.50	2.55	0.40	1.20	0.15	0.80	0.10

From Table 3.11, the median concentrations of the individual lantadines (La to Lu) and yttrium in the surface soils decrease in the following order:

Ce>La>Nd>Y>Pr>Sm>Gd>Dy>Er>Yb>Eu>Tb>Ho>Tm>Lu.

Ce, La, and Nd appear to be the most abundant REEs, with median concentrations of 46.05 μg g^{-1}, 22.75 μg g^{-1}, and 19.95 μg g^{-1}, respectively. A second group of REE elements shows median concentrations ranging from 5 μg g^{-1} (Pr) to 1.2 μg g^{-1} (Er). The remaining REEs have lower median contents, from 0.8 μg g^{-1} for Yb to 0.1 μg g^{-1} for Lu. The observed abundances are consistent with values reported in the literature (Rezaei et al., 2025) for total REE concentrations, with cerium being the most abundant, followed by lanthanum. Generally, LREEs (light REEs) are more abundant than HREEs (heavy REEs) (Tab.3.12). To evaluate the variations and their distribution pattern of REE abundance, it is standard to normalize the data to a geochemical reference. In this study, normalization was performed using chondrites (the reference values proposed by Anders E. and Ebihara, M. (1982).

Table 3.12 - Average and median values of total, light (LREE), medium (MREE), heavy (HREE) Rare Earth Element (REE) concentrations and the LREE/HREE ratio. Data in μg g^{-1}.

	∑REE	*∑LREE*	*∑MREE*	*∑HREE*	*∑LREE/∑HREE*
AVERAGE	390	277	82.6	29.6	9.51
MEDIAN	372	267	82.6	27.8	9.28

In the analyzed topsoil samples, LREEs dominate over HREEs, consistent with the distribution pattern observed in the water samples. The fractionation process, in which one or more REEs become depleted or enriched relative to others, can be evaluated through the LREE/HREE ratio. The calculated LREE/HREE ratio is 9.62, indicating a consistent pattern of preferential enrichment of LREEs and depletion of HREEs (Chen and Yang, 2010; Ion and Cosac, 2023). The REE profiles (Fig. 3.19) seem to be influenced by the composition of the parent material.

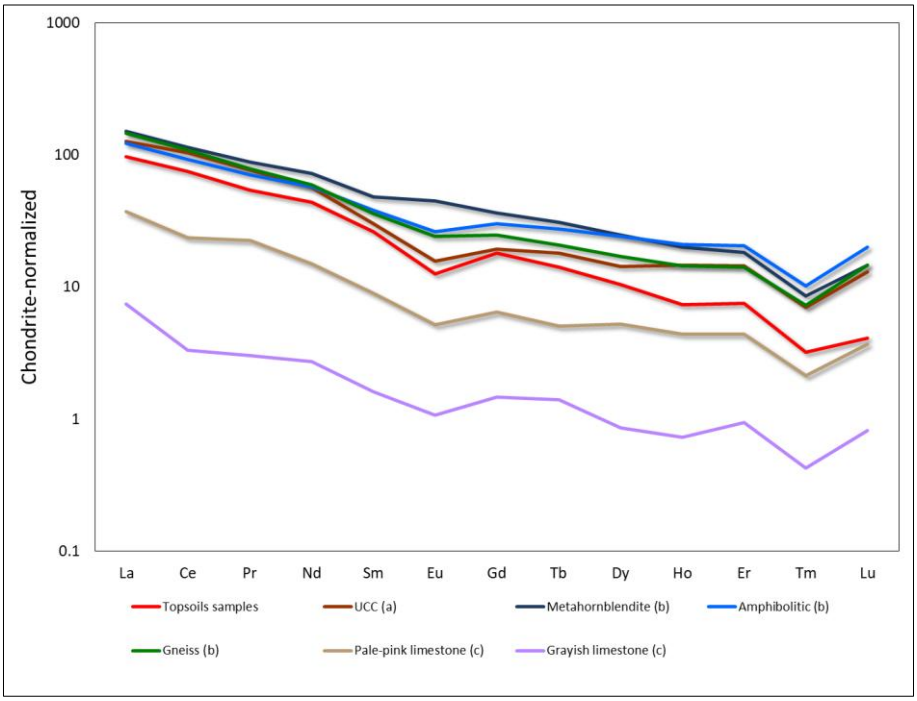

Figure 3.19 - Chondrite-normalized rare-earth element spider diagram for the median of topsoil samples and reference about: (a) Upper Continental Crust (UCC) (McLennan, 2001; Taylor and McLennan, 1985); (b) Metamorphic substrate (Duplay et al., 2014; Messina, unpublished), (c) sedimentary substrate (Messina et al., 2004b, 2004a).

The pattern of the topsoil samples shows an apparent similarity to that of the Upper Continental Crust (UCC, McLennan, 2001; Taylor and McLennan, 1985). This suggests that the soil composition is directly influenced by the Earth's crust, or by a mixture of rocks that, overall, have a similar composition to the UCC. Indeed, examining the patterns of local metamorphic and carbonate rocks reveals a generally excellent similarity, albeit with slightly different enrichments and depletions. This clearly indicates that the surface soil samples have a geochemical composition dominated by the bedrock rocks.

The calculation of elemental anomalies for Ce and Eu revealed that 81% of the samples had a positive Ce anomaly, while the remaining 19% showed a negative anomaly (Barrat et al., 2023; Lawrence et al., 2006; Lawrence and Kamber, 2006). Generally, the presence and fractionation of REEs, like other elements, are influenced by weathering processes driven by a combination of hydrogeological, geochemical, and biological factors, including human activities (Saiano and Scalenghe, 2019). The median concentrations of La and Ce in the soil samples (22.8 μg g^{-1} and 46.1 μg g^{-1}, respectively)

exceed the threshold values established for European agricultural soils (La: 14 µg g^{-1}; Ce: 28.4 µg g^{-1}, Reimann et al., 2018). Positive Gd anomalies were observed in the analyzed samples, indicating human contributions to soil composition (Duplay et al., 2014; Kulaksız and Bau, 2011). The wide variability in the concentrations of both elements across the study area highlights a strong dependence on the underlying bedrock, which is notably heterogeneous. Nevertheless, an anthropogenic contribution cannot be ruled out, since REEs incorporated in zeolite based catalysts employed in petroleum refining represent robust geochemical traces of refinery derived emissions (Kitto et al., 1992; Kulkarni et al., 2006; Moreno et al., 2012, 2008; Olmez et al., 1988; Sánchez De La Campa et al., 2011; Tian et al., 2020).

3.2.3. Data analysis (CoDa), Compositional Pollution Index (CPI), and Multivariate spatial statistics – stochastic approach

The atypicality index, used to identify differences within a dataset, flagged the following potential outliers: SP17-SP19-SP44-SP59-SP71-SP72-SP74. These samples were plotted on a clr biplot (Fig. 3.20), showing their classification as either potentially anthropogenic or natural. The first three components (PC1-PC2-PC3) explain 87% of the total variability. The biplot clearly separates natural samples (in red) from anthropogenic samples (in blue), indicating significant differences in their chemical composition, particularly in the clr log-ratios between the two groups.

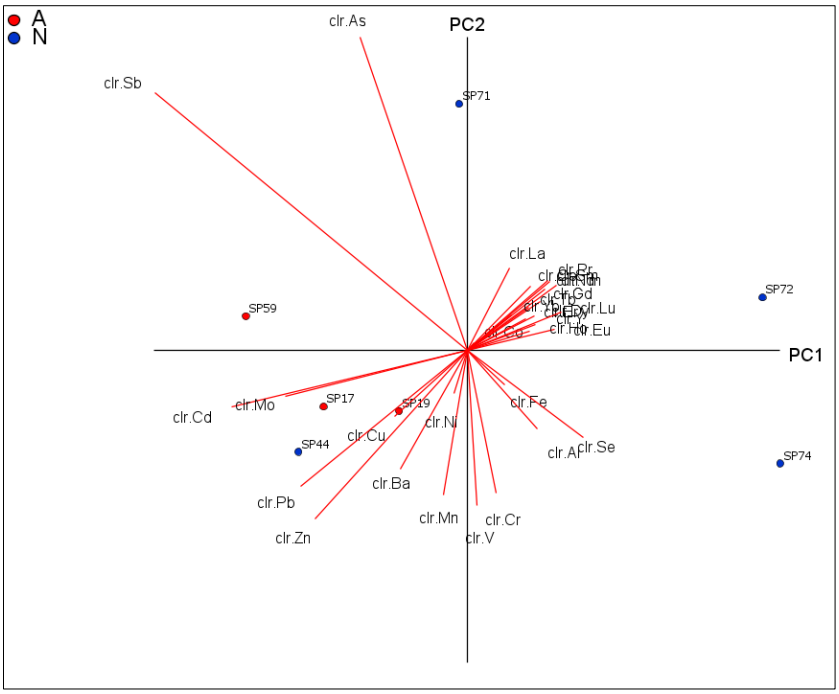

Figure 3.20: clr-biplot of the atypical samples identified by the Atypical Index. Samples classified as natural are in blue, while those classified as anthropogenic are in red.

The samples identified as natural are mainly associated with REEs, Co, Se, Al, Fe, and As, while Mn, Ni, Ba, Cu, Zn, Pb, Mo, Cd, and Sb characterize the samples identified as anthropogenic. An

exception is sample SP44; despite being classified as natural, it appears within the cluster of anthropogenic samples in the biplot. This anomaly can be attributed to its geographic location within a transitional zone where both human activities and natural inputs blend. Even in surface soil samples, the unusual values highlight and reflect the unique environmental features of the study area.A clr-biplot was then repeated with all samples (Fig. 3.21).

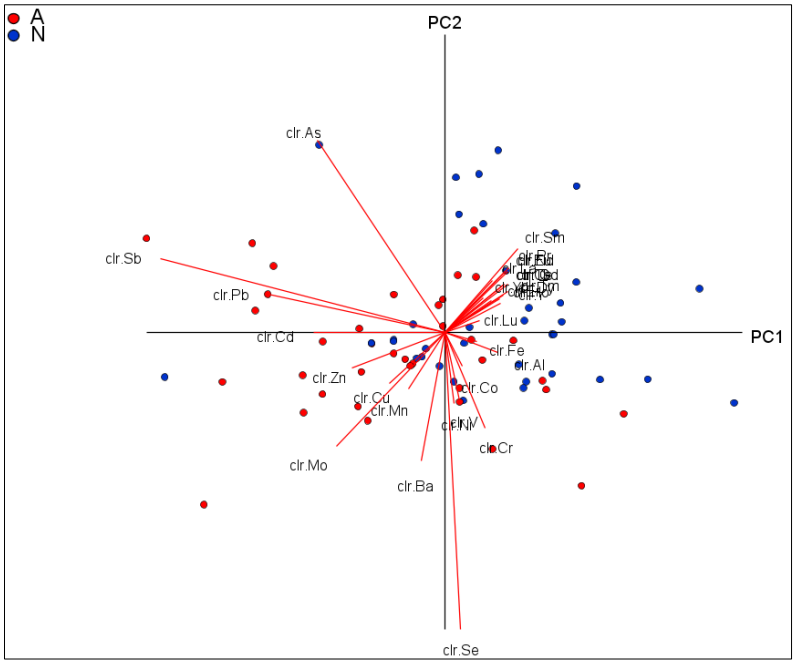

Figure 3.21: clr-biplot of the topsoil samples. Samples classified as natural are in blue, while those classified as anthropogenic are in red.

The first three components (PC1-PC2-PC3) explain 68% of the total variability. A clear distinction between natural and anthropogenic samples is evident, although the separation is not absolute. Samples influenced by anthropogenic sources predominantly cluster on the left side of the graph and show stronger associations with elements such as Ba, Cd, Cr, Mo, Pb, Sb, Se, Zn, which are commonly recognized as indicators of human activity. In contrast, samples of mainly natural origin tend to cluster toward the right side of the graph, displaying a closer association with rare earth elements (REEs). Based on the elemental composition that distinguishes natural from anthropogenic samples, a new compositional pollution index (CPI) was developed using expert-defined criteria and a targeted selection of elements (Boente et al. 2022). The construction of this index, described in detail in subparagraph vv.ss2.3.1., involved calculating CPI values for each soil sample, ranging from -0.16, indicating mainly natural conditions, to 5.38, reflecting significant anthropogenic influence. Spatial modelling of the CPI included calculating the experimental isotropic variogram followed by applying Sequential Gaussian Simulation (SGS) to generate 100 simulations as a conditional

stochastic model of the CPI distribution (Space-Stat software v.4.0.18BioMedware, was used for the simulation procedure: Boente et al. 2022; Albuquerque et al. 2017).

These simulations provided equally probable scenarios, allowing for the assessment of spatial variability and the identification of pollution hotspot clusters within the study area. Representative simulations are shown in Figure 3.22. To categorize ICP CPI values, the Jenks Natural Break method (Jenks 1967) was used. This approach minimizes variance within each class while maximizing variance between classes, offering an optimal data partitioning.

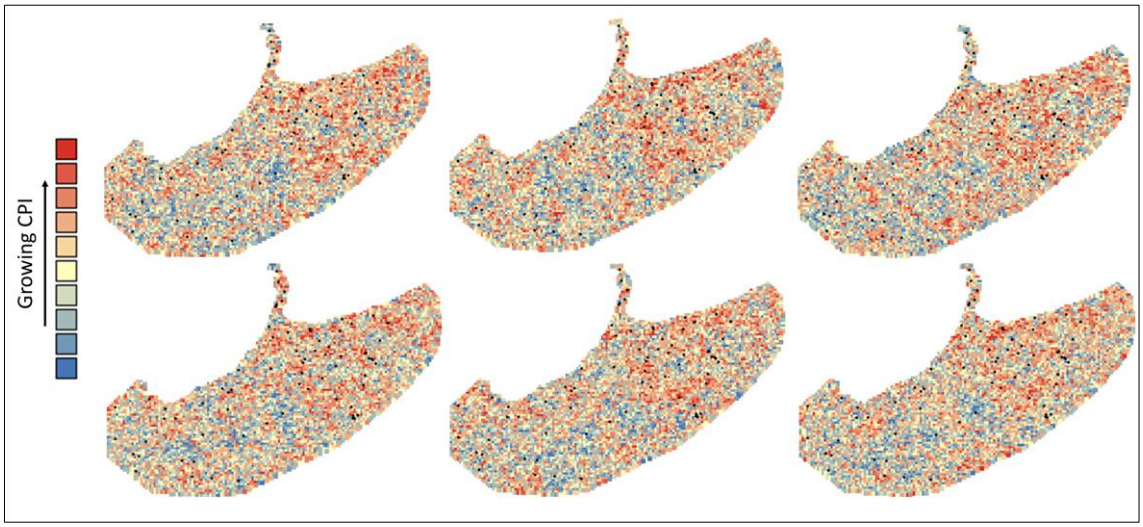

Figure 3.22 - Six different scenarios obtained by sequential Gaussian simulation (SGS) of CPI values.

All simulations consistently identify a predominantly natural area, shown in blue, located in the westernmost sector of the study area, and a mainly anthropogenic zone, marked in red, along the coastline, particularly in sites classified as Sites of National Interest (SIN). Figure 3.23 displays the mean spatial image (MI) and the associated standard deviation from the simulations, which range from 0.8 to 1.3.

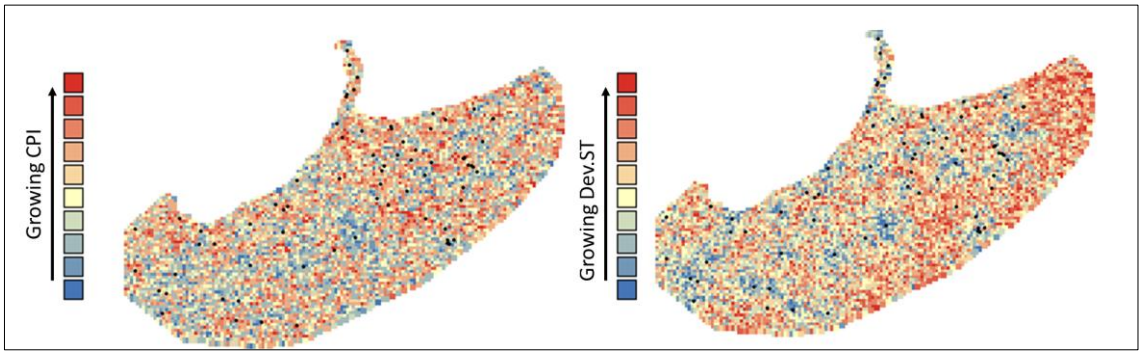

Figure 3.23 - left: Average of 100 Sequential Gaussian Simulation (SGS) of CPI values; right: standard deviation of CPI values.

Overall, standard deviation values stay low throughout the study area, with higher uncertainty in unsampled or poorly characterized areas. The probability maps of exceeding the third quartile (Q3) and of not exceeding the first quartile (Q1) provide valuable insights into the spatial distribution of

the pollution index and help identify clustered risk areas (Fig. 3.24). In the Q3 exceedance map, dark green regions highlight areas with a high probability of increased anthropogenic impact, closely matching the designation of SIN sites. Conversely, dark green zones in the Q1 not-exceedance map indicate areas with a high likelihood of minimal anthropogenic influence, reinforcing their classification as mainly natural. Along the coastline, a mosaic of colors depicts a transitional zone affected by both urban settlements and natural environments.

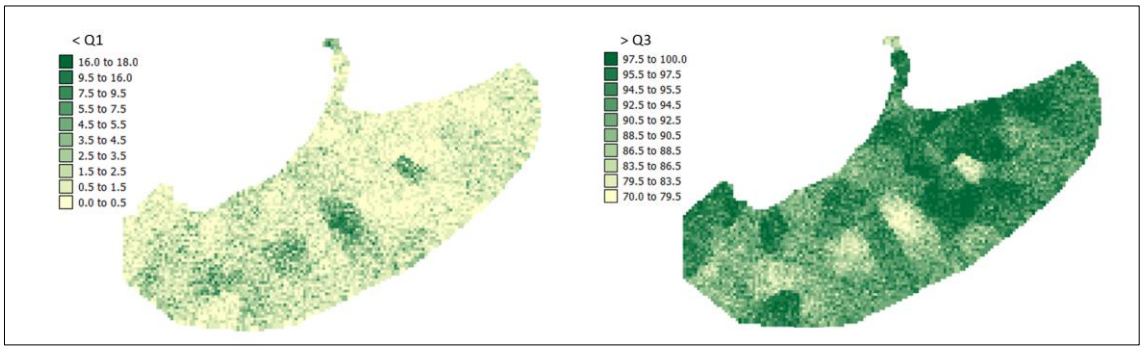

Figure 3.24 - Maps of the probability of not exceeding Q_1 and exceeding Q_3 of CPI values.

To further investigate spatial clustering patterns, the Local G test was applied, and the result is presented in Figure 3.25.

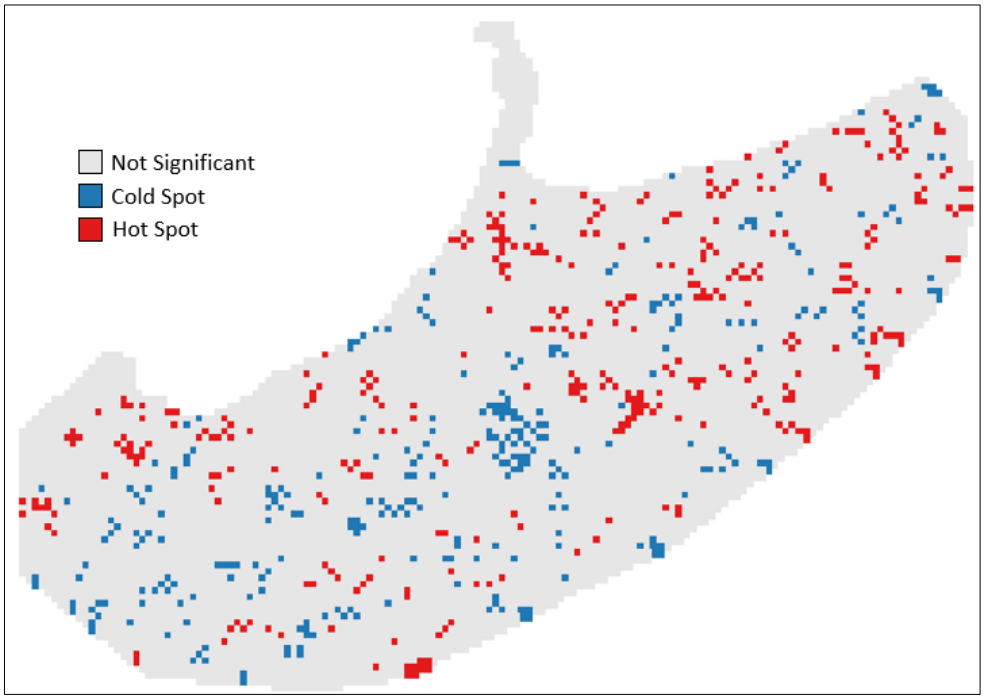

Figure 3.25 - Map of spatial clusters calculated with the Local G test. The red areas indicate hot spots (significantly high values surrounded by high values), while the blue areas represent cold spots (significantly low values surrounded by low values). Neutral values (gray) indicate the absence of significant spatial autocorrelation. The test considers the local spatial structure to identify statistically significant aggregations.

The Local G cluster map provides strong spatial evidence supporting the previous findings by clearly distinguishing hotspot sites (SIN and coastal areas) from coldspot areas. The outcomes of the Local

G test show high concordance with the CPI probability maps, confirming the presence of well-defined low-contamination zones inland and high-contamination zones along the coast and in other localized sectors. This geostatistical analysis is essential for understanding the spatial dynamics of contamination and serves as a fundamental tool for informing risk assessment and environmental management strategies. After identifying the low (natural) and high (anthropogenic) contamination areas, the samples were geographically divided to analyze their concentration trends. The comparison results between the two zones are shown in box plots (Fig. 3.26).

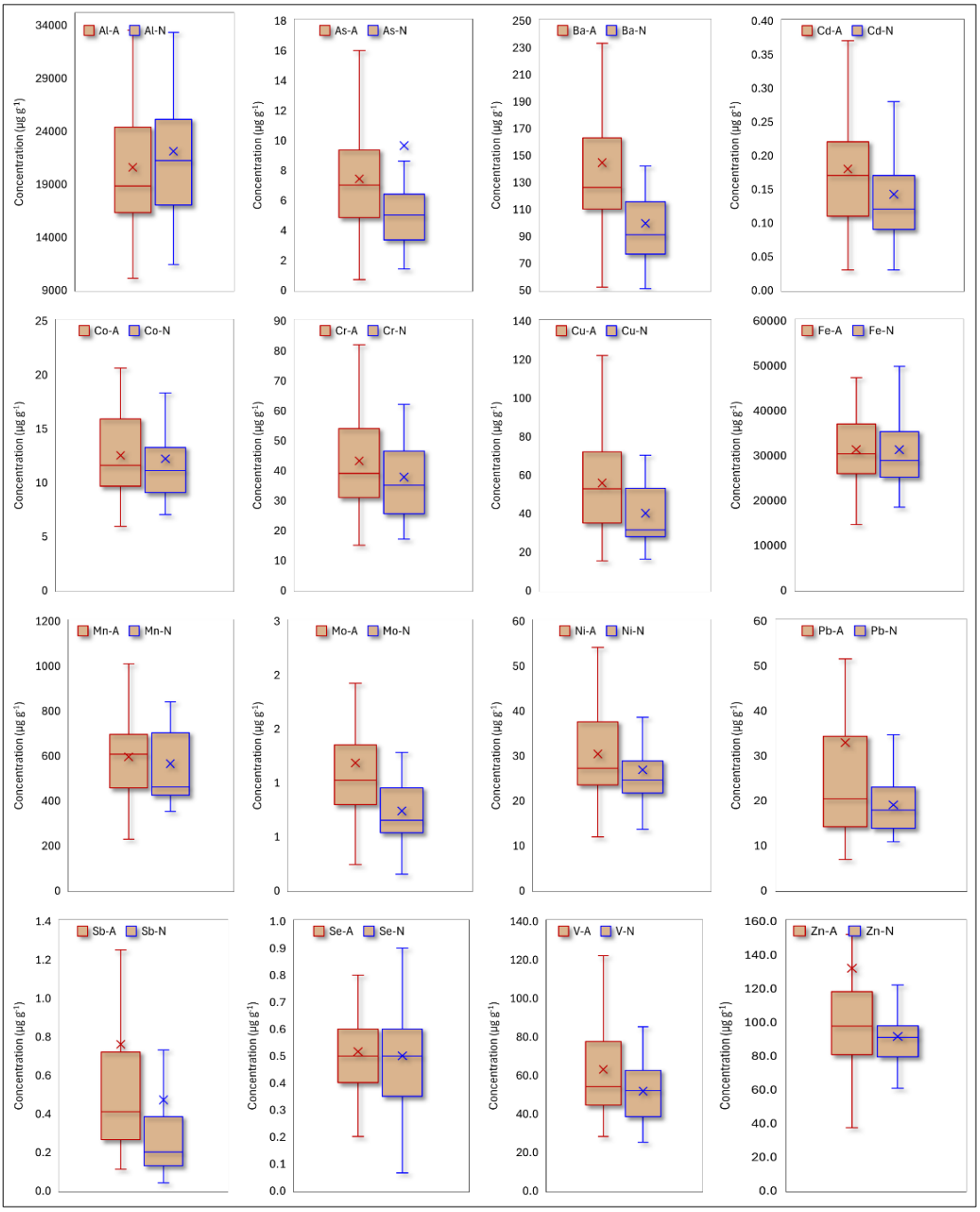

Figure 3.26 - Boxplot of trace element concentrations in topsoil samples. N: Natural zone; A: Anthropogenic zone. Data expressed in µg g^{-1}.

Some elements exhibit significant differences in concentration between samples from the highly contaminated area and those from the natural area, while others display similar distributions in both groups. Elements such as As, Ba, Cd, Cr, Cu, Mo, Ni, Pb, Sb, V, and Zn demonstrate greater variability and significantly higher maximum values in the highly contaminated anthropogenic samples. This trend indicates a direct influence of dominant anthropogenic activities in the study area (e.g., petrochemical industry, vehicular traffic, urban development). Conversely, Al is more abundant in samples from the natural area, suggesting a likely geogenic origin. Other elements, including Co, Fe, Mn, and Se, exhibit minimal differences in absolute concentrations between the two groups, reflecting a limited capacity to discriminate due to their likely mixed origin, which involves both anthropogenic inputs and lithological background. As with the water samples, some compatibility exists between relative and absolute concentrations, particularly for elements such as Ba, Cd, Cr, Mo, Pb, Sb, and Zn, which also characterize anthropogenic samples through a compositional approach, and for elements like Co, Fe, and Mn, which are less effective in distinguishing the groups. The consistency between the two methods confirms the reliability of the results. The analysis of absolute concentrations provides preliminary indications, but with limited discriminatory power. In contrast, the compositional approach (CoDa) is more robust, better distinguishing between natural and anthropogenic sources, highlighting elements that would otherwise be marginal, such as Se. The CoDa method thus confirms itself as the most effective tool for interpreting complex geochemical data.

3.3.Pine needle samples: analytical results and statistical evaluation

The genus *Pinus* is among the most widely distributed taxa across the northern hemisphere, with species occurring in both natural forest ecosystems and ex situ conservation contexts such as botanical gardens (Parzych et al., 2017). Due to their morphological and physiological traits, pine needles have been widely employed as passive biomonitors for evaluating of atmospheric contamination (Kord et al., 2010). Their role in monitoring trace metal accumulation has been extensively studied in various environmental settings, highly urbanized environments to remote background areas, over the past few decades (Zeiner and Juranović Cindrić, 2021). The mechanisms by which plants take up metals are essentially twofold: uptake from the rhizosphere through the root system and direct atmospheric deposition *via* wet and dry processes (Juranović Cindrić et al., 2019). Therefore, plant tissues serve as effective integrative matrices for environmental monitoring, with the amount and type of pollutants they accumulate depending greatly on spatial and temporal factors (Chen et al., 2022). As highlighted by Holoubek et al. (2000), the waxy cuticular layer of pine needles enhances their ability to trap lipophilic gaseous compounds and airborne particulate matter, reinforcing their role as sensitive and reliable bio-monitors. In addition to foliage, bark tissues from both broad-leaved and coniferous species have been used in studies of atmospheric contamination (Adeniyi, 1996; Grodzinka, 1982; Huhn et al., 1995; Lippo et al., 1995; Löstschert and Köhm, 1978). The advantage of using bark in biomonitoring is that its structure retains pollutants longer and it is highly porous (Świsłowski et al., 2020). Nonetheless, pine needles have a distinctive methodological advantage: their persistence on branches for periods exceeding one year allows for extended sampling intervals, thereby enabling the reconstruction of medium- to long-term trends in pollutant deposition and accumulation dynamics (Turkyilmaz et al., 2018).

3.3.1. Elemental concentrations

An overall overview of the element concentration results is shown in Table 3.13. Most of the elements analyzed, based on the Shapiro-Wilk test ($p < 0.05$), demonstrate asymmetrical distribution. The median concentrations of the macro elements ranged from 5910 μg g^{-1} (K) to 965 μg g^{-1} (P) with the following order of abundance: K>Ca>Mg>Na>P. A second group of elements followed this abundance order Fe>Al>Mn>Zn>Ti>Cu>Ba>Cr>Ni>Pb>Mo>V>As, with median concentrations ranging from 158500 ng g^{-1} to 140 ng g^{-1}. The remaining elements, such as Sb, Co, Se, Cd showed concentrations below 100 ng g^{-1}. Among the detected elements, some belong to macronutrients (such as Ca, Mg, K, P) and micronutrients (such as Fe, Mn, Zn, Cu), which play a crucial role in plant metabolic processes (Hepler, 2005; Kandziora-Ciupa et al., 2016; Marschner and Marschner, 2012; Soetan et al., 2010; Wang et al., 2013). The distribution data show considerable variability, with

positive skewness and kurtosis values for all elements, except for Mg kurtosis value. Notably, several trace elements, such as As, Cd, Co, Cr, Mn, Ni, Pb, and Sb, display high kurtosis values above 10, indicative of leptokurtic distributions characterized by a sharper peak and heavier tails. Other elements exhibit platykurtic distributions, reflecting flatter peaks and lighter tails. The calculated robust coefficient of variation (rCV%) reveals different value ranges: from 0.7% to 20% for elements such as Ba, Co, Cu, K, Ni, P, Se, and Zn; from 20% to 30% for Al, As, Ca, Cd, Cr, Fe, Mg, Mn, Pb, Sb, Ti, and V; and above 30% for Mo and Na (Ambrosino et al., 2023). These data reveal potential differences in environmental availability or plant uptake, highlighting significant heterogeneity among sampled sites. Overall, the statistical analysis indicates that, alongside a natural geochemical background, anthropogenic influences may also be present.

Table 3.13 - Descriptive statistics of major element concentrations in water samples. MAD: Median Absolute Deviation, rCV%: robust Coefficient of Variation, Q: Quartile, P: Percentile. Major elements expressed in $\mu g\ g^{-1}$ and trace elements in $ng\ g^{-1}$.

		AVERAGE	*MEDIAN*	*MINIMUM*	*MAXIMUM*	*MAD*	*rCV%*	*KURTOSIS*	*SKEWNEES*	*Q_1*	*Q_3*	*P10*	*P90*
Major elements	Ca	4466	4280	1090	10600	980	22	1.8	0.8	3510	5440	2296	6784
	K	6881	5910	3510	17800	1305	19	3.5	1.8	4655	7520	4382	11500
	Mg	2885	2870	1220	5000	630	22	-0.1	0.1	2340	3530	2030	3808
	Na	4284	2700	175	16500	1425	33	2.3	1.6	1520	5760	1194	8784
	P	1156	965	530	3220	226	20	5.2	2.2	789	1310	717	1740
Trace elements	Al	155652	138500	72000	336000	44500	29	0.1	0.8	110750	208000	83600	234900
	As	213	140	50	1760	55	26	22	4.4	95	195	69	341
	Ba	3042	2500	1000	10500	600	20	7.3	2.5	2000	3475	1680	4360
	Cd	60	39	7	463	15	25	17	3.8	23	52	16	138
	Co	130	88	49	846	19.5	15	18	4.1	73	129	65	178
	Cr	962	800	500	5300	200	21	26	4.8	600	1025	500	1210
	Cu	2922	2610	1880	7510	335	12	7.6	2.6	2325	2985	2063	4041
	Fe	181820	158500	85000	557000	43.5	24	6.7	2.2	118750	216750	104600	284836
	Mn	37525	19350	5600	295000	8050	21	15	3.9	15650	41450	10857	47970
	Mo	458	370	60	1350	140	31	1.9	1.4	238	628	159	767
	Ni	857	630	360	4790	140	16	19	3.9	500	773	407	1497
	Pb	635	440	240	5520	135	21	32	5.5	320	647	279	842
	Sb	113	90	50	660	30	26	27	4.8	70	127	60	180
	Se	95	65	65	300	0	0	3.2	2.0	65	100	65	200
	Ti	4264	3450	1640	13210	1080	25	5.0	2.1	2570	5050	2248	6819
	V	291	250	110	1053	60	21	9.4	2.9	188	310	160	425
	Zn	18966	16550	9100	42200	3450	18	1.0	1.3	13850	22350	11160	31630

Figure 3.27 shows the box plot for all determined elements, highlighting the variability of the distributions. These patterns likely result from heterogeneous environmental inputs, variable soil availability, or localized atmospheric deposition processes. These results emphasize the importance of combining analytical data with contextual information on environmental, geological, and landsoil characteristics to ensure accurate interpretation of observed concentrations (Lehndorff and Schwark, 2010; Serbula et al., 2013).

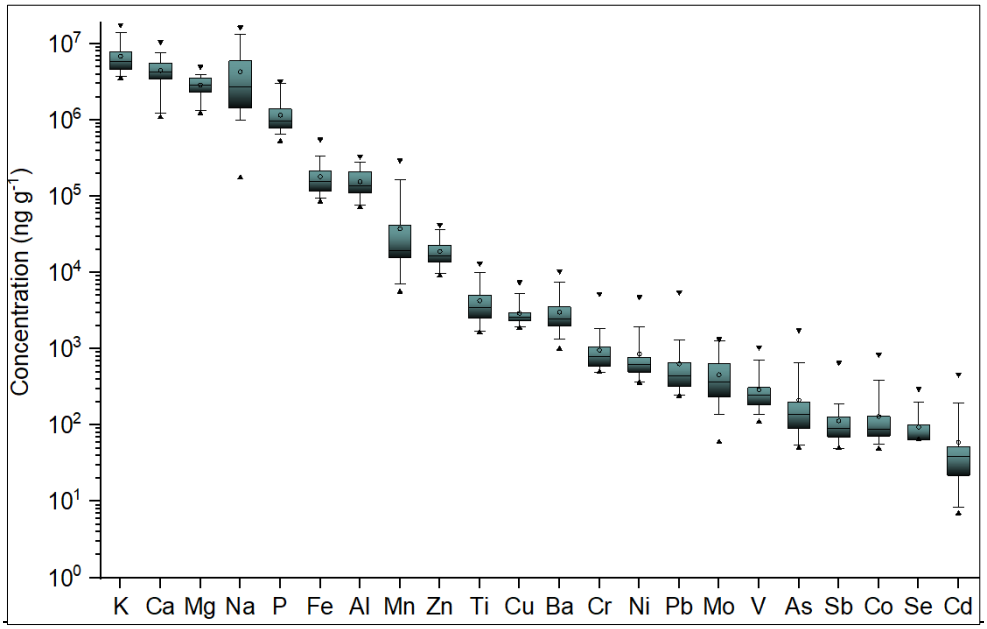

Figure 3.27 – Boxplots for each element distribution. Boxes delineate the interquartile range (25–75 %) with an indication of the median (solid line) and mean value (small circle inside the box). Whiskers indicate a 10–90 % range. The triangle symbols indicate the minimum and maximum values. Data are expressed in ng g^{-1}.

While sampling pine needles, it was possible to collect bark and soil samples simultaneously, resulting in 9 complete sample sets. Figure 3.28 shows the median concentrations of various chemical elements in pine needles, bark, and surface soil, revealing clear differences among the three matrices. An initial analysis reveals a similar pattern in element concentrations across the three: needles and bark tend to follow nearly parallel trends and often have similar values, whereas topsoils generally exhibit significantly higher concentrations. However, a closer look uncovers notable differences. For elements with mainly lithogenic origins, such as Al, Fe, and Ti, soil stands out distinctly, with concentrations much higher than those in needles and bark, which remain low and similar. Conversely, more mobile or biologically active elements, such as Mn, Zn, and Cu, display relatively high concentrations even in plant samples (needles and bark) (Huang et al., 2024; Kandziora-Ciupa et al., 2016; Kosiorek et al., 2016; Marschner and Marschner, 2012). In cases where no significant differences between soil and plants are observed, these similarities could be due to both natural factors (such as Cu, Mn, and Zn) and human activities (e.g., Cd, Pb, and Sb). This pattern reflects the combined effect of two processes: (i) bioaccumulation through root uptake and (ii) atmospheric deposition that gathers on the surfaces of needles and bark. Therefore, the variability from one site to another cannot be attributed solely to local geology, but is also greatly influenced by human pollution sources.

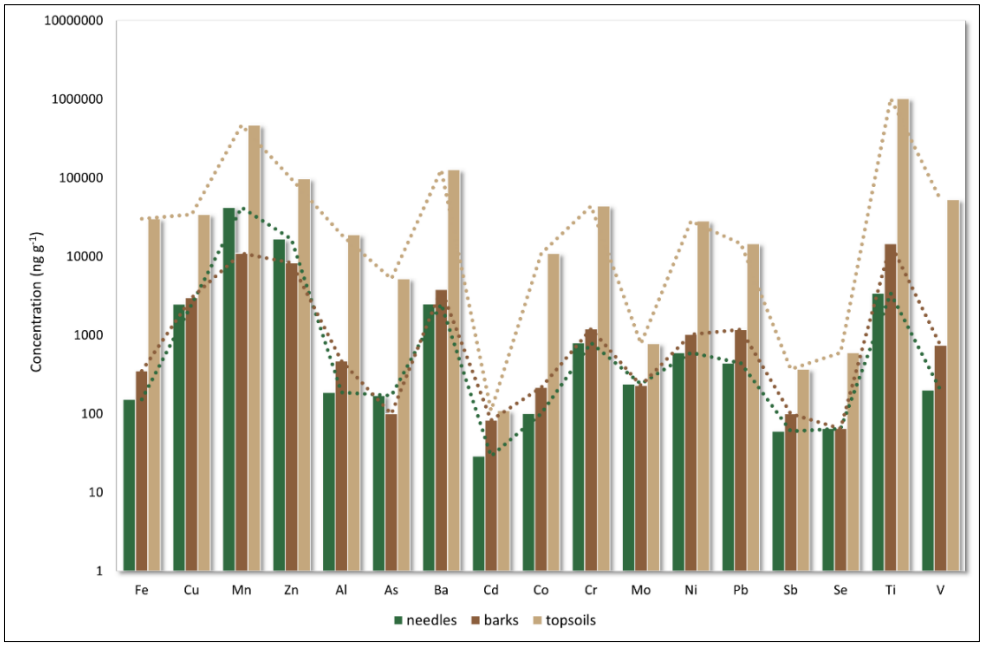

Figure 3.28 - Pattern of concentrations in pine needle-bark-topsoil sets. Data in ng g^{-1}.

REE are widely applied in environmental studies; they may be used as markers to trace the atmospheric deposition of particulate matter (Chiarenzelli et al., 2001; Dongarra and Varrica, 1998; Varrica et al., 2003; Varrica and Alaimo, 2024). The most abundant lanthanide is Ce (Tab.3.14), with a median concentration of 143 ng g^{-1}; the other elements follow this order of abundance, with the lowest value being 0.60 ng g^{-1} (Tm = Lu):

Ce>La>Nd>Y>Pr>Sm>Gd>Dy>Er=Yb>Eu>Ho>Tb>Tm=Lu.

Table 3.14- Average and median REE concentrations in pine needle samples. Data in ng g^{-1}.

	Rare earth elements (ng g^{-1})														
	Y	*La*	*Ce*	*Pr*	*Nd*	*Sm*	*Eu*	*Gd*	*Tb*	*Dy*	*Ho*	*Er*	*Tm*	*Yb*	*Lu*
AVERAGE	46	112	163	24	101	19	4	16	2	12	2	5	1	5	1
MEDIAN	43	90	143	21	88	17	3	14	2	11	2	5	1	5	1

Assessing the variation and relative distributions of REE abundance (i.e., fractionation) requires normalization to the chondritic values proposed by Anders and Ebihara, (1982). For pine needles, dividing REEs into light (LREEs), medium (MREEs) and heavy (HREEs) categories (Chen et al., 2015; Dubinin, 2004; Migaszewski and Gałuszka, 2019) offers additional insight into their biogeochemical behavior (Tab.3.15).

Table 3.15 - Average and median values of total, light (LREE), medium (MREE), heavy (HREE) Rare Earth Element (REE) concentrations and the LREE/HREE ratio. Data in ng g^{-1}.

	∑REE	*∑LREE*	*∑MREE*	*∑HREE*	*∑LREE/∑HREE*
Average	1.74	1.22	0.37	0.11	11.39
Median	1.55	1.05	0.34	0.09	11.08

The results show a strong enrichment of LREEs in pine needles, with much lower levels of MREEs and especially HREEs. This is reflected in a median ΣLREE/ΣHREE ratio of 11.08, emphasizing a clear preference for LREE accumulation. Such fractionation patterns match those observed in other biological and environmental systems (Brioschi et al., 2013), where plants often take up more LREEs than HREEs. This pattern is linked to differences in ionic forms: plants tend to absorb REEs that exist as free LREE ions, while many HREEs mainly appear as complexed ions (Brioschi et al., 2013). Figure 3.29 compares normalized REE concentrations in pine needles, bark, and related soil.

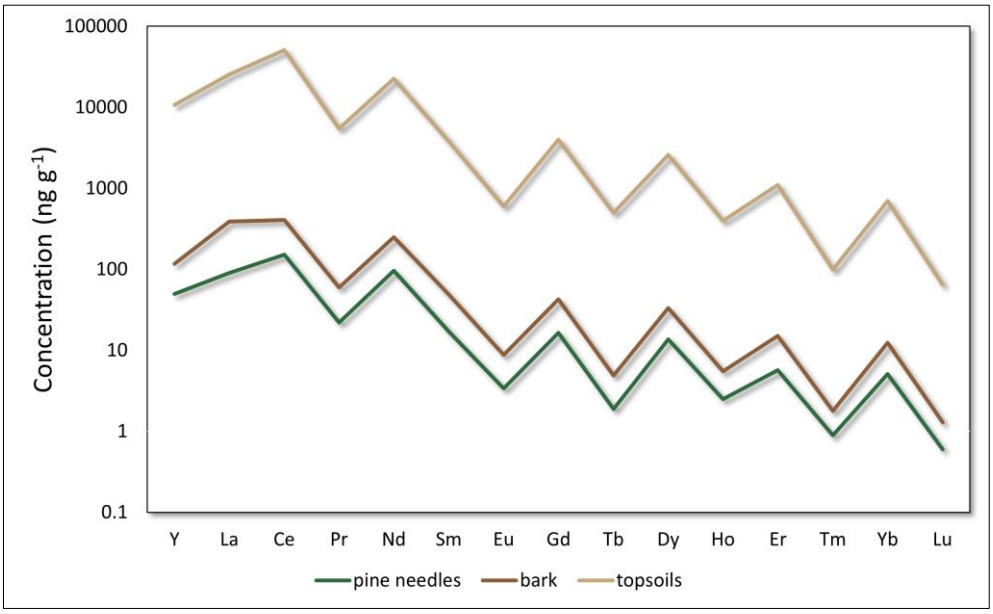

Figure 3.29 - Comparison of Rare Earth Elements in pine needle, bark, and soil samples. Data in ng g^{-1}.

The distribution patterns across these three matrices are almost identical, indicating minimal change in the relative REE proportions during plant uptake. This strong correlation suggests that plants largely maintain the geochemical signature of their substrate, supporting the use of REE as reliable tracers for differentiating between natural and human-made inputs.

3.3.2. Compositional Data analysis (CoDa), Compositional Pollution Index (CPI), and Multivariate spatial statistics – stochastic approach

The CoDa geostatistical method was initially used to identify anomalies within the dataset by employing the atypicality index, which flagged sample PN31 as a potential outlier. Since this was a single data point with no immediate reason for removal, it was kept during the preliminary phase. Based on prior knowledge of the study area, the samples were later grouped into two macro-categories: potentially anthropogenic and potentially natural, using multiple criteria, including anthropogenic influence, geographic and topographic context, and legislative designation (Siti di interesse Nazionale, SIN). The initial clr-biplot (Fig. 3.30) showed that the first three principal components (PC1, PC2, PC3) accounted for 76% of the total variability.

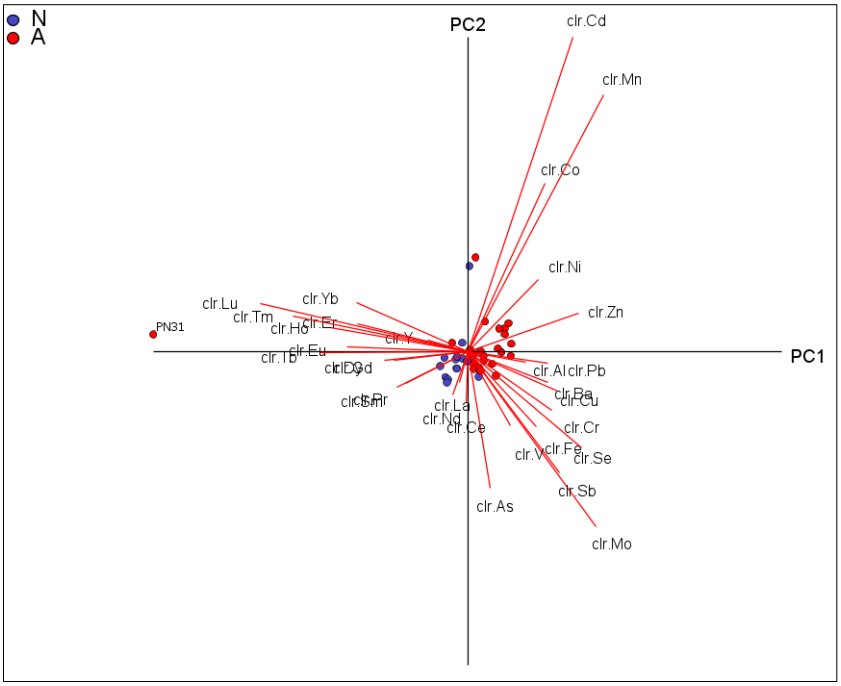

Figure 3.30– clr-biplot of all pine needle samples. Samples classified as natural are in blue, while those classified as anthropogenic are in red.

The PN31 sample exhibited a significant deviation from the other samples along PC1, which dominated the variance and made it difficult to visualize differences between groups. Its identification as an outlier, both statistically (via atypicality tests) and visually (biplot isolation), strongly supports its classification as a genuine multivariate outlier, unrelated to natural or anthropogenic patterns. To prevent bias during the exploratory phase, PN31 was excluded, and a new clr-biplot was created (Fig. 3.31).

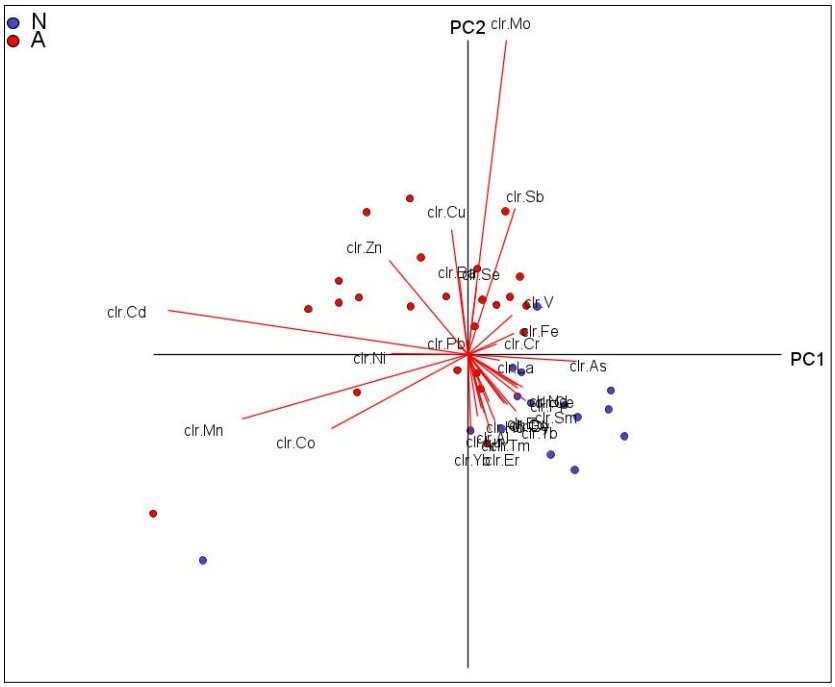

Figure 3.31 – clr-biplot of pine needle samples without the PN31 sample. Samples classified as natural are in blue, while those classified as anthropogenic are in red.

The first three components accounted for 64% of the total variability, clearly distinguishing anthropogenic samples, which are clustered in the northwestern quadrant, from natural samples, grouped in the southeastern quadrant. Anthropogenic sites were characterized by elements such as Ba, Cd, Cu, Mo, Sb, Se, and Zn, whereas the natural group was dominated by REE and As. Elements such as Al, Fe, V, Cr, Mn, and Co were more diffusely distributed, marking transitional zones and showing lower discriminating power between site categories. Based on these distinguishing elements, the Compositional Pollution Index (CPI) was constructed following expert-based selection criteria (Boente et al. 2022). CPI values, ranging from 4.74 to 8.56, were positive across all samples, indicating that the entire area exhibits chemical alteration to varying degrees, from natural background enrichment to anthropogenic contamination. Spatial modelling of the CPI involved calculating the experimental isotropic variogram and performing 100 sequential Gaussian simulations (SGS) to predict the CPI distribution (Fig. 3.32). The resulting maps revealed clear spatial variability and clusters of contamination hotspots. Classification of CPI values using the Jenks Natural Breaks classification (Jenks 1967), which optimizes within-class homogeneity and between-class separation. Computations were performed using Space-Stat v.4.0.18 (BioMedware) software (Boente et al. 2022; Albuquerque et al. 2017).

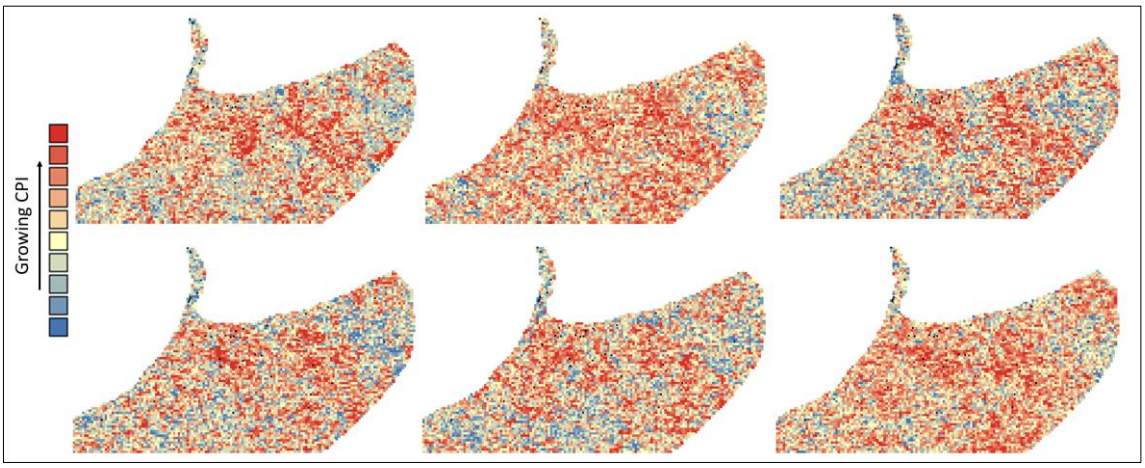

Figure 3.32 - Six different scenarios obtained by sequential Gaussian simulation (SGS) of CPI values.

All simulation outputs, including those for the biological matrix, consistently identified the SIN-designed area as highly contaminated. The mean image (MI) and the standard deviation (0.36 to 0.88) across simulations are shown in Figure 3.33.

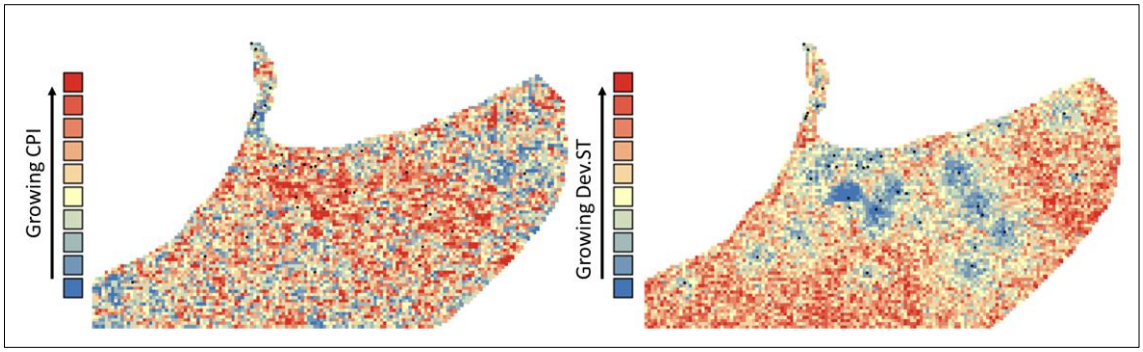

Figure 3.33 - left: Average of 100 Sequential Gaussian Simulation (SGS) of CPI values; right: standard deviation of CPI values.

Probability maps of exceeding the third quartile (Q3) and staying below the first quartile (Q1) (Fig. 3.34) clearly show contamination risk clusters. Dark green areas on the Q3-exceedance probability map indicate intense anthropogenic pressure, consistent with the SIN classification, while dark green areas on the Q1-non-exceedance map mark zones of minimal human impact, supporting their classification as natural.

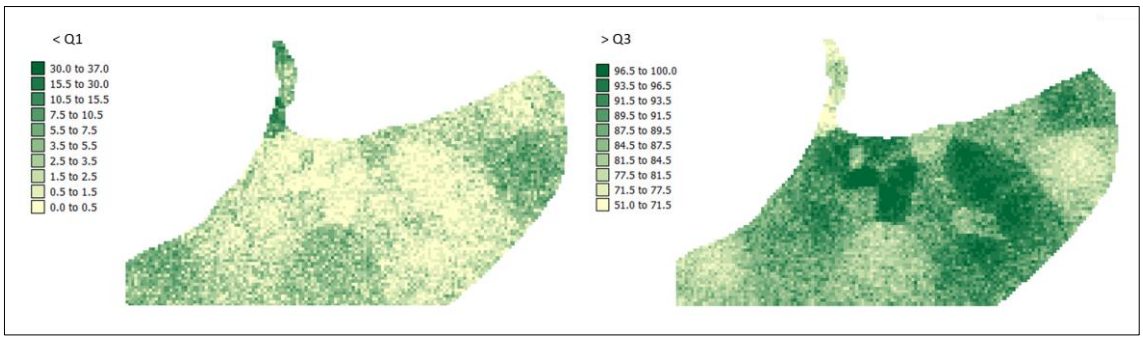

Figure 3.34 - Maps of the probability of not exceeding Q_1 and exceeding Q_3 of CPI values.

To further evaluate spatial clustering, the Local G test was used (Fig. 3.35). Results closely matched the CPI probability maps, identifying the main contamination zones in the SIN area and highlighting Capo Milazzo, western sector, and the hinterland on the eastern side as natural areas. This combined analysis provides a robust foundation for understanding how contamination is spatially distributed and for distinguishing natural geochemical background from human-related sources.

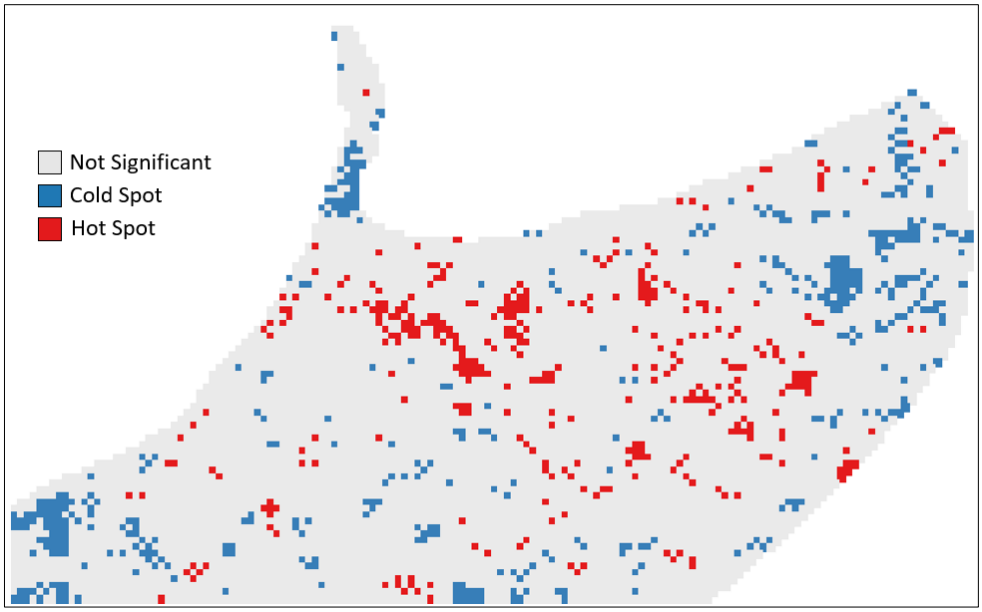

Figure 3.35 - Map of spatial clusters calculated with the Local G test. The red areas indicate hot spots (significantly high values surrounded by high values), while the blue areas represent cold spots (significantly low values surrounded by low values). Neutral values (gray) indicate the absence of significant spatial autocorrelation. The test considers the local spatial structure to identify statistically significant aggregations.

3.4. Lead isotopic data

Lead and its compounds have been widely used since ancient times, with their presence in the environment increasing significantly after industrialization (Abbaszade et al., 2022; Komárek et al., 2008; Riva et al., 2012). Natural sources of Pb include rock weathering, volcanic eruptions, and forest fires, which release lead into environmental compartments where it becomes part of the biogeochemical cycle (Shotyk et al., 1998). In contrast, human activities are the main source of Pb contamination. Currently, major anthropogenic sources include industrial processes, mining, battery production and recycling, pigments, ceramics, plastics, fossil fuel combustion, mineral fertilizers, and sewage sludge application (Adriano, 2001; Ahlberg et al., 2006; Hopper et al., 1991; Komárek et al., 2008; Mihaljevič, 1999; Rieuwerts et al., 1999; Sturges and Barrie, 1987). Global emission inventories estimate that human-made Pb fluxes are one to two orders of magnitude higher than natural inputs (Komárek et al., 2008). Additionally, these activities introduce various chemical species of Pb, many of which remain persistent in the environment (Saint-Laurent et al., 2010). Once released, Pb particles can be transported over long distances before settling onto soils or water bodies, where they accumulate in sediments, plants, and animal tissues (Bollhöfer and Rosman, 2000). Many studies have thus examined Pb levels across environmental compartments. Understanding how Pb transforms and tracing its sources in land and water systems are essential for assessing environmental risks and promoting sustainable land management. In recent decades, Pb stable isotopes have become a powerful tool for distinguishing between natural (geogenic) and human-made (anthropogenic) sources. This approach depends on the presence of four stable isotopes: ^{204}Pb (1.4%, primordial), ^{206}Pb (24.1%, partially radiogenic, daughter of ^{238}U), ^{207}Pb (22.1%, partially radiogenic, daughter of ^{235}U), and ^{208}Pb (52.4%, partially radiogenic, daughter of ^{232}Th). Different source materials show distinct isotopic ratios, providing diagnostic “fingerprints” that can distinguish natural from anthropogenic Pb (Komárek et al., 2008; Liu et al., 2016; Reimann et al., 2016). Significantly, isotopic ratios are mostly unaffected by physicochemical fractionation processes, making Pb isotopes a dependable tracer of contamination sources (Bollhöfer and Rosman, 2000; Veysseyre et al., 2001). One goal of this study was to analyze the contribution of geogenic and anthropogenic inputs to air and soils using Pb isotope compositions in pine needles, water, and soils within a complex environmental setting where natural and human-made sources coexist. Table 3.16 presents lead isotope ratios measured from the collected samples. The pine needle samples ranged from 1.153 to 1.192 (average: 1.171) for ^{206}Pb/^{207}Pb and from 2.063 to 2.108 (average: 2.093) for ^{208}Pb/^{206}Pb. The water samples ranged from 1.154 to 1.206 (average: 1.174) for ^{206}Pb/^{207}Pb and from 2.036 to 2.118 (average: 2.087) for ^{208}Pb/^{206}Pb. The isotope ratios in the topsoil samples tend to overlap with the ranges observed in the other matrices, varying from 1.184 to 1.214 (average: 1.197) for ^{206}Pb/^{207}Pb

and from 2.070 to 2.098 (average: 2.082) for $^{208}Pb/^{206}Pb$. All groups of samples showed consistent lead isotopic compositions, with topsoil samples appearing more radiogenic than the others.

Table 3.16 – Lead isotopes ratios measured in pine needle, water and topsoil samples from Valle del Mela district.

	$^{206}Pb/^{207}Pb$	$^{208}Pb/^{206}Pb$		$^{206}Pb/^{207}Pb$	$^{208}Pb/^{206}Pb$
	Pine needles			*Waters*	
PN1	1.192	2.063	*PE1*	1.156	2.107
PN2	1.178	2.086	*PE3*	1.166	2.095
PN6	1.171	2.093	*PE8*	1.174	2.084
PN7	1.174	2.093	*PE14*	1.1770	2.079
PN8	1.170	2.096	*PE17*	1.173	2.094
PN9	1.163	2.099	*PE25*	1.178	2.088
PN11	1.168	2.095	*PE26*	1.169	2.092
PN13	1.171	2.095	*PE32*	1.171	2.097
PN15	1.181	2.082	*PE38*	1.167	2.118
PN16	1.169	2.097	*PE42*	1.164	2.102
PN18	1.171	2.093	*PE45*	1.165	2.092
PN20	1.169	2.094	*PE54*	1.164	2.111
PN22	1.166	2.099		*Topsoils*	
PN23	1.184	2.075			
PN24	1.153	2.108	*S5*	1.214	2.075
PN25	1.167	2.095	*S7*	1.201	2.070
PN26	1.162	2.102	*S8*	1.198	2.080
PN28	1.167	2.094	*S71*	1.187	2.098
PN31	1.166	2.098	*S72*	1.192	2.088
PN34	1.173	2.092	*S74*	1.193	2.084
PN36	1.171	2.094	*S27*	1.184	2.098
PN37	1.171	2.090	*S73*	1.163	2.101
PN38	1.177	2.089	*S38*	1.149	2.111
PN40	1.160	2.107			

Figure 3.36 shows the lead isotope data measured in pine needles, water, and topsoil on the conventional $^{206}Pb/^{207}Pb$ versus $^{208}Pb/^{206}Pb$ plot. To identify potential lead sources, isotopic signatures from both natural and anthropogenic origins were analyzed. Results from a previous study (Monna et al., 1999) demonstrated that two types of anthropogenic Pb can be identified in Sicily: Pb used as an anti-knock additive in gasoline and Pb employed by industry. The geogenic end-members were defined using topsoils and bottom soils from the Peloritani mountains (Cosenza et al., 2015), volcanic materials such as rocks from Vulcano and Stromboli Islands (De Astis et al., 2000; Métrich et al., 2001; Monna et al., 1999), volcanic ash (Schiavi et al., 2012), and Sicilian sedimentary rocks (Alaimo et al., 2000). The distribution of samples within the isotopic space highlights the complexity of lead sources in the study area. Notably, the samples plot far from the gasoline-related signature, indicating limited direct influence from this source overall. The data also show that the samples are not homogeneously distributed, but instead form three distinct clusters, each with a different isotopic

signature. The first group is close to industrial areas, showing a strong isotopic match with local emissions. These samples suggest direct and predominant contamination from industrial activities.

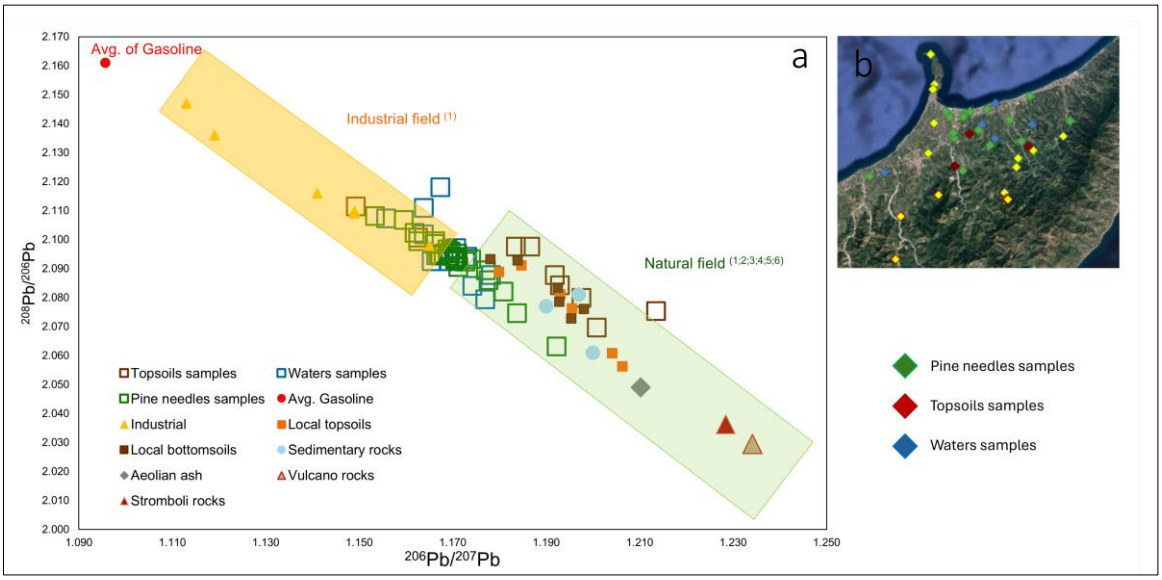

Figure 3.36 – a) Lead stable isotope ratios ($^{208}Pb/^{206}Pb$ vs. $^{206}Pb/^{207}Pb$) in water, topsoil, and pine needle samples, together with isotopic signatures of potential Pb sources. 1 (Monna et al., 1999), 2 (Cosenza et al., 2015), 3 (Alaimo et al., 2000), 4 (Schiavi et al., 2012); 5(De Astis et al., 2000); 6 (Métrich et al., 2001); b) Spatial distribution of the samples (waters, topsoils, and pine needles) subjected to isotopic analysis. Samples falling within the natural field are shown in yellow.

The second group, which includes most of the samples, forms a transition zone between anthropogenic and geogenic sources. Their intermediate isotopic values suggest mixing between dominant industrial inputs and the natural geological background. The third group is positioned entirely within the natural field. The spatial distribution of these natural-signature samples (Fig. 3.37b, highlighted in yellow) supports the isotopic evidence, as they are mainly located inland, at higher altitudes along the Peloritani ridge and the Milazzo peninsula, characterized by lower levels of urbanization and industrial activity. Consequently, their isotopic composition mirrors the underlying local geology, which is predominantly characterized by sedimentary and metamorphic lithologies. Furthermore, for the samples from the Milazzo peninsula, a volcanic contribution from the Aeolian Islands cannot be ruled out, as it is amplified by the prevailing wind regime in this area. In contrast, samples within the industrial influence zone are concentrated near coastal and lowland areas. The isotopic lead data highlight the variability among the samples, emphasizing that lead contamination is not evenly distributed within the same geographical area.

3.5.Definition and application of local geochemical baselines in water and topsoil

The consistency between the Local G map results across the three matrices analyzed and the Pb isotopic data strengthens the reliability of the interpretative model for source discrimination. The environmental geochemistry of an area is a complex mosaic shaped by both natural processes and human activities, and recognizing potential sources is essential to accurately assess the state of contamination. In this study, the multi-matrix approach improved the distinction between areas with stronger natural inputs and those with predominant anthropogenic inputs (Albanese et al., 2007b; Cicchella et al., 2005; Frattini et al., 2006; Galán et al., 2008; Matschullat et al., 2000; Salminen and Gregorauskiene, 2000). National and international reference values, which are defined exclusively for inorganic matrices such as water and soil, often fail to capture the environmental specificities of a given area. To address this limitation, site-specific geochemical baseline values were established in this study for both water and soil matrices, providing a more reliable framework for distinguishing natural geochemical variability from anthropogenic contamination. Therefore, considering the results of Local G for water and topsoil, the samples based on the domains identified as *cold spot* and *hot spot* were divided into two subdatasets, *natural* and *anthropogenic*. To statistically validate these domains, Sparse Linear Discriminant Analysis (sLDA) (Clemmensen et al., 2011; Liu et al., 2024; Qiao et al., 2009) was performed. The use of sLDA is advantageous for reducing the influence of noisy variables during the construction of the composite expression. In line with the compositional data approach adopted in this study, sLDA was applied to the isometric log-ratio (ilr)-transformed dataset. The ilr transformation was performed on the raw data using a sequential binary partition implemented in the CoDaPack software. The results of the sLDA analysis on water samples highlighted relevant ilr variables (ilr 4, ilr 1, ilr 10, ilr 5, ilr 17, ilr 9, ilr 14, and ilr12) in the first discriminant, i.e., the linear combination of variables that maximizes the separation between groups. These variables represent the main contributors to the discrimination of samples based on their group affiliation. The model was initially trained on the entire dataset with a lambda, i.e., the parameter that regularizes the model's sparsity, fixed at 0.2. The overall accuracy is 83.5%, an excellent value reflecting the model's strong ability to adapt to the dataset. A search for the best regularization parameter identified 0.05 as the optimal value for lambda. The final model was then trained on the entire dataset using this lambda value (0.05), again achieving 83.5% accuracy. This is the most significant and interesting aspect of the analysis, as the model's performance remains stable across a wide range of lambda values. This suggests that the initial value of 0.2 was already close to optimal for this dataset and indicates that the model is robust to variations in the regularization parameter. In the graph (Fig. 3.37), the two density curves (red for hot spot samples and blue for cold spot samples) are clearly separated, although they overlap slightly in the centre. The vertical dashed lines represent

the median scores for each group. Their distinct and distant positions confirm that the model has successfully identified the combination of variables that allows us to distinguish two groups of samples. The overlap area between the curves identifies the misclassified samples (blended samples). To interpret the contributions of elements to the separation between the samples group, the coefficients on the ilr balances were projected into the original element space using the partition definition matrix. The contribution of each element was calculated as the sum of the product of the coefficient and the element's weight in the balance across all balances. The resulting score shows both the strength and direction of each element's influence (Fig.3.37). Rare earth elements and aluminum characterize the group of samples located in cold spot areas, attributable to natural domains. In contrast, elements such as Cd, Ba, Se, Sb, Zn, and V characterize the group of samples in hot spot areas, corresponding to anthropogenic domains.

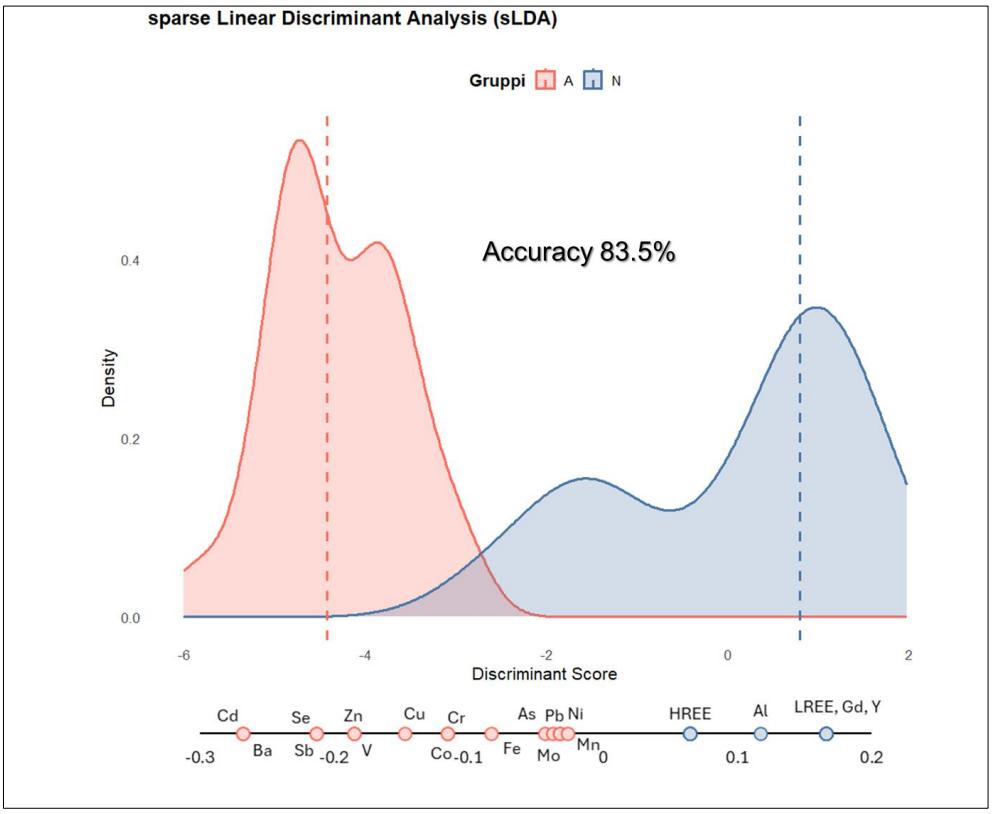

Figure 3.37 – Sparse Linear Discriminant Analysis (sLDA) applied on water samples. Group separation, efficiency of separation, and independent variables that best contributed to the separation. The dashed vertical lines indicate the median scores for each group. A: anthropogenic samples; N: natural samples.

The same technique was applied to topsoil samples, where sLDA analysis highlighted relevant ilr variables (ilr1, ilr12, ilr6, ilr10, ilr16, ilr17, ilr4, and ilr15) in the first discriminant. Regarding the water dataset, the sLDA model was run on the entire dataset using a fixed lambda value of 0.2. The overall accuracy was 79.7%. The search for the best lambda identified a value of 0.3, which, when applied to the model, resulted in an accuracy of 78.4%. In the graph (Fig. 3.38), the two density curves (red for hot spot samples and blue for cold spot samples) are clearly separated, although they overlap

in the centre. The median scores for each group, indicated by the dashed vertical lines, are distinct and far apart, confirming that the model successfully identified a combination of variables (the selected predictors) that separates samples in two groups. The contribution of each element was calculated, and the results are shown in Figure 3.38. Rare earth elements characterize the group of samples located in cold spot areas, attributable to natural domains. In contrast, elements such as V, Ba, Sb, Mo, Se, and Zn characterize the group of samples in hotspot areas, associated with anthropogenic domains.

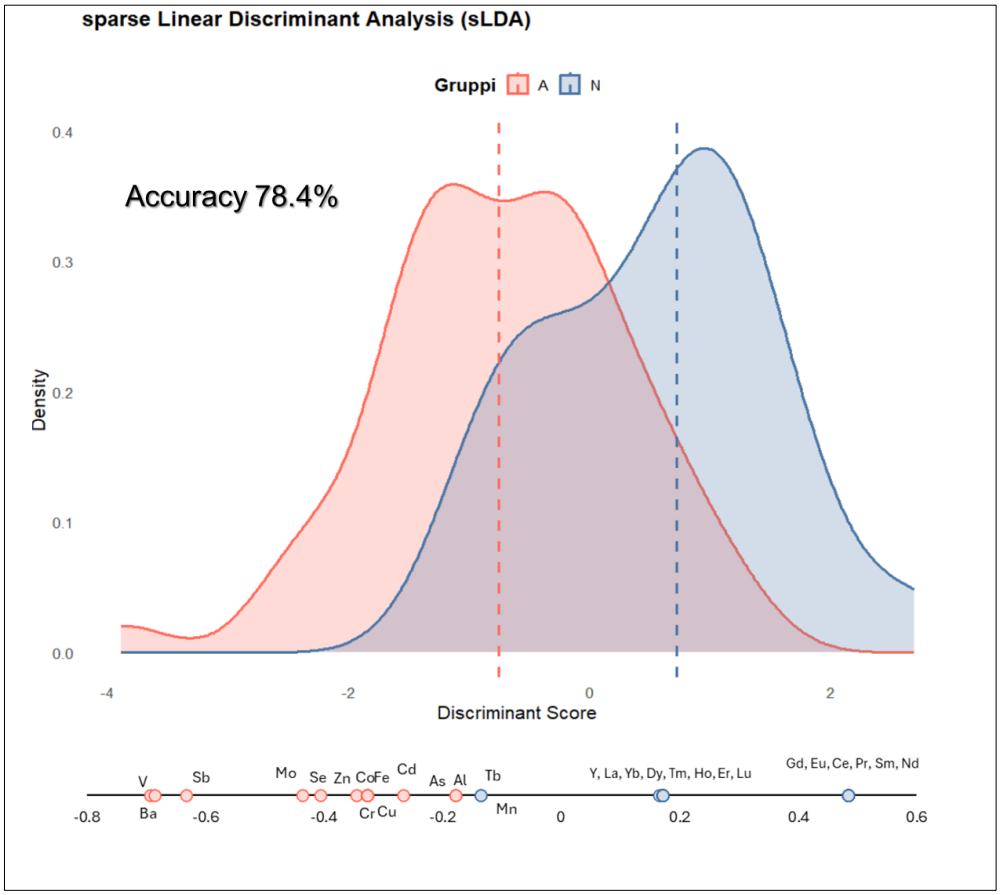

Figure 3.38 – Sparse Linear Discriminant Analysis (sLDA) applied on topsoil samples. Group separation, efficiency of separation, and independent variables that best contributed to the separation. The dashed vertical lines indicate the median scores for each group. A: anthropogenic samples; N: natural samples.

To obtain a more reliable estimate of model performance on held-out data, a 10-fold cross-validation was repeated five times for both the water and soil datasets. The sLDA model demonstrated a reasonable ability to distinguish between the two groups in the held-out data for both water and soil. Therefore, local G tests and sLDA analyses statistically robustly confirmed the distinction between anthropogenic and natural domains, providing a solid basis for defining geochemical baseline values in the water and topsoil environmental matrices. The superimposition of Local G test maps from surface water and soil samples was carried out, as shown in Figure 3.39. Several domains emerge from overlap of the two local G test maps (Fig.3.39): 1) both topsoils and waters show a natural area

(blue-blue); 2) both topsoils and waters show an anthropogenic area (red-red); 3) both topsoils and waters show an area where no significant clusters are detected (not-significant-not significant); 4) topsoils show a natural area but waters do not (blue-red); 5) topsoils show an anthropogenic area but waters do not (red-blue); 6) topsoils show a cluster (blue or red) but waters show no significant clusters, and vice versa. The domains where a perfect match in the results between water and surface soils is found include the SIN area and the coastal strip (hot spot), and the western sector of the hinterland up to the Peloritani ridge (cold spot).

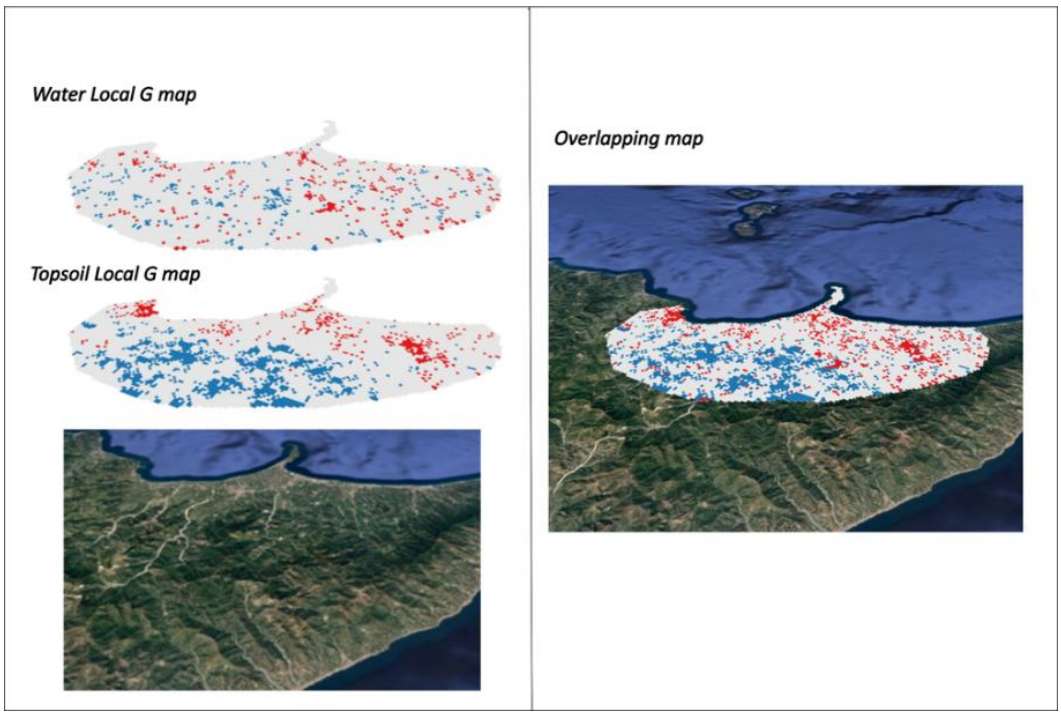

Figure 3.39 - Overlap between local G test maps performed on the spatial distribution of CPI values for water and topsoil samples.

To evaluate the spatial consistency between the geochemical domains identified in water and topsoil matrices, an overlap analysis of the respective maps was performed using the R programming environment, with shapefiles generated by the Local G test run on SpaceStat software. Concordance between the two maps was assessed at the individual simulation point level through an inner join of the water and topsoil data frames based on a unique row identifier. The results indicate significant agreement between the two matrices. Out of 7483 observations, 5701 points (approximately 77%) exhibit a matching classification between waters and topsoils. The overlap of these matrices is highly significant.

These findings justify the subsequent selection of concordance areas between anthropogenic and natural domains, which allow us to identify samples for defining geochemical baseline values in water and topsoil. The remaining 33% of the areas lack a correspondence between the matrices, indicating the coexistence of natural and anthropogenic mixing processes. Samples in these zones, referred to as blended samples, are excluded from the geochemical baseline calculation.

The results identified 26 water samples falling within the natural domain and 27 within the anthropogenic domain. For the topsoil samples, 21 were classified within the natural domain and 28 within the anthropogenic domain. These samples were used to calculate the natural and anthropic baseline values using the BCA- bootstrap (Bias- Corrected and Accelerated Bootstrap) technique. To ensure robustness and methodological consistency with the literature (Efron and Narasimhan, 2020), the procedure, performed on the ProUCL software, involved 2000 bootstrap runs, ensuring high stability of the estimates and reducing variability associated with random sampling. This setup enabled us to obtain a statistically robust and reliable estimate of the geochemical baseline values. To test the stability of the results, the process was repeated in the R environment, varying the number of bootstraps (500, 1.000, 5.000, and 10.000 replicates). It was observed that the UTL 95- 95 values remained practically unchanged starting from 1.000 bootstraps, indicating the estimate's stability concerning the number of bootstraps.

Table 3. 17 reports the Natural Baseline (NB) and Anthropic Baseline (AB) values calculated in water and topsoil matrices. These values reflect, for both waters and topsoils, the main sources of trace elements in the area. Specifically, elements such as Al, As, Mn, Sb in water samples and Al, As, Mn, Pb, Sb, and Zn in topsoils exhibit higher concentrations within the natural baseline, reflecting the main mineralogical assemblages present in the study area (Baldanza, 1949; De Vivo et al., 1999; Duplay et al., 2014; Mey, 2013; Triolo et al., 2008). Conversely, elements such as Ba, Cr, Cu, Mo, Se, V, and Zn in waters, and Ba, Cu, Mo, Ni, and V in topsoils, exhibit higher concentrations within the anthropic baseline values, indicating human activity inputs (Brugnone et al., 2025). The agreement between the matrices enhances the robustness of the interpretation in identifying the sources of the element.

Table 3.17– Natural Baseline (NB) and Anthropic Baseline (AB) calculated by the BCA-Bootstrap approach on the study area waters and topsoils samples. Data expressed in μg L^{-1} for water and μg g^{-1} for topsoil, respectively.

		Al	*As*	*Ba*	*Cd*	*Co*	*Cr*	*Cu*	*Fe*	*Mn*	*Mo*	*Ni*	*Pb*	*Sb*	*Se*	*V*	*Zn*
Geochemical baseline values in waters	NB	58.0	6.21	84.6	0.24	0.35	0.37	3.30	80.0	40.5	1.30	19.4	1.14	4.88	2.02	2.38	23.1
	AB	17.0	1.46	164	0.27	0.10	1.69	75.0	90.0	9.40	10.2	18.7	1.78	0.32	6.30	5.20	2010
Geochemical baseline values intopsoils	NB	53900	112	193	0.64	26.6	83.0	98.7	49800	1270	1.28	47.6	219	5.36	1.20	85.0	1120
	AB	33500	15.7	418	0.37	19.9	82.0	122	47300	1110	3.43	76.8	115	4.04	0.90	146	309

The determination of local geochemical baseline values is a key tool for evaluating environmental quality, establishing standards and guidelines for legislation, and supporting land management decisions (Chen et al., 1999; Facchinelli et al., 2001; Sappa et al., 2020; Wei and Wen, 2012).

Defining a local geochemical baseline value is crucial because it reflects the site-specific characteristics of an area, resulting from both geogenic and anthropogenic sources. Tables 3.18 and

3.19 report the Natural Baseline (NB) and Anthropic Baseline (AB) values of waters and topsoils with national limits (D. Lgs 23/23, 2023; D.Lgs 152/06, 2006).

The comparison clearly shows that, for waters, local values are lower than the established limits (Tab. 3.18). This highlights how using generic thresholds, not tailored to the local context, can lead to underestimating or overestimating contamination, since even significantly elevated local values often stay within official limits.

Table 3.18 – Comparison of water geochemical baseline (NB and AB) with the Italian legislation limits (D. Lgs 152/2006, D. Lgs. 23/23). Data expressed in μg L^{-1}.

	Al	*As*	*Ba*	*Cd*	*Co*	*Cr*	*Cu*	*Fe*	*Mn*	*Mo*	*Ni*	*Pb*	*Sb*	*Se*	*V*	*Zn*
NB	58.0	6.21	84.6	0.24	0.35	0.37	3.30	80.0	40.5	1.30	19.4	1.14	4.88	2.02	2.38	23.1
AB	17.0	1.46	164	0.27	0.10	1.69	75.0	90.0	9.40	10.2	18.7	1.78	0.32	6.30	5.20	2010
D. Lgs. 152/06	200	10		5	50	50	1000	200	50		20	10	5	10		3000
D. Lgs 23/23	200	10		5		25	2000	200	50		20	5	10		140	

In topsoils, the comparison shows exceedances of the limit thresholds: regarding the natural baseline for As, the anthropic baseline for Cu and V, and both baselines for Co, Pb, and Zn (Tab. 3.19).

Table 3.19 - Comparison of topsoil geochemical baseline (NB and AB) with the Regional Geochemical Baseline values (RGB) (Varrica et al., 2024; Lo Medico et al., 2025) and the Italian legislation limits (D. Lgs 152/2006, column A). Data expressed in μg g^{-1}.

	Al	*As*	*Ba*	*Cd*	*Co*	*Cr*	*Cu*	*Fe*	*Mn*	*Mo*	*Ni*	*Pb*	*Sb*	*Se*	*V*	*Zn*
NB	53900	112	193	0.64	26.6	83.0	98.7	49800	1270	1.28	47.6	219	5.36	1.20	85.0	1120
AB	33500	15.7	418	0.37	19.9	82.0	122	47300	1110	3.43	76.8	115	4.04	0.90	146	309
D. Lgs. 152/06		20		2	20	150	120				120	100	10	3	90	150
RGB	41414	11.8	245.9	1.16	22	58.1	62.9	52007	1303	3.96	44.89	41.3	1.14	1	88.2	124

These exceedances indicate the unique features of the study area and are linked to both geogenic and anthropogenic sources (Baldanza, 1949; De Vivo et al., 1999; Dinelli et al., 2012; Duplay et al., 2014; Mey, 2013; Triolo et al., 2008).

The comparison between the calculated local geochemical baseline values (both natural and anthropic) and the regional baseline values (RGB), as reported by Varrica et al. (2024) and Lo Medico et al. (2025) for uncontaminated topsoils in Sicily, reveals three types of deviations: significant deviations (>100%) for elements such as As, Pb, Sb, and Zn, across both natural and anthropic baselines (except As in the natural baseline); consistent deviations (>30%) for Cd, Cr, Cu, and Mo in the natural baseline, and for As, Ba, Cd, Cr, Cu, Ni, and V in the anthropic baseline; and minimal deviations (<30%) for Al, Ba, Co, Fe, Mn, Ni, Se, and V in the natural baseline, and for Al, Co, Fe, Mn, Mo, and Se in the anthropic baseline.

The observed deviations reflect both the unique local geochemistry, related to metamorphic rocks and polymetallic mineralizations, and the anthropogenic pressures in the Milazzo area. Using local baseline values is essential for capturing true natural variability, distinguishing anthropogenic increases, and accurately assessing environmental quality risks.

After establishing the natural and anthropic baselines for the waters and topsoil matrices, a key part of the study involved mapping the spatial distribution of elemental concentrations (Figs. 3.40-3.43). These maps show the spatial variability of the analyzed elements, highlighting areas of high concentrations mainly near coastal areas, the Site of National Interest for Reclamation (SIN), and along the Peloritani crest, indicating possible local sources of enrichment.

Consequently, the maps display a spatial gradient that links the previously identified geochemical domains with the distribution of concentrations, confirming the validity of the methodology used and enabling the identification of areas that represent environmental conditions, including hotspots of natural or anthropogenic enrichment.

The spatial distribution of elemental concentrations in water and topsoil samples, along with the definition of baseline values (AB and NB), provides a robust framework for classifying blended samples. For these samples, there is no clear distinction between natural or anthropogenic origins; instead, their categorization is element-dependent. Specifically, water samples for elements such as Al, Co, and Sb are closer to the anthropic baseline, while those for elements such as Ba, Cr, Mo, Se, V, and Zn are nearer to a natural baseline. Topsoil samples behave similarly, showing consistency with the anthropic baseline for elements such as As, Pb, Sb, Se, and Zn, and with the natural baseline for elements like Ba, Cu, Mo, Ni, and V. These results emphasize the importance of a multi-matrix approach, showing that these areas are not just a “mixing zones”, but instead reflect specific geochemical processes(Briffa et al., 2020; Cabral Pinto et al., 2017; Correia and Rasteiro, 2025; De Souza et al., 2017; Fernandes et al., 2018; Gorelick et al., 1993; Li et al., 2022; McLean and Bledsoe, 1992; Mikkonen et al., 2017; Qu et al., 2020; Violante et al., 2010; Xu et al., 2022; Zhang et al., 2019).

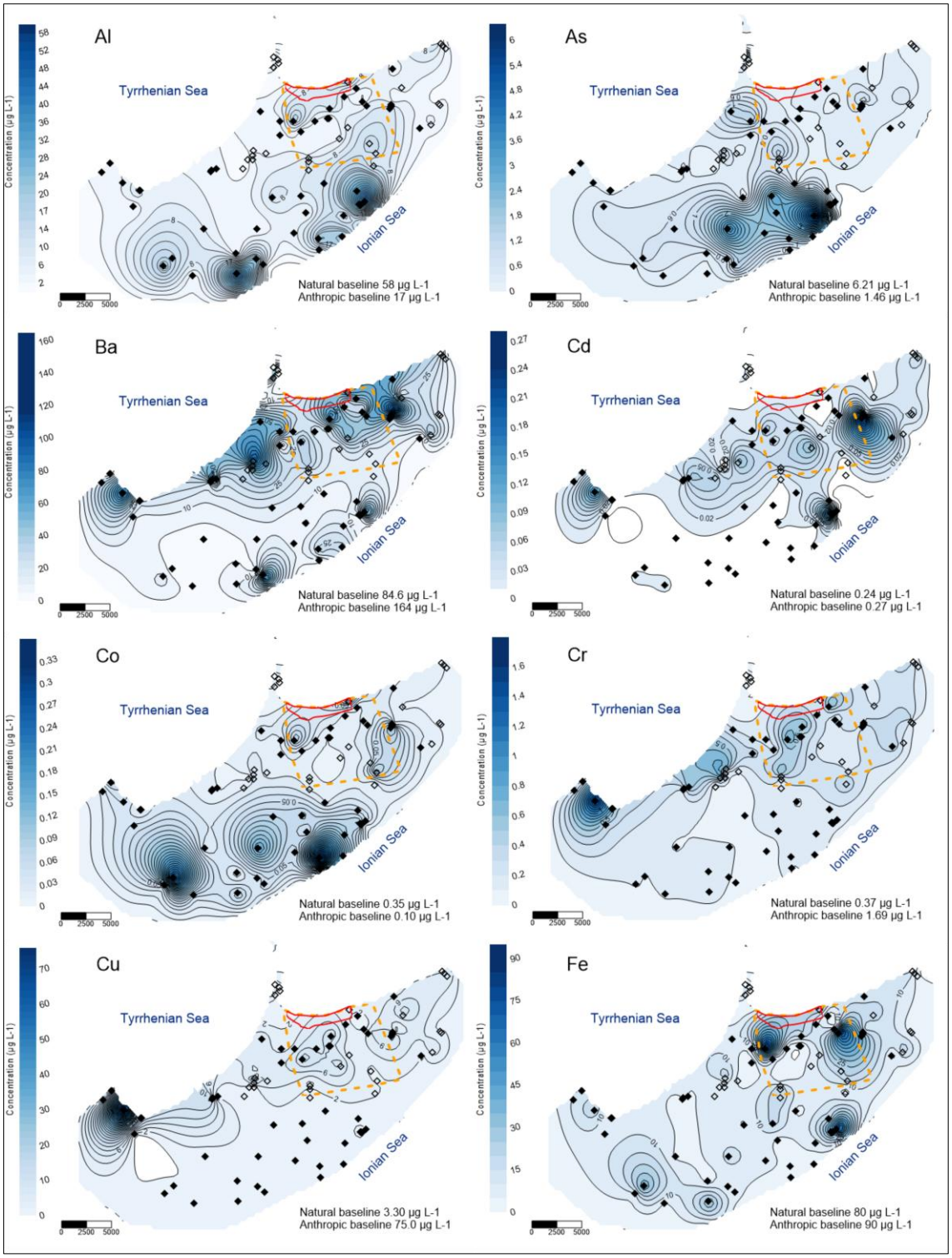

Figure 3.40 – Spatial distribution of Al, As, Ba, Cd, Co, Cr, Cu, and Fe in water samples. The filled rhombuses represent the pure samples used to calculate the natural and anthropic geochemical baseline values. The empty rhombuses represent the blended samples excluded from the calculation. The industrial plant is marked in red, and the boundary of the Site of National Interest for remediation (SIN) is outlined in orange.

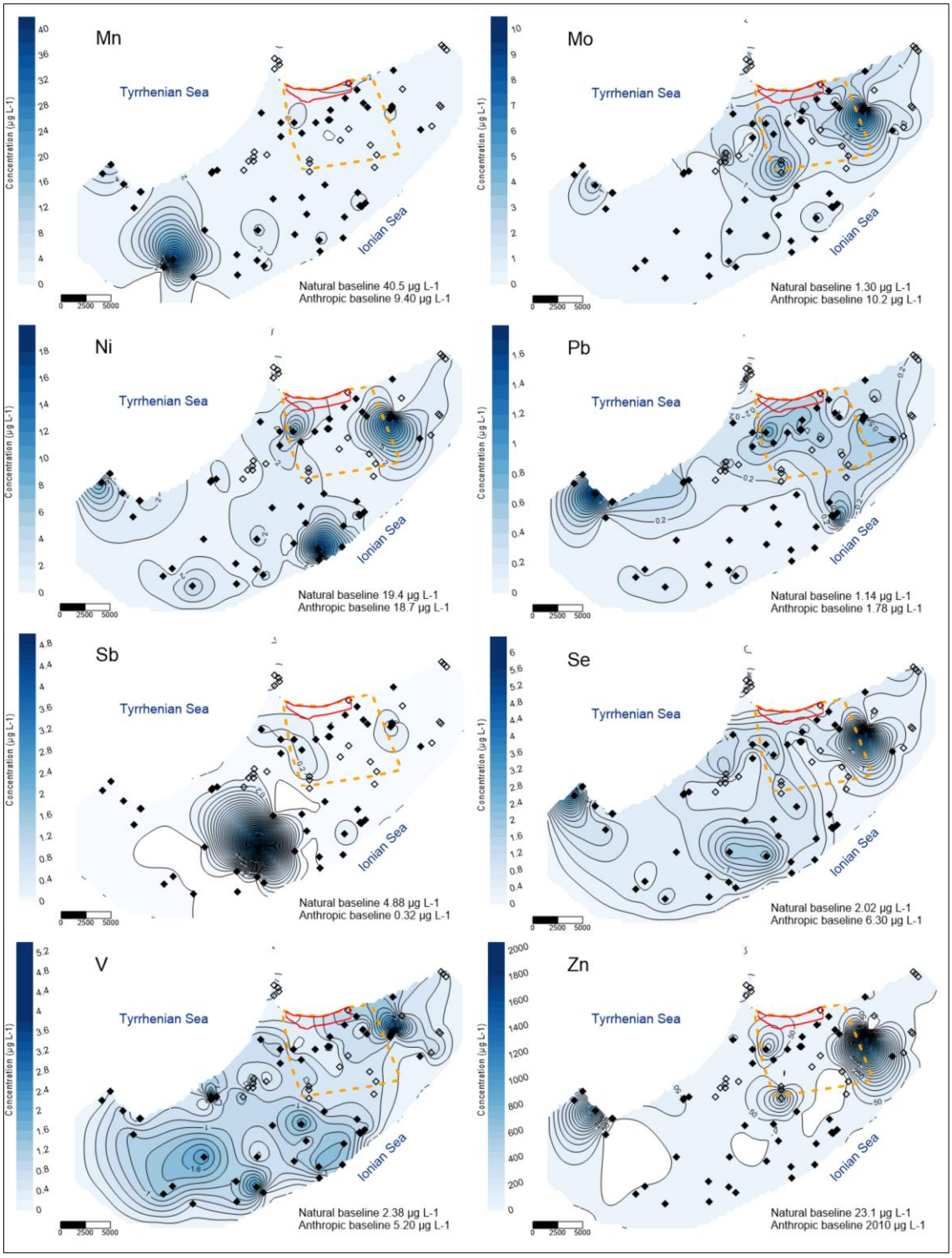

Figure 3.41 – Spatial distribution of Mn, Mo, Ni, Pb, Sb, Se, V, and Zn in water samples. The filled rhombuses represent the pure samples used to calculate the natural and anthropic geochemical baseline values. The empty rhombuses represent the blended samples excluded from the calculation. The industrial plant is marked in red, and the boundary of the Site of National Interest for remediation (SIN) is outlined in orange.

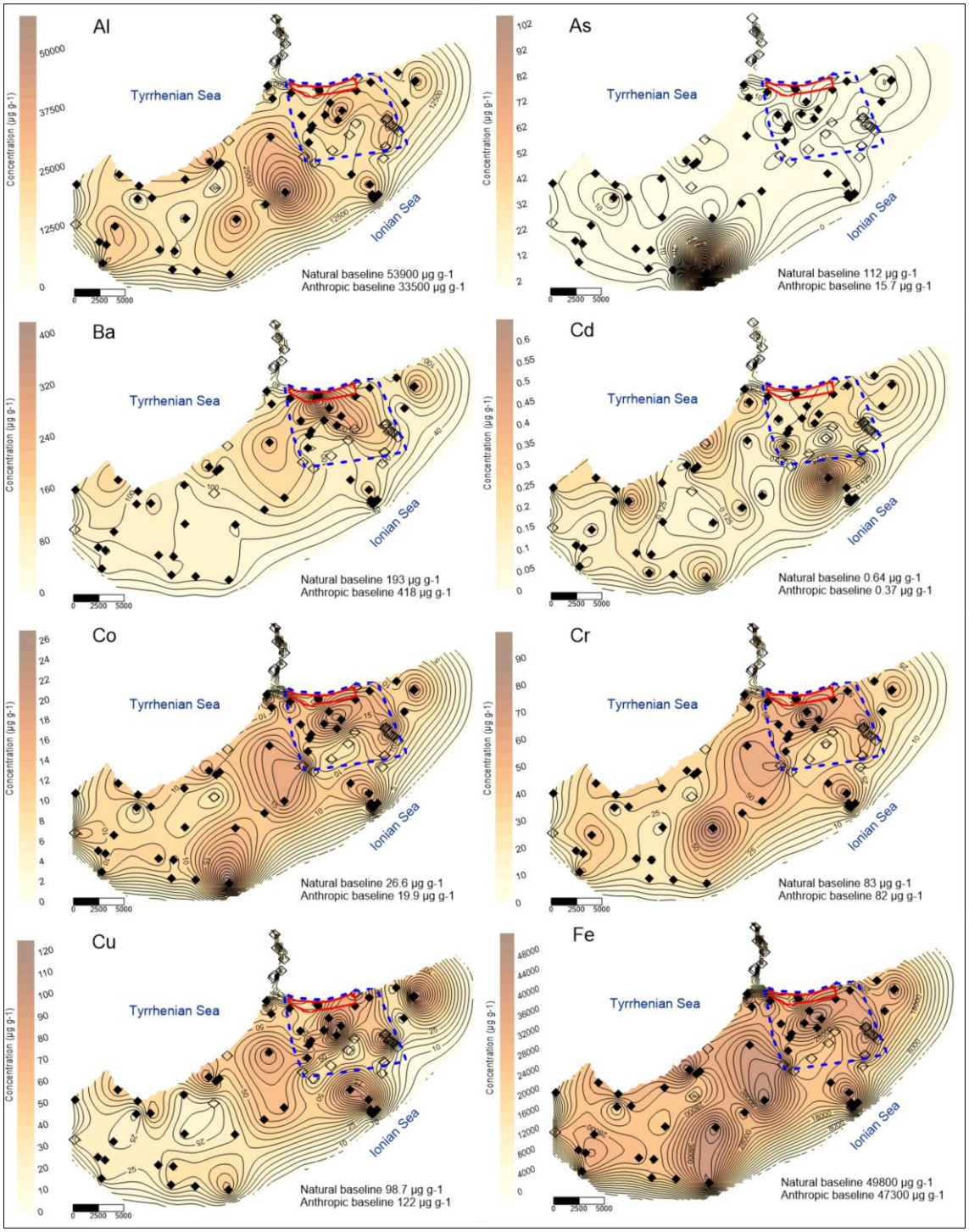

Figure 3.42 – Spatial distribution of Al, As, Ba, Cd, Co, Cr, Cu, and Fe in topsoil samples. The filled rhombuses represent the pure samples used to calculate the natural and anthropic geochemical baseline values. The empty rhombuses represent the blended samples excluded from the calculation. The industrial plant is marked in red, and the boundary of the Site of National Interest for remediation (SIN) is outlined in blue.

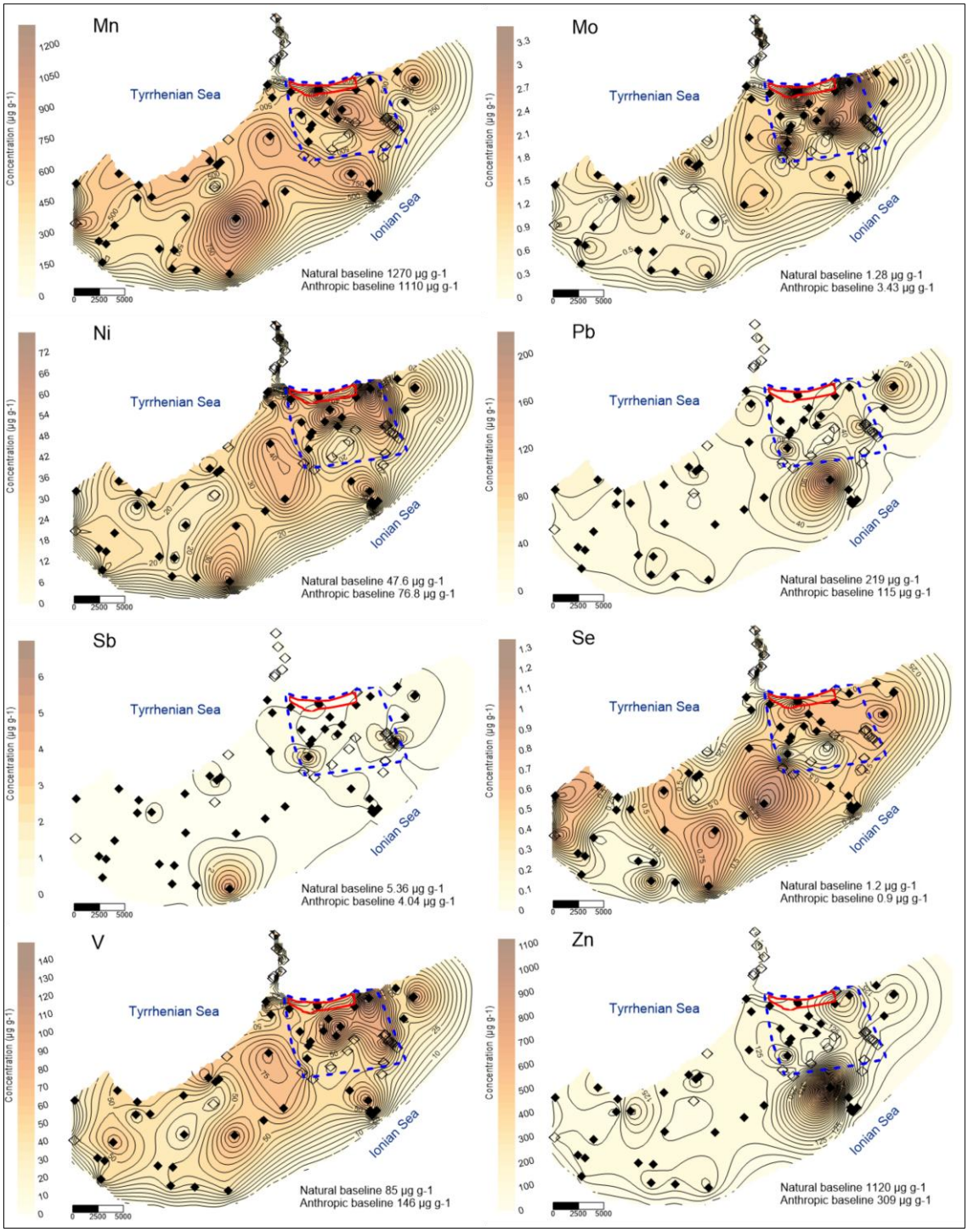

Figure 3.43 – Spatial distribution of Mn, Mo, Ni, Pb, Sb, Se, V, and Zn in topsoil samples. The filled rhombuses represent the pure samples used to calculate the natural and anthropic geochemical baseline values. The empty rhombuses represent the blended samples excluded from the calculation. The industrial plant is marked in red, and the boundary of the Site of National Interest for remediation (SIN) is outlined in blue.

The use of local geochemical baseline values helps distinguish between contaminated and uncontaminated areas (Baize and Sterckeman, 2001; Lo Medico et al., 2025; López et al., 2008; Négrel et al., 2015; Salminen et al., 2004; Sappa et al., 2020; Tack et al., 2005; Tarvainen and Paukola, 1998; Varrica et al., 2024; Wang et al., 2007; Yongming et al., 2006). To evaluate the contamination status of blended samples, several contamination indicators were employed, including

the geo-accumulation Index (I_{geo}), Enrichment Factor (EF), Contamination Factor (CF), Contamination degree (Cd), Ecological Risk Index (ERI), and Pollutant Load Index (PLI). Natural Baselines (NB) were used as reference values, providing a consistent, site-specific framework for comparison. For blended topsoil sample, the analysis of the geo-accumulation Index (I_{geo}) (Fig. 3.44) shows that nearly all elements, except for Mo, display an "uncontaminated" status ($I_{geo}<0$), with negative median values (Muller, 1969). For Mo, we observe an uncontaminated to moderately contaminated condition ($0 < I_{geo} \leq 1$).

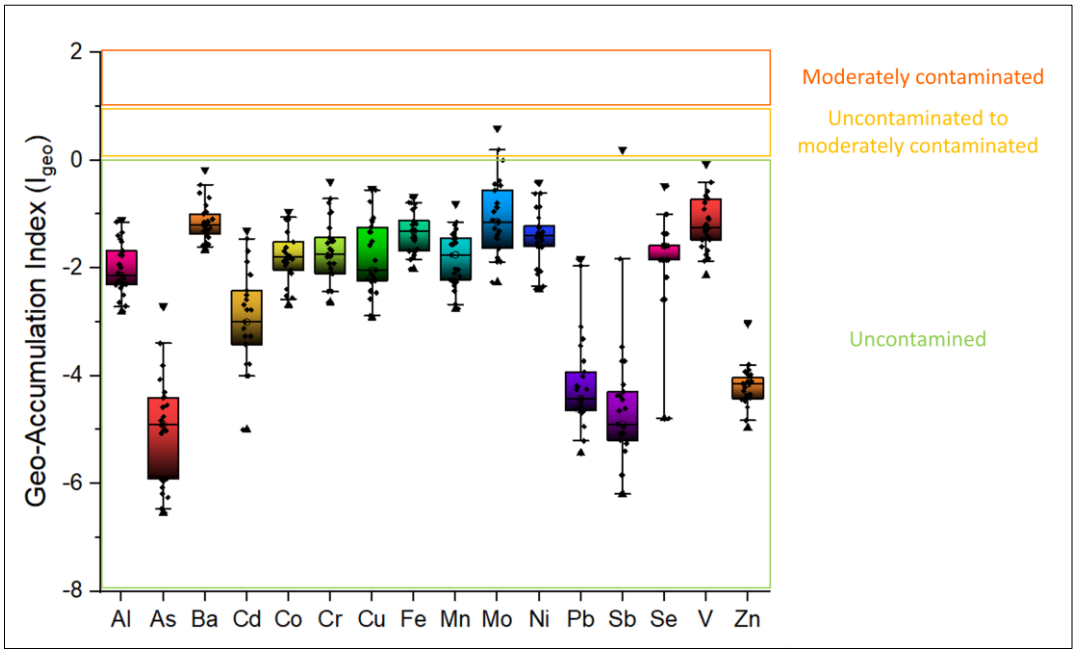

Figure 3.44 – Geo-Accumulation Index (I_{geo}) calculated for blended topsoil samples

Similar results are observed in the EF calculations, where all medians are below 2, indicating conditions ranging from deficiency to minimal enrichment (Yongming et al., 2006). However, some samples for elements such as Ba, Cu, Mn, Mo, Ni, Sb, Se, and V reach maximum EF values between 2 and 5, indicating moderate to significant enrichment (Fig.3.45). Only Mo shows an EF value >5, indicating significant enrichment.

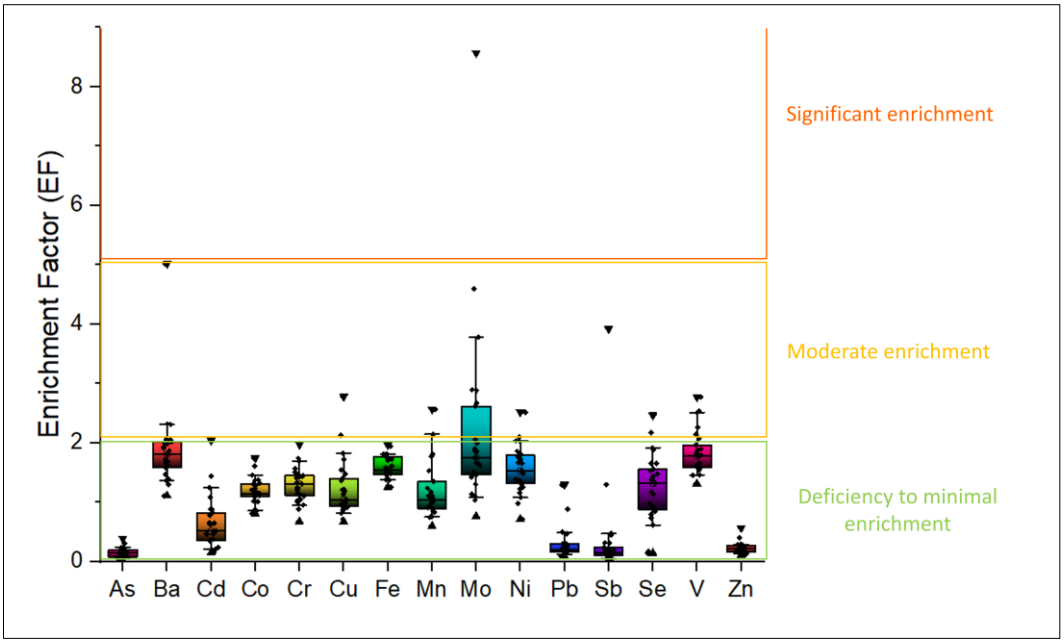

Figure 3.45 –Enrichment Factor (EF) calculated for blended topsoil samples.

Median CF values (Table 3.20) indicate a non-contaminated state (CF = 0-1); however, maximum values exceed this range for some elements (Ba, Cr, Cu, Mo, Ni, Sb, Se, V), suggesting uneven anthropogenic impacts. In particular, elements such as Ba, Cr, Cu, Ni, Sb, Se, and V show a state of suspected contamination (CF=1-2), while Mo shows a slight contamination state (CF=2-3.5). ERI values are below 40, indicating a low risk (Chen et al., 2024).

Table 3.20 - Contamination Factor (CF), and Ecological risk index (ERI) calculated for blended topsoil samples.

		Al	*As*	*Ba*	*Cd*	*Co*	*Cr*	*Cu*	*Fe*	*Mn*	*Mo*	*Ni*	*Pb*	*Sb*	*Se*	*V*	*Zn*
	Maximum	0.70	0.23	1.33	0.61	0.77	1.14	1.04	0.94	0.86	2.27	1.13	0.42	1.72	1.08	1.44	0.18
CF	Minimum	0.21	0.02	0.47	0.05	0.23	0.24	0.20	0.37	0.22	0.31	0.29	0.03	0.02	0.05	0.34	0.05
	Median	0.34	0.05	0.65	0.19	0.43	0.45	0.36	0.60	0.44	0.68	0.57	0.07	0.05	0.50	0.64	0.08
	Maximum		2.29		18.28	3.87	2.29	5.57	0.94	0.86		5.66	2.11	8.62		2.87	0.18
ERI	Minimum		0.16		1.41	1.17	0.48	0.99	0.37	0.22		1.43	0.17	0.10		0.68	0.05
	Median		0.50		6.56	2.17	0.88	1.95	0.59	0.48		2.77	0.39	0.30		1.28	0.08

For Cd, median values below 6 are noted (Tab.3.21), while maximum Cd values point to moderate contamination levels (6 < Cd < 12) (Hakanson, 1980). The Pollution Load Index (PLI) indicates a condition ranging from unpolluted to moderately polluted (0 < PLI ≤ 1), according to Tomlinson et al. (1980) (Tab.3.22).

Table 3.21 - Contamination Degree (C_d), and Pollution Load Index (PLI) calculated for blended topsoil samples.

Cd			*PLI*		
Maximum	Minimun	Median	Maximum	Minimun	Median
8.1	2.64	4.94	0.48	0.16	0.28

For blended water samples, the median Contamination Factor (CF) values (Tab. 3.22), based on Rutkowski et al. (2020), show that most elements remain in a non-contaminated state (CF = 0-1), except for Mo, which suggests possible contamination (CF = 1-2). The maximum CF values exceed the non-contaminated threshold (CF = 0–1): Ba shows a suspected contamination status (CF = 1–2), Cr and Mo exhibit slight contamination (CF = 2–3.5), while Cu and Zn reach moderate (CF = 3.5–8) and severe (CF = 8–27) contamination levels, respectively. These results imply uneven anthropogenic impact and potential contamination. The Ecological Risk Index (ERI) values are below 40 (Tab. 3.22), indicating low risk (Chen et al., 2024).

Table 3.22 - Contamination Factor (CF), and Ecological risk index (ERI) calculated for blended waters samples.

		Al	*As*	*Ba*	*Cd*	*Co*	*Cr*	*Cu*	*Fe*	*Mn*	*Mo*	*Ni*	*Pb*	*Sb*	*Se*	*V*	*Zn*
CF	Maximum	0.29	0.32	1.13	0.36	0.31	2.23	4.79	0.38	0.16	3.15	0.10	0.72	0.06	0.74	0.49	18.27
	Minimum	0.00	0.00	0.12	0.01	0.01	0.12	0.21	0.01	0.00	0.15	0.01	0.03	0.00	0.08	0.04	0.03
	Median	0.09	0.05	0.36	0.08	0.05	0.46	0.71	0.13	0.01	1.15	0.05	0.22	0.01	0.30	0.21	0.66
ERI	Maximum		3.24		10.88	1.54	4.45	23.94	0.38	0.16		0.52	3.60	0.30		0.97	18.27
	Minimum		0.05		0.41	0.07	0.25	1.06	0.01	0.00		0.03	0.13	0.00		0.08	0.03
	Median		0.51		2.50	0.23	0.92	3.56	0.13	0.01		0.23	1.10	0.04		0.42	0.66

For Contamination degree (Cd) median values are below 6 (Tab.3.23), however, maximum values indicate considerable contamination levels (Cd 12-24) (Hakanson, 1980). The Pollution Load Index (PLI) indicates a condition ranging from unpolluted to moderately polluted ($0 < PLI \leq 1$), according to Tomlinson et al. (1980) (Tab.3.23).

Table 3.23 - Contamination Degree (C_d), and Pollution Load Index (PLI) calculated for blended waters samples.

Cd			*PLI*		
Maximum	Maximum	Maximum	Maximum	Maximum	Maximum
24.0	2.17	5.64	0.29	0.05	0.13

The combined use of different indices, each highlighting specific aspects of the contamination phenomenon, from deviations from natural baseline values to estimates of potential ecological risks, has enhanced the overall robustness of the assessment. The results clearly show potential contamination hotspots. In this context, using local geochemical baselines (NB), applied to water and topsoil samples collected in blended areas, has proven to be a crucial approach for delineating the contamination status and more accurately pinpointing areas of high environmental concern.

In environmental geochemistry, biomonitoring is one of the most commonly used screening methods for an initial evaluation of contamination in areas exposed to intense human activity. A major challenge in interpreting biogeochemical data is distinguishing between elements from soil and those from human activities. The use of site-specific baseline values improves the reliability of contamination assessments when calculating contamination indices. However, a significant issue in applying these indices is choosing the appropriate reference substrate (Reimann and de Caritat, 2000,

2005). Relying on a generic substrate, such as the average composition of the Earth's crust, often leads to discrepancies from the local geological composition and can cause assessment errors. Several studies have demonstrated that using locally established baseline values provides a more reliable fondation for calculating and interpreting contamination indices (Sierra et al., 2015; Varrica et al., 2024; Yongming et al., 2006). Once natural baseline values for soils in the study area are established, it becomes possible to evaluate air quality contamination through biomonitoring. This evaluation is further supported by the calculation of the Enrichment Factor (EF). The EF values, calculated from pine needle samples, highlight the presence of potential contamination hotspots. The EF values show different scenarios, depending on the elements analyzed. For elements such as As, Ba, Co, Cr, Fe, V, Ni, Pb, and Zn, the EF values range from conditions of deficiency to minimal enrichment (EF<2) to Significant enrichment (5 < EF < 20). Elements such as Cu and Sb, show a more marked enrichment, with values even reaching very high enrichment (20 < EF < 40), while Se, Cd, Mn, and particularly Mo, show the greatest variability, with some areas exhibiting extremely high enrichment (EF > 40). Spatial analysis (Fig.3.46-3.47) of the distribution of EF values reveals common patterns for several elements, including As, Cd, Cr, Cu, Fe, Mn, Mo, Ni, Pb, Sb, V, and Zn. These elements tend to form contamination hotspots near the main anthropogenic sources, with dispersion that more or less follows the prevailing wind direction (W-WNW and SSE), thus facilitating the transport of contamination towards the hinterland. In contrast, elements such as Ba and Se show a more diffuse and less concentrated distribution. The Capo Milazzo area warrants particular attention, where contamination hotspots are observed for some elements, particularly As, Cr, and Ni; in this area, a contribution from the aeolian arc cannot be ruled out, as also suggested by the results obtained from lead isotopic analysis. The Ecological Risk Index (ERI) values are below 40, indicating low risk (Chen et al., 2024).

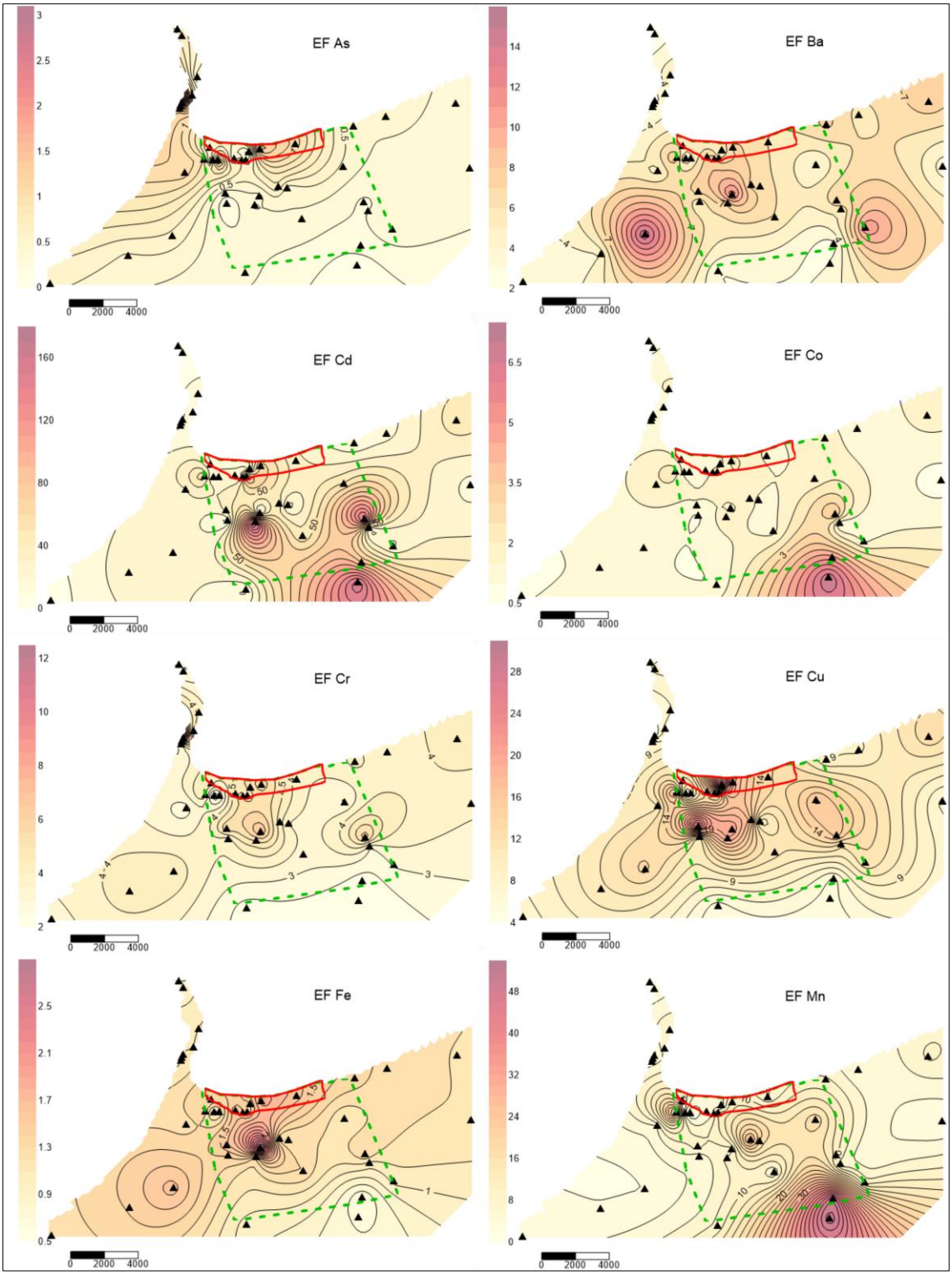

Figure 3.46 - Distribution maps of Enrichment Factors (EF) for As, Ba, Cd, Co, Cr, Cu, Fe, and Mn in pine needle samples. The industrial plant is marked in red, and the boundary of the Site of National Interest for remediation (SIN) is outlined in green.

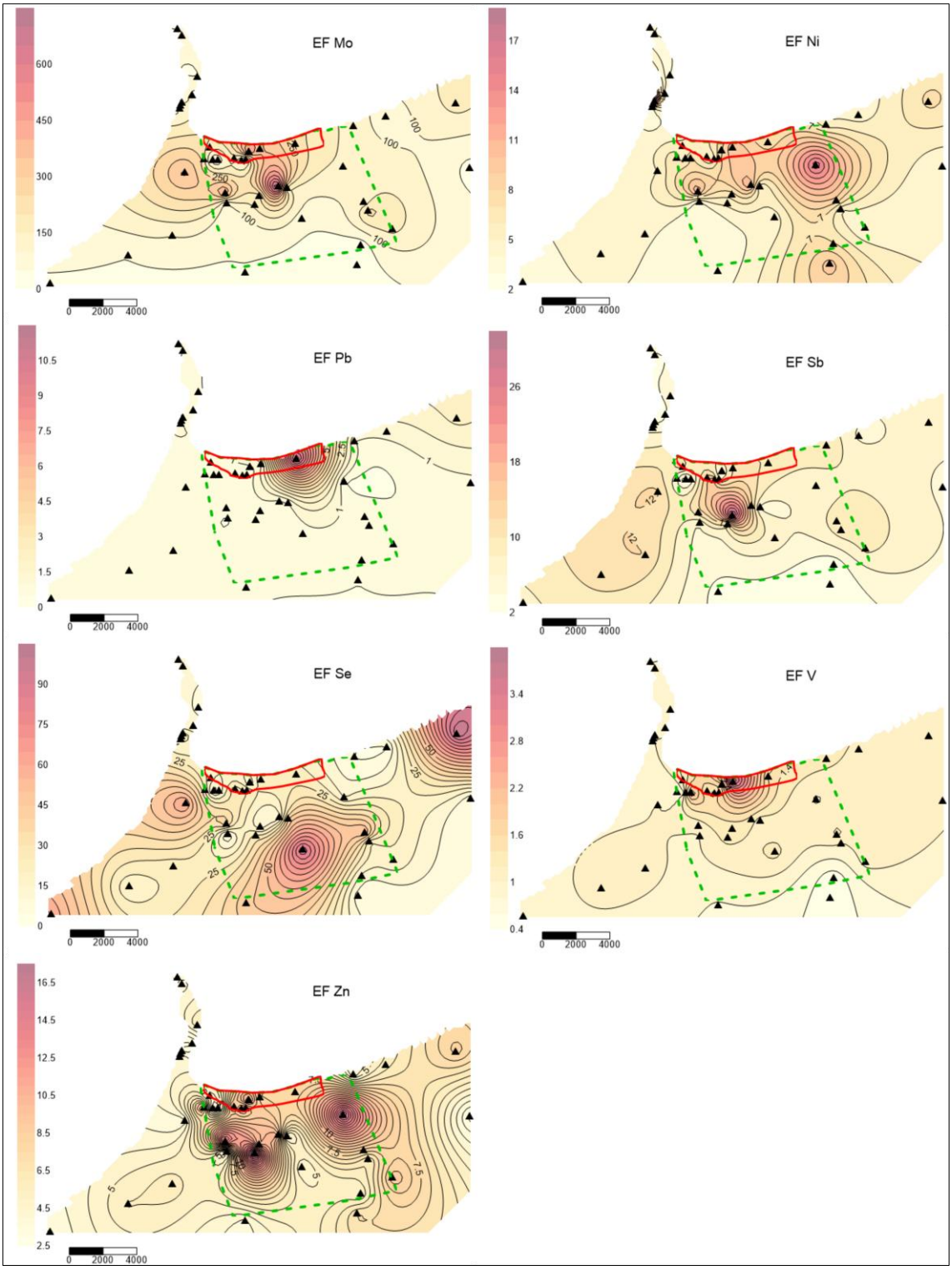

Figure 3.47 - Distribution maps of Enrichment Factors (EF) for Mo, Ni, Pb, Sb, Se, V, and Zn in pine needle samples. The industrial plant is marked in red, and the boundary of the Site of National Interest for remediation (SIN) is outlined in green.

4. Conclusion

This study introduces and validates an innovative approach for establishing site-specific geochemical baseline values in complex environmental settings where natural and anthropogenic signatures overlap. The Valle del Mela district, designated as a Site of National Interest (SIN) for remediation, was selected as an ideal location to explore a heterogeneous geochemical environment influenced by both natural and anthropogenic factors. Previous research has shown that the distribution and level of trace elements are affected by geogenic inputs, mainly the local geology, as well as human sources, such as refineries, power plants, waste incineration, and heavy traffic. A key finding is that using generic regulatory thresholds, which are not tailored to the local context, can cause significant misinterpretations because they fail to clearly differentiate between natural anomalies and human-related contamination. Defining site-specific geochemical baseline values has proven essential not only for more accurate interpretation of contamination but also for the developing scientifically sound environmental cleanup policies.

From a methodological perspective, this study stands out for its strong integration of analytical, statistical, and geostatistical methods, outlined through the following steps:

- the adoption of a multi-matrix framework (waters, topsoils, pine needles) enabled us to capture the system's complexity and to identify convergences and divergences among environmental compartments;

- the extensive sampling across the study area and analysis of a wide range of trace elements (Al, As, B, Ba, Cd, Co, Cr, Cu, Fe, Mn, Mo, Ni, Pb, Sb, Se, V, and Zn) which are relevant to both national and international for water and soil regulations, together with Rare Earth Elements (Y, La, Ce, Pr, Nd, Sm, Eu, Gd, Tb, Dy, Ho, Er, Tm, Yb, and Lu), provided a comprehensive geochemical dataset to distinguish natural from anthropogenic signatures;

- The application of Compositional Data Analysis (CoDa) overcame the limitations of traditional concentration-based methods, allowing the identification of geochemical fingerprints independent of absolute values, with a clear differentiation between natural and anthropogenic samples;

- the development of the Compositional Pollution Index (CPI) represents a novel contribution, providing a robust quantification of anthropogenic pressure;

- the combined use of Sequential Gaussian Simulation (SGS) and Local G spatial statistics ensured cross-validation of identified geochemical domains (natural and anthropogenic), reinforcing the robustness and reproducibility of the results;

- the use of sparse Linear Discriminant Analysis (sLDA) applied to water and topsoil datasets, achieving classification accuracies of 83.5% and 78.4%, respectively, further validated the methodological approach.

This methodology identified the presence of two geochemical domains in both water and soil: natural (in the westernmost part of the study area, aligned with the Peloritani Mountains crest) and anthropogenic (along the coast and within the SIN).

Local G maps obtained from pine needles and the results of Pb stable isotope analyses in pine needles, water, and soil provide independent and consistent validation in the identification of geochemical domains. The pine needles Local G maps highlight a clear anthropogenic dominance concentrated within the SIN, while the isotopic results outline a complex environmental scenario, in which geogenic and anthropogenic contributions coexist. The isotopic signatures show that the influence of industrial emissions is particularly marked in the areas adjacent to the SIN, while the more inland and less urbanized areas near the Peloritani Mountains crest are characterized by natural signals. Furthermore, isotopic analysis identified a third population of samples for which a mixed contribution was observed, attributable to both the local geological substrate and inputs from anthropogenic activities.

The core of methodology lies in the overlap analysis of water and topsoil Local G maps, which allowed us to identify areas where the two matrices consistently indicated natural or anthropogenic domains. The high level of concordance between waters and soils (77%) in classifying natural and anthropogenic domains allowed to identify samples within these zones, forming the basis for the calculation of natural and anthropic baselines using the UTL95-95 BCA-Bootstrap method.

The resulting baseline values reflect the specific geochemical characteristics of the study area. Two baseline values were established: a Natural Baseline (NB), and Anthropic Baseline (AB). These baseline values highlight the area's unique geochemical features. High NB levels of Al, As, Mn, and Sb in water samples, and of Al, As, Mn, Pb, Sb, and Zn in topsoil samples, match the mineralogical makeup of the study area. Conversely, elevated AB levels of Ba, Cr, Cu, Mo, Se, V, and Zn in water samples, along with Ba, Cu, Mo, Ni, and V in topsoil samples, point to human-related sources.

The multi-matrix approach identified a third cluster of blended samples, representing areas where discrepancies between water and soil classifications appeared. These samples indicate areas where natural and anthropogenic influences actively interact, resisting direct categorization. Instead, their

categorization is element-dependent, displaying concentrations that may be similar to natural or anthropic baseline values. To assess the contamination status of these samples, several contamination indicators were used, including the geo-accumulation Index (I_{geo}), the Enrichment Factor (EF), the Contamination Factor (CF), the Contamination degree (Cd), the Ecological Risk Index (ERI), and the Pollutant Load Index (PLI). Natural geochemical baselines were adopted as reference values, ensuring a consistent and site-specific comparison framework. Overall, the results highlight the presence of potential contamination in the hotspots.

Baseline soil geochemical values were used to assess air contamination through biomonitoring. This assessment was performed by calculating the Enrichment Factor (EF) on pine needle samples. The results highlighted the presence of potential contamination hotspots. Spatial analysis of the EF distribution highlights common patterns for several elements, including As, Cd, Cr, Cu, Fe, Mn, Mo, Ni, Pb, Sb, V, and Zn. These elements tend to form contamination hotspots near the main anthropogenic sources, with dispersion following the prevailing wind direction (W-WNW and SSE), which favors the transport of contamination inland.

Overall, this research develops a transferable methodological framework that tackles one of the main challenges in environmental geochemistry: defining geochemical baselines in areas where natural and anthropogenic signatures overlap. The uniqueness of the study lies in its integrative approach, combining multi-matrix analysis, CoDa-based statistical methods, and advanced geostatistical modeling. The simultaneous application and mutual validation of these approaches provide site-specific baseline values and introduce new interpretive categories, such as blended samples, which capture the dynamic nature of contaminant transport and accumulation. Although designed for the Valle del Mela district, the methodology is naturally adaptable and can be used in other locations with similar geochemical complexities. Its transferability makes it relevant beyond the local context, serving as a model for environmental monitoring, risk assessment, and management. Future research will aim to improve the methodology through more multidisciplinary approaches and extending its application to different environmental scenarios, supporting science-based policies for sustainable and resilient management of contaminated and high-risk areas. This approach marks a crucial step toward a more integrated, context-aware, and sustainability focused fiels of applied geochemistry.

References

Abbaszade, G., Tserendorj, D., Salazar-Yanez, N., Zacháry, D., Völgyesi, P., Tóth, E., Szabó, C., 2022. Lead and stable lead isotopes as tracers of soil pollution and human health risk assessment in former industrial cities of Hungary. Appl. Geochem. 145, 105397. https://doi.org/10.1016/j.apgeochem.2022.105397

Adeniyi, A.A., 1996. Determination of cadmium, copper, iron, lead, manganese and zinc in water leaf (Talinumtriangularia) in dump sites. Environ. Int. 22, 259–262.

Adriano, D.C., 2001. Trace elements in the terrestrial environments: biogeochemistry, bioavailability, and risks of metals. New York: Springer.

Ahlberg, G., Gustafsson, O., Wedel, P., 2006. Leaching of metals from sewage sludge during one year and their relationship to particle size. Environ. Pollut. 144, 545–553. https://doi.org/10.1016/j.envpol.2006.01.022

Aitchinson, J., 1986. The Statistical Analysis of Compositional Data. Chapman & Hall Ltd. London.

Aitchison, J., 1983. Principal component analysis of compositional data. Biometrika 70, 57–65. https://doi.org/10.1093/biomet/70.1.57

Aitchison, J., 1982. The Statistical Analysis of Compositional Data. Journal of the Royal Statistical Society Series B: Statistical Methodology 44, 139–160. https://doi.org/10.1111/j.2517-6161.1982.tb01195.x

Aitchison, J., Greenacre, M., 2002. Biplots of Compositional Data. Journal of the Royal Statistical Society Series C: Applied Statistics 51, 375–392. https://doi.org/10.1111/1467-9876.00275

Akoto, R., Anning, A.K., 2021. Heavy metal enrichment and potential ecological risks from different solid mine wastes at a mine site in Ghana. Enviro. Adv. 3, 100028. https://doi.org/10.1016/j.envadv.2020.100028

Alaimo, M.G., Dongarrà, G., Melati, M.R., Monna, F., Varrica, D., 2000. Recognition of environmental trace metal contamination using pine needles as bioindicators. The urban area of Palermo (Italy). Environ. Geol. 39, 914–924. https://doi.org/10.1007/s002549900071

Albanese, S., De Vivo, B., Lima, A., Cicchella, D., 2007a. Geochemical background and baseline values of toxic elements in stream sediments of Campania region (Italy). Journal of Geochemical Exploration 93, 21–34. https://doi.org/10.1016/j.gexplo.2006.07.006

Albanese, S., De Vivo, B., Lima, A., Cicchella, D., 2007b. Geochemical background and baseline values of toxic elements in stream sediments of Campania region (Italy). J. Geochem. Explor. 93, 21–34. https://doi.org/10.1016/j.gexplo.2006.07.006

Albuquerque, M.T.D., Gerassis, S., Sierra, C., Taboada, J., Martín, J.E., Antunes, I.M.H.R., Gallego, J.R., 2017. Developing a new Bayesian Risk Index for risk evaluation of soil contamination. Sci. Total Environ. 603–604, 167–177. https://doi.org/10.1016/j.scitotenv.2017.06.068

Albuquerque, T., Fonseca, R., Araújo, J., Silva, N., Araújo, A., 2024. Stream sediment pollution: a compositional baseline assessment. Euro-Mediterr. J. Environ. Integr. 9, 1021–1031. https://doi.org/10.1007/s41207-024-00470-x

Algeo, T.J., Hong, H., Wang, C., 2025. The chemical index of alteration (CIA) and interpretation of ACNK diagrams. Chem. Geol. 671, 122474. https://doi.org/10.1016/j.chemgeo.2024.122474

Allison, Brown, D.S., Novo-Gradac, K.J., 1991. MINTEQA2, a geochemical assessment model for environmental systems. Report EPA/600/3-91/0-21. USEPA, Athens, Georgia.

Ambrosino, M., El-Saadani, Z., Khatita, A., Mingqi, W., Palarea-Albaladejo, J., Cicchella, D., 2023. Geochemical Speciation, Ecological Risk and Assessment of Main Sources of Potentially Toxic Elements (PTEs) in Stream Sediments from Nile River in Egypt. Water 15, 2308. https://doi.org/10.3390/w15132308

Ambrosino, M., Palarea-Albaladejo, J., Albanese, S., Lin, X., Ciarcia, S., Cicchella, D., 2025. Assessing natural background concentrations of chemical elements in urban soils: A case study in Benevento (Italy). Sci. Total Environ. 975, 179298. https://doi.org/10.1016/j.scitotenv.2025.179298

Amiard, J.C., Amiard-Triquet, C., Méayer, C., Salanki, J., 1995. Experimental study of bioaccumulation, toxicity, and regulation of some trace metals in various estuarine and coastal organisms., in: Proceedings of the Symposium on Heavy Metals in Water Organisms. Budapest, Hungary, Akademiai Kiado, pp. 313–324.

Anders, E., Ebihara, M., 1982. Solar-system abundances of the elements. Geoch. Cosm. Act. 46, 2363–2380.

ASTM Committee D-18 on Soil and Rock., 1963. ASTM D422-63: Standard test method for particle-size analysis of soils.

Bai, T., Tahmasebi, P., 2022. Sequential Gaussian simulation for geosystems modeling: A machine learning approach. Geosci. Front. 13, 101258. https://doi.org/10.1016/j.gsf.2021.101258

Baize, D., Sterckeman, T., 2001. Of the necessity of knowledge of the natural pedo-geochemical background content in the evaluation of the contamination of soils by trace elements. Sci. Total Environ. 264, 127–139. https://doi.org/10.1016/S0048-9697(00)00615-X

Baldanza, B., 1949. Primi risultati delle ricerche eseguite sulle mineralizzazioni dei Monti Peloritani (I minerali della contrada Tripi del comune di Alì, prov. di Messina). Rend. Soc. Min. Ital. ANNO IV, 1–8.

Barbera, G., Lo Giudice, A., Mazzoleni, P., Pappalardo, A., 2009. Combined statistical and petrological analysis of provenance and diagenetic history of mudrocks: Application to Alpine Tethydes shales (Sicily, Italy). Sediment. Geol. 213, 27–40. https://doi.org/10.1016/j.sedgeo.2008.11.002

Barrat, J.-A., Bayon, G., Lalonde, S., 2023. Calculation of cerium and lanthanum anomalies in geological and environmental samples. Chem. Geol. 615, 121202. https://doi.org/10.1016/j.chemgeo.2022.121202

Bau, M., 1999. Scavenging of dissolved yttrium and rare earths by precipitating iron oxyhydroxide: experimental evidence for Ce oxidation, Y-Ho fractionation, and lanthanide tetrad effect. Geoch. Cosm. Act. 63, 67–77. https://doi.org/10.1016/S0016-7037(99)00014-9

Bau, M., 1991. Rare-earth element mobility during hydrothermal and metamorphic fluid-rock interaction and the significance of the oxidation state of europium. Chem. Geol. 93, 219–230. https://doi.org/10.1016/0009-2541(91)90115-8

Bau, M., Dulski, P., 1996. Distribution of yttrium and rare-earth elements in the Penge and Kuruman iron-formations, Transvaal Supergroup, South Africa. Precambrian Research 79, 37–55. https://doi.org/10.1016/0301-9268(95)00087-9

Bau, M., Dulski, P., Möller, P., 1995. Yttrium and holmium in South Pacific seawater: vertical distribution and possible fractionation mechanisms. Chem. Erde. 55, 1–15.

Bau, M., Knappe, A., Dulski, P., 2006. Anthropogenic gadolinium as a micropollutant in river waters in Pennsylvania and in Lake Erie, northeastern United States. Geochem. 66, 143–152. https://doi.org/10.1016/j.chemer.2006.01.002

Belzile, N., Chen, Y.-W., Wang, Z., 2001. Oxidation of antimony (III) by amorphous iron and manganese oxyhydroxides. Chem. Geol. 174, 379–387. https://doi.org/10.1016/S0009-2541(00)00287-4

Berg, A., Banwart, S.A., 2000. Carbon dioxide mediated dissolution of Ca-feldspar: implications for silicate weathering. Chem. Geol. 163, 25–42. https://doi.org/10.1016/S0009-2541(99)00132-1

Bergallo, M., Ferrara, V., Pennisi, A., 1993. Lineamenti idrogeologici e vulnerabilità all'inqui- namento degli acquiferi della fascia costiera tirrenica del Messinese (versante settentrionale dei M. Peloritani - Sicilia NE)., in: Atti Congr. ANDIS '93. pp. 17–31.

Bertolotti, G., Gialanella, S., 2014. Review: use of conifer needles as passive samplers of inorganic pollutants in air quality monitoring. Anal. Methods 6, 6208. https://doi.org/10.1039/C4AY00172A

Besag, J., Newell, J., 1991. The Detection of Clusters in Rare Diseases. J R Stat Soc Ser A 154, 143. https://doi.org/10.2307/2982708

Bini, C., Sartori, G., Wahsha, M., Fontana, S., 2011. Background levels of trace elements and soil geochemistry at regional level in NE Italy. Journal of Geochemical Exploration 109, 125–133. https://doi.org/10.1016/j.gexplo.2010.07.008

BioMedware, 2021. SpaceStat - Software for the analysis and exploration of spatiotemporal data.

Boente, C., Albuquerque, M.T.D., Gallego, J.R., Pawlowsky-Glahn, V., Egozcue, J.J., 2022. Compositional baseline assessments to address soil pollution: An application in Langreo, Spain. Sci. Total Environ. 812, 152383. https://doi.org/10.1016/j.scitotenv.2021.152383

Bollhöfer, A., Rosman, K.J.R., 2000. Isotopic source signatures for atmospheric lead: the Southern Hemisphere. Geoch. Cosm. Act. 64, 3251–3262. https://doi.org/10.1016/S0016-7037(00)00436-1

Bonardi, G., De Vivo, B., Giunta, G., Perrone, V., 1982. I conglomerati rossi dei Monti Peloritani e considerazioni sull'Unità di Novara. Boll. Soc. Geol. It. 101, 157–172.

Bonardi, G., Giunta, G., Perrone, V., Russo, M., Zuppetta, A., Ciampo, G., 1980. Osservazioni sull'evoluzione dell'Arco Calabro-Peloritano nel Miocene inferiore: la Formazione di Stilo - Capo d'Orlando. Boll. Soc. Geol. It. 99, 365–393.

Bozau, E., Stärk, H.-J., Strauch, G., 2013. Hydrogeochemical characteristics of spring water in the Harz Mountains, Germany. Geochem. 73, 283–292. https://doi.org/10.1016/j.chemer.2013.02.002

Briffa, J., Sinagra, E., Blundell, R., 2020. Heavy metal pollution in the environment and their toxicological effects on humans. Heliyon 6, e04691. https://doi.org/10.1016/j.heliyon.2020.e04691

Brioschi, L., Steinmann, M., Lucot, E., Pierret, M.C., Stille, P., Prunier, J., Badot, P.M., 2013. Transfer of rare earth elements (REE) from natural soil to plant systems: implications for the environmental availability of anthropogenic REE. Plant Soil 366, 143–163. https://doi.org/10.1007/s11104-012-1407-0

Brookins, D.G., 1989. Aqueous geochemistry of rare earth elements. RiMG 21, 201–225.

Brookins, D.G., 1983. Eh-pH diagrams for the rare earth elements at 25 °C and one bar pressure. 17, 223–229.

Brugnone, F., Calabrese, S., Parello, F., Li Vigni, L., Saiano, F., Liotta, M., Bellomo, S., Sprovieri, M., 2023. Major ions and trace elements composition of rainwater around the two industrial areas of Milazzo and Priolo Gargallo (Sicily - Italy).

Brugnone, F., D'Alessandro, W., Liotta, M., Bitetto, M., Randazzo, L., Bellomo, S., Brusca, L., Cilluffo, G., Parello, F., Calabrese, S., 2025. Source apportionment of major ions and trace elements in the atmospheric deposition of Palermo (Sicily, Italy). Atmos. Pollut. Res. 16, 102431. https://doi.org/10.1016/j.apr.2025.102431

Buccianti, A., Pawlowsky-Glahn, V., 2005. New Perspectives on Water Chemistry and Compositional Data Analysis. Math. Geosci. 37, 703–727. https://doi.org/10.1007/s11004-005-7376-6

Cabral Pinto, M.M.S., Silva, M.M.V.G., Ferreira Da Silva, E.A., Dinis, P.A., Rocha, F., 2017. Transfer processes of potentially toxic elements (PTE) from rocks to soils and the origin of PTE in soils: A case study on the island of Santiago (Cape Verde). Journal of Geochemical Exploration 183, 140–151. https://doi.org/10.1016/j.gexplo.2017.06.004

Cangemi, M., Madonia, P., Albano, L., Bonfardeci, A., Di Figlia, M.G., Di Martino, R.M.R., Nicolosi, M., Favara, R., 2019. Heavy Metal Concentrations in the Groundwater of the Barcellona-Milazzo Plain (Italy): Contributions from Geogenic and Anthropogenic Sources. Int. J. Environ. Res. Public Health. 16, 285. https://doi.org/10.3390/ijerph16020285

Cannon, H.L., Connally, G.G., Epstein, J.B., Parker, J.G., Thornton, I., Wixson, G., 1978. Rocks: geological sources of most trace elements. In: Report to the workshop at south seas plantation Captiva Island, FL, US. Environ. Geochem. 3, 17–31.

Cao, C., Liu, X.-M., Chen, J., 2022. Cerium anomaly as a tracer for paleo-oceanic redox conditions: A thermodynamics-based Ce oxidation modeling approach. Front. Earth Sci. 10, 927826. https://doi.org/10.3389/feart.2022.927826

Carbone, S., Messina, A., Lentini, F., Barbano, M.S., Grasso, D., Di Stefano, A., Ferrara, V., Somma, R., Chiocci, F.L., Catalano, R., Di Geronimo, I., Critelli, S., Agate, M., Barone, M., Dominici, R., Marchetti, M., Martorelli, E., Rosso, A., Sulli, A., Valenti, V., Zanini, A., Falcini, F., Sprovieri, R., Incarbona, A., 2023. CARG - CARtografia Geologica di Italia-Note illustrative della Carta Geologica d'Italia, foglio 601 (Messina-Reggio Calabria).

Carbone, S., Messina, A., Lentini, F., Macaione, E., 2011. CARG - CARtografia Geologica di Italia- Note illustrative della Carta Geologica d'Italia, fogli 587 e 600 (Milazzo-Barcellona P.G.).

Casiot, C., Ujevic, M., Munoz, M., Seidel, J.L., Elbaz-Poulichet, F., 2007. Antimony and arsenic mobility in a creek draining an antimony mine abandoned 85 years ago (upper Orb basin, France). Appl. Geochem. 22, 788–798. https://doi.org/10.1016/j.apgeochem.2006.11.007

Chakhmouradian, A.R., Wall, F., 2012. Rare Earth Elements: Minerals, Mines, Magnets (and More). Elements 8, 333–340. https://doi.org/10.2113/gselements.8.5.333

Chang, C., Fu, Q., Wang, X., 2019. Linear Correlation of Ba and Eu Contents by Hydrothermal Activities: A Case Study in the Hetang Formation, South China. Geofluids 2019, 1–15. https://doi.org/10.1155/2019/9797326

Charlesworth, S., De Miguel, E., Ordóñez, A., 2011. A review of the distribution of particulate trace elements in urban terrestrial environments and its application to considerations of risk. Environ. Geochem. Health. 33, 103–123. https://doi.org/10.1007/s10653-010-9325-7

Chen, J., Algeo, T.J., Zhao, L., Chen, Z.-Q., Cao, L., Zhang, L., Li, Y., 2015. Diagenetic uptake of rare earth elements by bioapatite, with an example from Lower Triassic conodonts of South China. Earth-Science Reviews 149, 181–202. https://doi.org/10.1016/j.earscirev.2015.01.013

Chen, J., Yang, R., 2010. Analysis on REE geochemical characteristics of three types of REE-rich soil in Guizhou Province, China. J. Rare Earths 28, 517–522. https://doi.org/10.1016/S1002-0721(10)60271-2

Chen, M., Ma, L.Q., Harris, W.G., 1999. Baseline Concentrations of 15 Trace Elements in Florida Surface Soils. J. Env. Quality 28, 1173–1181. https://doi.org/10.2134/jeq1999.00472425002800040018x

Chen, X., Gao, F., Cao, Y., Fu, Y., Li, H., Wang, M., Pan, Q., 2024. In situ formation of copper nanoclusters for efficient analysis of β-glucosidase activity. Microchemical Journal 196, 109546. https://doi.org/10.1016/j.microc.2023.109546

Chen, Y., Ning, Y., Bi, X., Liu, J., Yang, S., Liu, Z., Huang, W., 2022. Pine needles as urban atmospheric pollution indicators: Heavy metal concentrations and Pb isotopic source identification. Chemosphere 296, 134043. https://doi.org/10.1016/j.chemosphere.2022.134043

J. Chiarenzelli, L. Aspler, C. Dunn, B. Cousens, D. Ozarko, K. Powis, 2001. Multi-element and rare earth element composition of lichens, mosses, and vascular plants from the Central Barrenlands, Nunavut, Canada. Applied Geochemistry, 16, 245-270. https://doi.org/10.1016/S0883-2927(00)00027-5

Cicchella, D., De Vivo, B., Lima, A., 2005. Background and baseline concentration values of elements harmful to human health in the volcanic soils of the metropolitan and provincial areas of Napoli (Italy). GEEA 5, 29–40. https://doi.org/10.1144/1467-7873/03-042

Cidu, R., Vittori Antisari, L., Biddau, R., Buscaroli, A., Carbone, S., Da Pelo, S., Dinelli, E., Vianello, G., Zannoni, D., 2013. Dynamics of rare earth elements in water–soil systems: The case study of the Pineta San Vitale (Ravenna, Italy). Geoderma 193–194, 52–67. https://doi.org/10.1016/j.geoderma.2012.10.009

Clemmensen, L., Hastie, T., Witten, D., Ersbøll, B., 2011. Sparse Discriminant Analysis. Technometrics 53, 406–413. https://doi.org/10.1198/TECH.2011.08118

Coltro, R., Ferrara, V., Roda, C., 1980. Relazione tra acque superficiali e falde subalvee nelle fiumare., in: Atti 4° Conv. Int. Acque Sotterranee, Acireale 17-21 Febbraio 1980. pp. 211–237.

Comas-Cufí, M., Thió-Henestrosa, S., 2011. CoDaPack 2.0: a stand-alone, multi-platform compositional software.In: Egozcue JJ, Tolosana-Delgado R, Ortego MI, eds. CoDaWork'11: 4th International Workshop on Compositional Data Analysis.

Correia, A., Rasteiro, M., 2025. A Review of Persistent Soil Contaminants: Assessment and Remediation Strategies. Environments 12, 229. https://doi.org/10.3390/environments12070229

Cosenza, A., Lima, A., Ayuso, R.A., Foley, N.K., Albanese, S., Messina, A., De Vivo, B., 2015. Soil geochemical survey of abandoned mining sites in the Eastern-Central Peloritani Mountains, Sicily, Italy. GEEA 15, 361–372. https://doi.org/10.1144/geochem2014-307

De Bartolomeo, A., Poletti, L., Sanchini, G., Sebastiani, B., Morozzi, G., 2004. Relationship among parameters of lake polluted sediments evaluated by multivariate statistical analysis. Chemosphere 55, 1323–1329. https://doi.org/10.1016/j.chemosphere.2003.12.005

De Souza, E.S., Texeira, R.A., Da Costa, H.S.C., Oliveira, F.J., Melo, L.C.A., Do Carmo Freitas Faial, K., Fernandes, A.R., 2017. Assessment of risk to human health from simultaneous exposure to multiple contaminants in an artisanal gold mine in Serra Pelada, Pará, Brazil. Sci. Total Environ. 576, 683–695. https://doi.org/10.1016/j.scitotenv.2016.10.133

De Vivo, B., 1982. Mineral resources of the Calabria-Peloritani Arc: Genetic aspects in the evolution of the Arc. Earth Evolution Sciences 3, 187–196.

De Vivo, B., Sava, A., Villani, V., Messina, A., 1999. Cartografia Geochimica dei monti Peloritani (Sicilia). - Estratto da MEMORIE DESCRITTIVE DELLA CARTA GEOLOGICA D'ITALIA LV, 33–47.

Deutsch, C.V., Journel, A.G., 1998. GSLIB: Geostatistical Software Library and User's Guide, 2nd ed. Oxford University Press, New York.

Dia, A., Gruau, G., Olivié-Lauquet, G., Riou, C., Molénat, J., Curmi, P., 2000. The distribution of rare earth elements in groundwaters: assessing the role of source-rock composition, redox changes and colloidal particles. Geoch. Cosm. Act. 64, 4131–4151. https://doi.org/10.1016/S0016-7037(00)00494-4

Dinelli, E., Lima, A., Albanese, S., Birke, M., Cicchella, D., Giaccio, L., Valera, P., De Vivo, B., 2012. Major and trace elements in tap water from Italy. J. Geochem. Explor. 112, 54–75. https://doi.org/10.1016/j.gexplo.2011.07.009

Dongarrà, G., Manno, E., Sabatino, G., Varrica, D., 2009. Geochemical characteristics of waters in mineralised area of Peloritani Mountains (Sicily, Italy). Appl. Geochem. 24, 900–914. https://doi.org/10.1016/j.apgeochem.2009.02.002

Dongarrà, G., Varrica, D., 1998. The presence of heavy metals in air particulate at Vulcano island (Italy). Science of The Total Environment, 212, 1-9. https://doi.org/10.1016/S0048-9697(97)00323-9

Dubinin, A.V., 2004. Geochemistry of Rare Earth Elements in the Ocean. Lithology and Mineral Resources 39, 289–307. https://doi.org/10.1023/B:LIMI.0000033816.14825.a2

Duplay, J., Semhi, K., Mey, M., Messina, A., Quaranta, G., Huber, F., Aubert, A., 2014. Geogenic versus anthropogenic geochemical influence on trace elements contents in soils from the Milazzo Peninsula. Geochem. 74, 691–704. https://doi.org/10.1016/j.chemer.2014.04.006

Dupré, B., Dessert, C., Oliva, P., Goddéris, Y., Viers, J., François, L., Millot, R., Gaillardet, J., 2003. Rivers, chemical weathering and Earth's climate. C. R. - Geosci. 335, 1141–1160. https://doi.org/10.1016/j.crte.2003.09.015

Duvert, C., Cendón, D.I., Raiber, M., Seidel, J.-L., Cox, M.E., 2015. Seasonal and spatial variations in rare earth elements to identify inter-aquifer linkages and recharge processes in an Australian catchment. Chem. Geol. 396, 83–97. https://doi.org/10.1016/j.chemgeo.2014.12.022

Efron, B., Narasimhan, B., 2020. The Automatic Construction of Bootstrap Confidence Intervals. JCGS 29, 608–619. https://doi.org/10.1080/10618600.2020.1714633

Efron, B., Tibshirani, R.J., 1994. An Introduction to the Bootstrap, 0 ed. Chapman and Hall/CRC. https://doi.org/10.1201/9780429246593

Egli, M., Merkli, C., Sartori, G., Mirabella, A., Plötze, M., 2008. Weathering, mineralogical evolution and soil organic matter along a Holocene soil toposequence developed on carbonate-rich materials. Geomorphology 97, 675–696. https://doi.org/10.1016/j.geomorph.2007.09.011

Egozcue, J.J., Pawlowsky-Glahn, V., Mateu-Figueras, G., 2003. Isometric Logratio Transformations for Compositional Data Analysis. Math. Geol. 35, 279–300. https://doi.org/10.1023/A:1023818214614

European Union, 2020. Directive (EU) 2020/2184 of the European Parliament and of the Council of 16 December 2020 on the Quality of Water Intended for Human Consumption (recast).

European Union, 2010. Directive 2010/75/EU of the European Parliament and of the Council of 24 November 2010 on industrial emissions (integrated pollution prevention and control) (recast).

European Union, 2000. Directive 2000/60/EC of 23 October 2000 establishing a framework for Community action in the field of water policy.

Fabian, C., Reimann, C., Fabian, K., Birke, M., Baritz, R., Haslinger, E., 2014. GEMAS: Spatial distribution of the pH of European agricultural and grazing land soil. Appl. Geochem. 48, 207–216. https://doi.org/10.1016/j.apgeochem.2014.07.017

Facchinelli, A., Sacchi, E., Mallen, L., 2001. Multivariate statistical and GIS-based approach to identify heavy metal sources in soils. Environ. Pollut. 114, 313–324. https://doi.org/10.1016/S0269-7491(00)00243-8

Fedo, C.M., Wayne Nesbitt, H., Young, G.M., 1995. Unraveling the effects of potassium metasomatism in sedimentary rocks and paleosols, with implications for paleoweathering conditions and provenance. Geology 23, 921. https://doi.org/10.1130/0091-7613(1995)023%253C0921:UTEOPM%253E2.3.CO;2

Ferla, P., 2000. A model of continental crust evolution in the geological history of the Peloritani Mountains (Sicily). Mem . Soc . Geol . It . 55, 87–93.

Ferla, P., Lorenzoni, S., Zanettin Lorenzoni, E., 1983. Geological costruction and evolution of the Calabro-Peloritan Hercynian range. Rend. S.I.M.P. 38, 951–962.

Ferla, P., Omenetto, P., 2000. Metallogenic evolution of Peloritani Mountains (NE Sicily): a summary. Mem. Soc. Geol. Ital 55 293–297.

Fernandes, A.R., Souza, E.S.D., De Souza Braz, A.M., Birani, S.M., Alleoni, L.R.F., 2018. Quality reference values and background concentrations of potentially toxic elements in soils from the Eastern Amazon, Brazil. J. Geochem. Explor. 190, 453–463. https://doi.org/10.1016/j.gexplo.2018.04.012

Ferrara, V., 1987. Aspetti connessi alla vulnerabilità degli acquiferi alluvionali nei bacini dei corsi d'acqua minori della Sicilia nord-orientale. Boll. Mus. St. Nat. Lunigiana 6–7, 427–430.

Ferrari, M., Medici, D., 1996. Alberi e arbusti in Italia. Edagricole, Bologna.

Feth, J.H., Roberson, C.E., Polzer, 1964. Sources of mineral constituents in water from granitic rocks, Sierra Nevada, California and Nevada. https://doi.org/10.3133/wsp1535I

Filzmoser, P., Hron, K., 2011. Compositional data analysis: theory and applications. In: Pawlowsky-Glahn V, Buccianti A (eds) Compositional data analysis: theory and applications. 59–72.

Filzmoser, P., Hron, K., Templ, M., 2018. Applied Compositional Data Analysis: With Worked Examples in R, Springer Series in Statistics. Springer International Publishing, Cham. https://doi.org/10.1007/978-3-319-96422-5

Frattini, P., De Vivo, B., Lima, A., Cicchella, D., 2006. Elemental and gamma-ray surveys in the volcanic soils of Ischia Island, Italy. GEEA 6, 325–339. https://doi.org/10.1144/1467-7873/06-105

Galán, E., Fernández-Caliani, J.C., González, I., Aparicio, P., Romero, A., 2008. Influence of geological setting on geochemical baselines of trace elements in soils. Application to soils of South–West Spain. J. Geochem. Explor. 98, 89–106. https://doi.org/10.1016/j.gexplo.2008.01.001

Gałuszka, A., 2007a. A review of geochemical background concepts and an example using data from Poland. Environ. Geochem. 52, 861–870. https://doi.org/10.1007/s00254-006-0528-2

Gałuszka, A., 2007b. Different approaches in using and understanding the term "geochemical background" –practical implications for environmental studies. Pol. J. Environ. Stud. 16(3), 389–395.

Gałuszka, A., 2006. Methods of determining geochemical background in environmental studies. Landsc. Ecol. XVI/1, 507–519.

Gałuszka, A., Migaszewski, Z., 2011. Geochemical background - an environmental perspective. Mineralogia 42, 7–17. https://doi.org/10.2478/v10002-011-0002-y

Gammons, C.H., Wood, S.A., Nimick, D.A., 2005. Diel behavior of rare earth elements in a mountain stream with acidic to neutral pH. Geoch. Cosm. Act. 69, 3747–3758. https://doi.org/10.1016/j.gca.2005.03.019

Gao, X., Han, G., Liu, J., Zhang, S., 2023. Spatial Distribution and Sources of Rare Earth Elements in Urban River Water: The Indicators of Anthropogenic Inputs. Water 15, 654. https://doi.org/10.3390/w15040654

Garrels, R.M., 1967. Genesis of some ground waters from igneous rocks. Geochem. 2, John Wiley&sons, 405–420.

Gasparo Morticelli, M.; Valenti, V.; Catalano, R.; Sulli, A.; Agate, M.; Avellone, G.; Albanese, C.; Basilone, L.; Gugliotta, C. 2015.Deep controls on foreland basin system evolution along the Sicilian fold and thrust belt. *Bull. Soc. Géol. De Fr.*, *186*, 273–290

Getis, A., Ord, J.K., 1992. The Analysis of Spatial Association by Use of Distance Statistics. Geogr. Anal. 24, 189–206. https://doi.org/10.1111/j.1538-4632.1992.tb00261.x

Giunta, G., Nigro, F., 1999. Tectono-sedimentary constraints to the Oligocene-to-Miocene evolution of the Peloritani thrust belt (NE Sicily). Tectonophysics 315, 287–299. https://doi.org/10.1016/S0040-1951(99)00283-8

Göb, S., Loges, A., Nolde, N., Bau, M., Jacob, D.E., Markl, G., 2013. Major and trace element compositions (including REE) of mineral, thermal, mine and surface waters in SW Germany and implications for water–rock interaction. Applied Geochemistry 33, 127–152. https://doi.org/10.1016/j.apgeochem.2013.02.006

Goovaerts, P., 1997. Geostatistics for natural resources evaluation. Oxford university press.

Gorelick, S.M., Freeze, R.A., Donohue, D., Keely, J.F., 1993. Groundwater Contamination: Optimal Capture and Containment. Lewis Publishers, Boca Raton, FL.

Gosselin, D.C., Smith, M.R., Lepel, E.A., Laul, J.C., 1992. Rare earth elements in chloride-rich groundwater, Palo Duro Basin, Texas, USA. Geoch. Cosm. Act. 56, 1495–1505. https://doi.org/10.1016/0016-7037(92)90219-9

Grodzinka, k, 1982. Monitoring of air pollutants by mosses and tree bark - In: Monitoring of Air Pollutants by Plants, Steubing, L., and Jäger, H. J. (eds.), Dr W. Junk Publishers. The Hague 33–42.

Gruba, P., Socha, J., 2016. Effect of parent material on soil acidity and carbon content in soils under silver fir (Abies alba Mill.) stands in Poland. CATENA 140, 90–95. https://doi.org/10.1016/j.catena.2016.01.020

Hakanson, L., 1980. An ecological risk index for aquatic pollution control.a sedimentological approach. Water Research 14, 975–1001. https://doi.org/10.1016/0043-1354(80)90143-8

Hawkes, H.E., Webb, J.S., 1962. Geochemistry in mineral exploration. Harper & Row, New York.

Hepler, P.K., 2005. Calcium: A Central Regulator of Plant Growth and Development. Plant Cell 17, 2142–2155. https://doi.org/10.1105/tpc.105.032508

Hiller, S., 2003. Quantitative Analysis of Clay and other Minerals in Sandstones by X-Ray Powder Diffraction (XRPD), in: Clay Mineral Cements in Sandstones. pp. 313–251.

Holoubek, I., Kořínek, P., Šeda, Z., Schneiderová, E., Holoubková, I., Pacl, A., Tříska, J., Cudlín, P., Čáslavský, J., 2000. The use of mosses and pine needles to detect persistent organic pollutants at local and regional scales. Environ. Pollut. 109, 283–292. https://doi.org/10.1016/S0269-7491(99)00260-2

Hopper, J.F., Ross, H.B., Sturges, W.T., Barrie, L.A., 1991. Regional source discrimination of atmospheric aerosols in Europe using the isotopic composition of lead. Tellus 43, 45. https://doi.org/10.3402/tellusb.v43i1.15245

Huang, S., Yamaji, N., Ma, J.F., 2024. Metal Transport Systems in Plants. Annu. Rev. Plant Biol. 75, 1–25. https://doi.org/10.1146/annurev-arplant-062923-021424

Huhn, G., Schulz, H., Stärk, H.J., Töll, R., Schüürmann, G., 1995. Evaluation of regional heavy metal deposition by multivariate analysis of lement contents in pine tree barks. Water, Air and Soil Pollution 84, 367–383.

Ion, A., Cosac, A., 2023. Rare earth elements distribution in topsoil from Ditrău Alkaline Massif area, eastern Carpathians, Romania. Heliyon 9, e13976. https://doi.org/10.1016/j.heliyon.2023.e13976

Isaaks, E.H., Srivastava, R.M., 1989. An Introduction to Applied Geostαtistics, 1st ed. New York : Oxford University Press.

Islam, S., Ahmed, K., Habibullah-Al-Mamun, Masunaga, S., 2015. Potential ecological risk of hazardous elements in different land-use urban soils of Bangladesh. Sci. Total Environ. 512–513, 94–102. https://doi.org/10.1016/j.scitotenv.2014.12.100

Janssen, R.P.T., Verweij, W., 2003. Geochemistry of some rare earth elements in groundwater, Vierlingsbeek, The Netherlands. Water Res. 37, 1320–1350. https://doi.org/10.1016/S0043-1354(02)00492-X

Jenks, G.F., 1967. The data model concept in statistical mapping. Int Yearbook Cartogr 7, 186–190.

Johannesson, K.H., Chevis, D.A., Burdige, D.J., Cable, J.E., Martin, J.B., Roy, M., 2011. Submarine groundwater discharge is an important net source of light and middle REEs to coastal waters of the Indian River Lagoon, Florida, USA. Geoch. Cosm. Act. 75, 825–843. https://doi.org/10.1016/j.gca.2010.11.005

Johannesson, K.H., Lyons, W.B., Yelken, M.A., Gaudette, H.E., Stetzenbach, K.J., 1996. Geochemistry of the rare-earth elements in hypersaline and dilute acidic natural terrestrial waters: Complexation behavior and middle rare-earth element enrichments. Chem. Geol. 133, 125–144. https://doi.org/10.1016/S0009-2541(96)00072-1

Johannesson, K.H., Stetzenbach, K.J., Hodge, V.F., 1997. Rare earth elements as geochemical tracers of regional groundwater mixing. Geoch. Cosm. Act. 61, 3605–3618. https://doi.org/10.1016/S0016-7037(97)00177-4

Johannesson, K.H., Zhou, X., Guo, C., Stetzenbach, K.J., Hodge, V.F., 2000. Origin of rare earth element signatures in groundwaters of circumneutral pH from southern Nevada and eastern California, USA. Chem. Geol. 164, 239–257. https://doi.org/10.1016/S0009-2541(99)00152-7

Jordens, A., Cheng, Y.P., Waters, K.E., 2013. A review of the beneficiation of rare earth element bearing minerals. Miner. Eng. 41, 97–114. https://doi.org/10.1016/j.mineng.2012.10.017

Journel, A.G., Huijbregts, C.J., 1978. Mining geostatistics. United Kingdom.

Juranović Cindrić, I., Zeiner, M., Starčević, A., Stingeder, G., 2019. Metals in pine needles: characterisation of bio-indicators depending on species. Int. J. Environ. Sci. Technol. 16, 4339–4346. https://doi.org/10.1007/s13762-018-2096-x

Kaczor-Kurzawa, D., Wysocka, I., Chuchro, M., 2024. The behavior of the rare earth elements and yttrium in groundwaters of the Holy Cross Mountains, SE Poland. J. Geochem. Explor. 263, 107493. https://doi.org/10.1016/j.gexplo.2024.107493

Kaczor-Kurzawa, D., Wysocka, I., Porowski, A., Drzewicz, P., Vassileva, E., 2022. The occurrence and distribution of rare earth elements in mineral and thermal waters in the Polish Lowlands. J. Geochem. Explor. 237, 106984. https://doi.org/10.1016/j.gexplo.2022.106984

Kandziora-Ciupa, M., Ciepał, R., Nadgórska-Socha, A., Barczyk, G., 2016. Accumulation of heavy metals and antioxidant responses in Pinus sylvestris L. needles in polluted and non-polluted sites. Ecotoxicology 25, 970–981. https://doi.org/10.1007/s10646-016-1654-6

Kawabe, I., Ohta, A., Miura, N., 1999. Distribution coefficients of REE between Fe oxyhydroxide precipitates and NaCl solutions affected by REE-carbonate complexation. Geochem. J. 33, 181–197. https://doi.org/10.2343/geochemj.33.181

Kicińska, A., Turek, K., 2017. Establishing geochemical background of elements present in soil and its application in the evaluation of soil pollution based on data collected in the Beskid Sądecki region. GP 16, 87–99. https://doi.org/10.4467/21995923GP.17.007.7194

Kitto, M.E., Anderson, D.L., Gordon, G.E., Olmez, I., 1992. Rare Earth Distributions in Catalysts and Airborne Particles. Environ. Sci. Technol. 26.

Kobina Mensah, A., Amoakwah, E., 2024. Soil Biogeochemical Factors Influencing Mobilization of Toxic Elements in Mine-Contaminated Soils and Remediation Potential of Plants, in: Rehman Hakeem, K. (Ed.), Environmental Sciences. IntechOpen. https://doi.org/10.5772/intechopen.1005487

Komárek, M., Ettler, V., Chrastný, V., Mihaljevič, M., 2008. Lead isotopes in environmental sciences: A review. Environ. Int. 34, 562–577. https://doi.org/10.1016/j.envint.2007.10.005

Kord, B., Mataji, A., Babaie, S., 2010. Pine (Pinus Eldarica Medw.) needles as indicator for heavy metals pollution. Int. J. Environ. Sci. Technol. 7, 79–84. https://doi.org/10.1007/BF03326119

Korfali, S.I., Davies, B.E., 2004. Speciation of metals in sediment and water in a river underlain by limestone: role of carbonate species for purification capacity of rivers. AER 8, 599–612. https://doi.org/10.1016/S1093-0191(03)00033-9

Kosiorek, M., Modrzewska, B., Wyszkowski, M., 2016. Levels of selected trace elements in Scots pine (Pinus sylvestris L.), silver birch (Betula pendula L.), and Norway maple (Acer platanoides L.) in an urbanized environment. Environ Monit Assess 188, 598. https://doi.org/10.1007/s10661-016-5600-0

Kottek, M., Grieser, J., Beck, C., Rudolf, B., Rubel, F., 2006. World Map of the Köppen-Geiger climate classification updated. metz 15, 259–263. https://doi.org/10.1127/0941-2948/2006/0130

Kowalska, J.B., Mazurek, R., Gąsiorek, M., Zaleski, T., 2018. Pollution indices as useful tools for the comprehensive evaluation of the degree of soil contamination–A review. EGAH 40, 2395–2420. https://doi.org/10.1007/s10653-018-0106-z

Kulaksız, S., Bau, M., 2013. Anthropogenic dissolved and colloid/nanoparticle-bound samarium, lanthanum and gadolinium in the Rhine River and the impending destruction of the natural rare earth element distribution in rivers. EPSL 362, 43–50. https://doi.org/10.1016/j.epsl.2012.11.033

Kulaksız, S., Bau, M., 2011. Rare earth elements in the Rhine River, Germany: First case of anthropogenic lanthanum as a dissolved microcontaminant in the hydrosphere. Environ. Int. 37, 973–979. https://doi.org/10.1016/j.envint.2011.02.018

Kulkarni, P., Chellam, S., Fraser, M.P., 2006. Lanthanum and lanthanides in atmospheric fine particles and their apportionment to refinery and petrochemical operations in Houston, TX. Atmos. Environ. 40, 508–520. https://doi.org/10.1016/j.atmosenv.2005.09.063Italian Law 426/1998.Nuovi interventi in campo ambientale.(GU n.291 del 14-12-1998)

Landajo, A., Arana, G., De Diego, A., Etxebarria, N., Zuloaga, O., Amouroux, D., 2004. Analysis of heavy metal distribution in superficial estuarine sediments (estuary of Bilbao, Basque Country) by open-focused microwave-assisted extraction and ICP-OES. Chemosphere 56, 1033–1041. https://doi.org/10.1016/j.chemosphere.2004.06.005

Langelier, W.F., Ludwig, H.F., 1942. Graphical Methods for Indicating the Mineral Character of Natural Waters. Journal AWWA 34, 335–352. https://doi.org/10.1002/j.1551-8833.1942.tb19682.x

Lasaga, A.C., 1984. Chemical kinetics of water-rock interactions. J. Geophys. Res. 89, 4009–4025. https://doi.org/10.1029/JB089iB06p04009

Laveuf, C., Cornu, S., 2009. A review on the potentiality of Rare Earth Elements to trace pedogenetic processes. Geoderma 154, 1–12. https://doi.org/10.1016/j.geoderma.2009.10.002

Lawrence, M.G., Greig, A., Collerson, K.D., Kamber, B.S., 2006. Rare Earth Element and Yttrium Variability in South East Queensland Waterways. Aquat. Geochem. 12, 39–72. https://doi.org/10.1007/s10498-005-4471-8

Lawrence, M.G., Kamber, B.S., 2006. The behaviour of the rare earth elements during estuarine mixing—revisited. Mar. Chem. 100, 147–161. https://doi.org/10.1016/j.marchem.2005.11.007

Lee, S.-G., Tanaka, T., Lee, M.J., 2023. Geochemical implication of Eu isotopic ratio in anorthosite: new evidence of Eu isotope fractionation during feldspar crystallization. Geosci. J. 27, 271–284. https://doi.org/10.1007/s12303-023-0009-6

Lehndorff, E., Schwark, L., 2010. Accumulation histories of major and trace elements on pine needles in the Cologne conurbation as function of air quality. Atmos. Environ. 44, 2822–2829.

Lentini, F., Carbone, S., 2014. Geologia della Sicilia—Geology of Sicily.

Leybourne, M.I., Goodfellow, W.D., Boyle, D.R., Hall, G.M., 2000. Rapid development of negative Ce anomalies in surface waters and contrasting REE patterns in groundwaters associated with Zn–Pb massive sulphide deposits. Appl. Geochem. 15, 695–723. https://doi.org/10.1016/S0883-2927(99)00096-7

Li, Q., Wang, Y., Li, Y., Li, L., Tang, M., Hu, W., Chen, L., Ai, S., 2022. Speciation of heavy metals in soils and their immobilization at micro-scale interfaces among diverse soil components. Sci. Total Environ. 825, 153862. https://doi.org/10.1016/j.scitotenv.2022.153862

Lippo, H., Poikolainen, J., Kubin, E., 1995. The use of moss, lichen and pine bark in the nationwide monitoring of atmospheric heavy metal deposition in Finland. Water, Air and Soil Pollution 85, 2241–2246.

Liu, H., Guo, H., Xing, L., Zhan, Y., Li, F., Shao, J., Niu, H., Liang, X., Li, C., 2016. Geochemical behaviors of rare earth elements in groundwater along a flow path in the North China Plain. J. Asian Earth Sci. 117, 33–51. https://doi.org/10.1016/j.jseaes.2015.11.021

Liu, J., Feng, M., Xiu, X., Liu, W., 2024. Towards robust and sparse linear discriminant analysis for image classification. Pattern Recognit. 153, 110512. https://doi.org/10.1016/j.patcog.2024.110512

Lo Medico, F., Varrica, D., Zuccolini, M.V., Miola, M., Scopelliti, G., Alaimo, M.G., 2025. Geochemical baseline values and spatial distribution of major, trace, and rare earth elements in unpolluted soils of the Sicily region (Italy). Environ Geochem Health 47, 167. https://doi.org/10.1007/s10653-025-02475-z

López, M., González, I., Romero, A., 2008. Trace elements contamination of agricultural soils affected by sulphide exploitation (Iberian Pyrite Belt, Sw Spain). Environ Geol 54, 805–818. https://doi.org/10.1007/s00254-007-0864-x

Löstschert, W., Köhm, H.J., 1978. Characteristics of tree bark as an indicator in high emission areas: II. Content of heavy metals. Oecologia 37, 121–132.

Lumivero, 2024. XLSTAT statistical and data analysis solution.

Manly, B.F.J., 1997. Randomization, Bootstrap and Monte Carlo Methods in Biology. Chapman and Hall/CRC.

Marini, L., 2007. Geological sequestration of carbon dioxide. Thermodynamics, kinetics, and reaction path modeling. Developments in Geochemistry.

Marschner, H., Marschner, P. (Eds.), 2012. Marschner's mineral nutrition of higher plants, 3rd ed. ed. Elsevier/Academic Press, London ; Waltham, MA.

Matheron, G., 1971. The theory of regionalized variables and Its applications. Les Cahiers du Centre de Morphologie Mathématique DE FONTAINEBLEAU. École Nationale Supérieure des Mines de Paris.

Matschullat, J., Ottenstein, R., Reimann, C., 2000. Geochemical background - can we calculate it? Environ Geol 39, 990–1000. https://doi.org/10.1007/s002549900084

McCleskey, R.B., 2018. Calculated specific conductance using PHREEQCI: U.S. Geological Survey software release.

McCleskey, R.B., Nordstrom, D.K., Ryan, J.N., 2012a. Comparison of electrical conductivity calculation methods for natural waters. L&O Methods 10, 952–967. https://doi.org/10.4319/lom.2012.10.952

McCleskey, R.B., Nordstrom, D.K., Ryan, J.N., Ball, J.W., 2012b. A new method of calculating electrical conductivity with applications to natural waters. Geoch. Cosm. Act. 77, 369–382. https://doi.org/10.1016/j.gca.2011.10.031

McLean, J.E., Bledsoe, B.E., 1992. EPA- Ground Water Issue - Behavior of Metals in Soils.

McLennan, S.M., 2001. Relationships between the trace element composition of sedimentary rocks and upper continental crust. Geochem Geophys Geosyst 2, 2000GC000109. https://doi.org/10.1029/2000GC000109

Messina, A., Somma, R., Lima, A.M., Macaione, E., Carbone, G., Carreri, C., 2004a. The abundance of 55 elements and petrovolumetric models of the Crust in the Peloritani Mountains. In: F.P. SASSI (Ed.): "The abundance of 55 elements and petrovolumetric models of the crust in 9 type areas from the crystalline basements of Italy, with some geophysical and petrophysical data". Accad. Nazionale delle Scienze detta dei XL 13, 411–450.

Messina, A., Somma, R., Macaione, E., Carbone, G., Careri, G., 2004b. Peloritani continental crust composition (southern Italy); geological and petrochemical evidence. IJG 3, 405–441.

Métrich, N., Bertagnini, A., Landi, P., Rosi, M., 2001. Crystallization Driven by Decompression and Water Loss at Stromboli Volcano (Aeolian Islands, Italy). J. Petrol. 42, 1471–1490. https://doi.org/10.1093/petrology/42.8.1471

Mey, M., 2013. The life cycle assessment of the Milazzo peninsula (north-eastern Sicily, Italy) : geochimical impact assessment of water and soils.

Mgbenu, C.N., Egbueri, J.C., 2019. The hydrogeochemical signatures, quality indices and health risk assessment of water resources in Umunya district, southeast Nigeria. Appl Water Sci 9, 22. https://doi.org/10.1007/s13201-019-0900-5

Miekeley, N., Coutinho De Jesus, H., Porto Da Silveira, C.L., Linsalata, P., Morse, R., 1992. Rare-earth elements in groundwaters from the Osamu Utsumi mine and Morro do Ferro analogue study sites, Poços de Caldas, Brazil. J. Geochem. Explor. 45, 365–387. https://doi.org/10.1016/0375-6742(92)90131-Q

Migaszewski, Z.M., Gałuszka, A., 2019. Pierwiastki ziem rzadkich w kwaśnych wodach kopalnianych – zarys problematyki. PG 67, 105–114. https://doi.org/10.7306/2019.2

Migaszewski, Z.M., Gałuszka, A., 2016. The use of gadolinium and europium concentrations as contaminant tracers in the Nida River watershed in south-central Poland. GQ 60. https://doi.org/10.7306/gq.1241

Migaszewski, Z.M., Gałuszka, A., 2015. The Characteristics, Occurrence, and Geochemical Behavior of Rare Earth Elements in the Environment: A Review. Crit Rev Environ Sci Technol 45, 429–471. https://doi.org/10.1080/10643389.2013.866622

Mihaljevič, M., 1999. Lead. Marshall C, Fairbridge R, editors. Encyclopedia of Geochemistry.Dordrecht: Kluwer Academic Publishers.

Mikkonen, H.G., Clarke, B.O., Dasika, R., Wallis, C.J., Reichman, S.M., 2017. Assessment of ambient background concentrations of elements in soil using combined survey and open-source data. Science of The Total Environment 580, 1410–1420. https://doi.org/10.1016/j.scitotenv.2016.12.106

Miró, M., Estela, J.M., Cerdà, V., 2004. Application of flowing stream techniques to water analysis. Talanta 63, 201–223. https://doi.org/10.1016/j.talanta.2003.10.047

Möller, P., 2002. The distribution of rare earth elements and yttrium in water-rock interactions: field observations and experiments, in: Stober, I., Bucher, K. (Eds.), Water-Rock Interaction, Water Science and Technology Library. Springer Netherlands, Dordrecht, pp. 97–123. https://doi.org/10.1007/978-94-010-0438-1_4

Möller, P., Bau, M., 1993. Rare-earth patterns with positive cerium anomaly in alkaline waters from Lake Van, Turkey. EPSL 117, 671–676. https://doi.org/10.1016/0012-821X(93)90110-U

Möller, P., Rosenthal, E., Dulski, P., Geyer, S., Guttman, Y., 2003. Rare earths and yttrium hydrostratigraphy along the Lake Kinneret–Dead Sea–Arava transform fault, Israel and adjoining territories. Appl. Geochem. 18, 1613–1628. https://doi.org/10.1016/S0883-2927(03)00044-1

Möller, P., Rosenthal, E., Inbar, N., Magri, F., 2016. Hydrochemical considerations for identifying water from basaltic aquifers: The Israeli experience. J. Hydrol. Reg. Stud. 5, 33–47. https://doi.org/10.1016/j.ejrh.2015.11.016

Monna, F., Aiuppa, A., Varrica, D., Dongarra, G., 1999. Pb Isotope Composition in Lichens and Aerosols from Eastern Sicily: Insights into the Regional Impact of Volcanoes on the Environment. Environ. Sci. Technol. 33, 2517–2523. https://doi.org/10.1021/es9812251

Monna, F., Loizeau, J.-L., Thomas, B., Guéguen, C., Favarger, P.-Y., Losno, R., Dominik, J., 2000. Noise identification and sampling frequency determination for precise Pb isotopic measurements by quadrupole-based Inductively Coupled Plasma Mass Spectrometry. Analusis 28, 750–757. https://doi.org/10.1051/analusis:2000146

Monna, F., Loizeau, J.-L., Thomas, B.A., Guéguen, C., Favarger, P.-Y., 1998. Pb and Sr isotope measurements by inductively coupled plasma–mass spectrometer: efficient time management for precision improvement. Spectrochim. Acta B At. spectrosc. 53, 1317–1333. https://doi.org/10.1016/S0584-8547(98)00164-5

Moreno, T., Kojima, T., Querol, X., Alastuey, A., Amato, F., Gibbons, W., 2012. Natural versus anthropogenic inhalable aerosol chemistry of transboundary East Asian atmospheric outflows into western Japan. Sci. Total Environ. 424, 182–192. https://doi.org/10.1016/j.scitotenv.2012.02.060

Moreno, T., Querol, X., Alastuey, A., Gibbons, W., 2008. Identification of FCC refinery atmospheric pollution events using lanthanoid- and vanadium-bearing aerosols. Atmos. Environ. 42, 7851–7861. https://doi.org/10.1016/j.atmosenv.2008.07.013

Muller, G., 1969. Index of Geoaccumulation in Sediments of the Rhine River. Geoj. 2, 108–118.

Négrel, P., Sadeghi, M., Ladenberger, A., Reimann, C., Birke, M., 2015. Geochemical fingerprinting and source discrimination of agricultural soils at continental scale. Chem. Geol. 396, 1–15. https://doi.org/10.1016/j.chemgeo.2014.12.004

Nelson, S.W., Sommers, L.E., 1996. Total carbon, organic carbon, and organic matter. In: Sparks, D.L., et al., Eds., Methods of Soil Analysis. Part 3. Chemical Methods, SSSA Book Series No. 5, SSSA and ASA, Madison, WI 961–1010.

Nesbitt, H.W., Young, G.M., 1982. Early Proterozoic climates and plate motions inferred from major element chemistry of lutites. Nature 299, 715–717. https://doi.org/10.1038/299715a0

Noack, C.W., Dzombak, D.A., Karamalidis, A.K., 2014. Rare Earth Element Distributions and Trends in Natural Waters with a Focus on Groundwater. Environ. Sci. Technol. 48, 4317–4326. https://doi.org/10.1021/es4053895

Nozaki, Y., Zhang, J., Amakawa, H., 1997. The fractionation between Y and Ho in the marine environment. EPSL 148, 329–340. https://doi.org/10.1016/S0012-821X(97)00034-4

Ogawa, Y., Ishiyama, D., Đorđievski, S., Petrović, J., Milivojević, M., Saini-Eidukat, B., Wood, S.A., 2021. Geochemical mobility of rare earth elements (REEs) and actinides (U and Th) originating from Kusatsu acid thermal waters during neutralization and river transport: Effect of aqueous speciation on sorption onto suspended materials and fractionation among REEs and actinides. Chem. Geol. 586, 120559. https://doi.org/10.1016/j.chemgeo.2021.120559

Olmez, I., Sheffield, A.E., Gordon, G.E., Houck, J.E., Pritchett, L.C., Cooper, J.A., Dzubay, T.G., Bennett, R.L., 1988. Compositions of Particles from Selected Sources in Philadelphia for Receptor Modeling Applications. JAPCA 38, 1392–1402. https://doi.org/10.1080/08940630.1988.10466479

Ord, J.K., Getis, A., 1995. Local Spatial Autocorrelation Statistics: Distributional Issues and an Application. Geogr. Anal. 27, 286–306. https://doi.org/10.1111/j.1538-4632.1995.tb00912.x

Ordonez, A., Loredo, J., De Miguel, E., Charlesworth, S., 2003. Distribution of Heavy Metals in the Street Dusts and Soils of an Industrial City in Northern Spain. Arch. Environ. Contam. Toxicol. 44, 160–170. https://doi.org/10.1007/s00244-002-2005-6

Otero, N., Vitòria, L., Soler, A., Canals, A., 2005. Fertiliser characterisation: Major, trace and rare earth elements. Appl. Geochem. 20, 1473–1488. https://doi.org/10.1016/j.apgeochem.2005.04.002

Parkhust, D.L., Appelo, C.A.J., 1999. User's guide to PHREEQC (Version 2)--a computer program for speciation, batch-reaction, one-dimensional transport, and inverse geochemical calculations: U.S. Geological Survey Water- Resources Investigations. Report 99-4259 312.

Parzych, A., Mochnacký, S., Sobisz, Z., Kurhaluk, N., Polláková, N., 2017. Accumulation of heavy metals in needles and bark of Pinus species. Folia for. Pol., Ser. 59, 34–44. https://doi.org/10.1515/ffp-2017-0004

Pawlowsky-Glahn, V., Buccianti, A. (Eds.), 2011. Compositional Data Analysis: Theory and Applications, 1st ed. Wiley. https://doi.org/10.1002/9781119976462

Pawlowsky-Glahn, V., Egozcue, J.J., 2020. Compositional Data in Geostatistics: A Log-Ratio Based Framework to Analyze Regionalized Compositions. Math. Geosci. 52, 1067–1084. https://doi.org/10.1007/s11004-020-09873-2

Pawlowsky-Glahn, V., Egozcue, J.J., Tolosana-Delgado, R., 2015. Modelling and Analysis of Compositional Data, 1st ed. Wiley. https://doi.org/10.1002/9781119003144

Pawlowsky-Glahn, V., Serra, J., Matheron, G., 2019. Matheron's Theory of Regionalised Variables, 1st ed. Oxford University Press. https://doi.org/10.1093/oso/9780198835660.001.0001

Petruzzelli, G., Pezzarossa, B., Pedron, F., 2025. The Fate of Chemical Contaminants in Soil with a View to Potential Risk to Human Health: A Review. Environments 12, 183. https://doi.org/10.3390/environments12060183

Plummer, L.N., Jones, B.F., Truesdell, A.H., 1976. WATEQF - A FORTRAN IV version of WATEQ, a computer program for calculating chemical equilibrium of natural waters (revised and reprinted january, 1984): U.S. Geological Survey Water-Resources Investigations.

Polechońska, L., Klink, A., 2023. Estimation of background concentrations of macro- and trace elements in an aquatic plant as a basis for the passive biomonitoring of pollution. Sci. Total Environ. 899, 165652. https://doi.org/10.1016/j.scitotenv.2023.165652

Punturo, R., Kern, H., Cirrincione, R., Mazzoleni, P., Pezzino, A., 2005. - P- and S-wave velocities and densities in silicate and calcite rocks from the Peloritani Mountains, Sicily (Italy): The effect of pressure, temperature and the direction of wave propagation. Tectonophysics 409, 55–72.

Qiao, P., Wang, S., Li, J., Zhao, Q., Wei, Y., Lei, M., Yang, J., Zhang, Z., 2023. Process, influencing factors, and simulation of the lateral transport of heavy metals in surface runoff in a mining area driven by rainfall: A review. Sci. Total Environ. 857, 159119. https://doi.org/10.1016/j.scitotenv.2022.159119

Qiao, Z., Zhou, L., Huang, J.Z., 2009. Sparse Linear Discriminant Analysis with Applications to High Dimensional Low Sample Size Data. IAENG Int. J. Appl. Math. 39.

Qu, S., Wu, W., Nel, W., Ji, J., 2020. The behavior of metals/metalloids during natural weathering: A systematic study of the mono-lithological watersheds in the upper Pearl River Basin, China. Science of The Total Environment 708, 134572. https://doi.org/10.1016/j.scitotenv.2019.134572

Quinn, K.A., Byrne, R.H., Schijf, J., 2004. Comparative Scavenging of Yttrium and the Rare Earth Elements in Seawater: Competitive Influences of Solution and Surface Chemistry. Aquat. Geochem. 10, 59–80. https://doi.org/10.1023/B:AQUA.0000038959.03886.60

R Core Team, 2023. R: A Language and Environment for Statistical Computing.

Ramos, S.J., Dinali, G.S., Oliveira, C., Martins, G.C., Moreira, C.G., Siqueira, J.O., Guilherme, L.R.G., 2016. Rare Earth Elements in the Soil Environment. Curr Pollution Rep 2, 28–50. https://doi.org/10.1007/s40726-016-0026-4

Razali, N.M., Eah, Y.B., 2011. Power comparisons of Shapiro-Wilk, Kolmogorov-Smirnov, Lilliefors and Anderson-Darling tests. JOSMA 2, 21–33.

Reimann, C., De Caritat, P., 2017. Establishing geochemical background variation and threshold values for 59 elements in Australian surface soil. Sci. Total Environ. 578, 633–648. https://doi.org/10.1016/j.scitotenv.2016.11.010

Reimann, C., Fabian, K., Birke, M., Filzmoser, P., Demetriades, A., Négrel, P., Oorts, K., Matschullat, J., De Caritat, P., Albanese, S., Anderson, M., Baritz, R., Batista, M.J., Bel-Ian, A., Cicchella, D., De Vivo, B., De Vos, W., Dinelli, E., Ďuriš, M., Dusza-Dobek, A., Eggen, O.A., Eklund, M., Ernsten, V., Flight, D.M.A., Forrester, S., Fügedi, U., Gilucis, A., Gosar, M., Gregorauskiene, V., De Groot, W., Gulan, A., Halamić, J., Haslinger, E., Hayoz, P., Hoogewerff, J., Hrvatovic, H., Husnjak, S., Jähne-Klingberg, F., Janik, L., Jordan, G., Kaminari, M., Kirby, J., Klos, V., Kwećko, P., Kuti, L., Ladenberger, A., Lima, A., Locutura, J., Lucivjansky, P., Mann, A., Mackovych, D., McLaughlin, M., Malyuk, B.I., Maquil, R., Meuli, R.G., Mol, G., O'Connor, P., Ottesen, R.T., Pasnieczna, A., Petersell, V., Pfleiderer, S., Poňavič, M., Prazeres, C., Radusinović, S., Rauch, U., Salpeteur, I., Scanlon, R., Schedl, A., Scheib, A., Schoeters, I., Šefčik, P., Sellersjö, E., Slaninka, I., Soriano-Disla, J.M., Šorša, A., Svrkota, R., Stafilov, T., Tarvainen, T., Tendavilov, V., Valera, P., Verougstraete, V., Vidojević, D., Zissimos, A., Zomeni, Z., Sadeghi, M., 2018. GEMAS: Establishing geochemical background and threshold for 53 chemical elements in European agricultural soil. Appl. Geochem. 88, 302–318. https://doi.org/10.1016/j.apgeochem.2017.01.021

Reimann, C., Fabian, K., Flem, B., Schilling, J., Roberts, D., Englmaier, P., 2016. Pb concentrations and isotope ratios of soil O and C horizons in Nord-Trøndelag, central Norway: Anthropogenic or natural sources? Appl. Geochem. 74, 56–66. https://doi.org/10.1016/j.apgeochem.2016.09.002

Reimann, C., Filzmoser, P., Garrett, R.G., 2005. Background and threshold: critical comparison of methods of determination. Sci. Total Environ. 346, 1–16. https://doi.org/10.1016/j.scitotenv.2004.11.023

Reimann, C., Garrett, R.G., 2005. Geochemical background—concept and reality. Sci. Total Environ. 350, 12–27. https://doi.org/10.1016/j.scitotenv.2005.01.047

Rétif, J., Zalouk-Vergnoux, A., Briant, N., Poirier, L., 2023. From geochemistry to ecotoxicology of rare earth elements in aquatic environments: Diversity and uses of normalization reference materials and anomaly calculation methods. Sci. Total Environ. 856, 158890. https://doi.org/10.1016/j.scitotenv.2022.158890

Reuter, L.R., Lado, L.R., Hengl, T., Montanarella, L., 2008. Continental-scale digital soil mapping using European soil profile data: soil pH 19, 91–102.

Rezaei, M., Sanchez-Lecuona, G., Abdolazimi, O., 2025. A Cross-Disciplinary Review of Rare Earth Elements: Deposit Types, Mineralogy, Machine Learning, Environmental Impact, and Recycling. Minerals 15, 720. https://doi.org/10.3390/min15070720

Rieuwerts, J., Farago, M., Cikrt, M., Bencko, V., 1999. Heavy metal concentrations in and round households near a secondary lead smelter. Environ Monit Assess 58, 317–335.

Riva, M.A., Lafranconi, A., D'orso, M.I., Cesana, G., 2012. Lead Poisoning: Historical Aspects of a Paradigmatic "Occupational and Environmental Disease." Saf Health Work 3, 11–16. https://doi.org/10.5491/SHAW.2012.3.1.11

Rivoirard, J., 2005. Concepts and methods of geostatistics. Space, structure, and randomness. In: Meyer F, Schmitt M (eds) Contributions in honor of Georges Matheron in the fields of geostatistics, random sets, and mathematical morphology. Springer, New York.

Rutkowski, P., Diatta, J., Konatowska, M., Andrzejewska, A., Tyburski, Ł., Przybylski, P., 2020. Geochemical Referencing of Natural Forest Contamination in Poland. Forests 11, 157. https://doi.org/10.3390/f11020157

Sadiq, M., 1997. Arsenic Chemistry in Soils: An Overview of Thermodynamic Predictions and Field Observations. Water, Air, & Soil Pollution 93, 117–136. https://doi.org/10.1023/A:1022135909197

Saiano, F., Scalenghe, R., 2019. Soil REE patterns as tracers of the emplacement of metal-rich anthropogenic materials. A case study in Moa (Cuba). JSS 19, 2777–2784. https://doi.org/10.1007/s11368-019-02283-w

Saint-Laurent, D., St-Laurent, J., Hähni, M., Ghaleb, B., Chapados, C., 2010. Using Lead Concentrations and Stable Lead Isotope Ratios to Identify Contamination Events in Alluvial Soils. Appl. Environ. Soil Sci. 2010, 1–12. https://doi.org/10.1155/2010/235210

Salminen, R., Bogatyrev, I., Chekushin, V., Glavatskikh, S.P., Gregorauskiene, V., Niskavaara, H., Selenok, L., Tenhola, M., Tomilina, O., 2004. Geochemical Baselines of Nickel and Chromium in Various Surficial Materials in the Barents Region, NW Russia and Finland. Geostandards and Geoanalytical Research 28, 333–341. https://doi.org/10.1111/j.1751-908X.2004.tb00749.x

Salminen, R., Gregorauskiene, V., 2000. Considerations regarding the definition of a geochemical baseline of elements in the surficial materials in areas differing in basic geology. Appl. Geochem. 15, 647–653. https://doi.org/10.1016/S0883-2927(99)00077-3

Salminen, R., Tarvainen, T., 1997. The problem of defining geochemical baselines. A case study of selected elements and geological materials in Finland. J. Geochem. Explor. 60, 91–98. https://doi.org/10.1016/S0375-6742(97)00028-9

Sánchez De La Campa, A.M., Moreno, T., De La Rosa, J., Alastuey, A., Querol, X., 2011. Size distribution and chemical composition of metalliferous stack emissions in the San Roque petroleum refinery complex, southern Spain. J. Hazard. Mater. 190, 713–722. https://doi.org/10.1016/j.jhazmat.2011.03.104

Santo, A.P., Jacobsen, S.B., Baker, J., 2004. Evolution and genesis of calc-alkaline magmas at Filicudi Volcano, Aeolian Arc (Southern Tyrrhenian Sea, Italy). Lithos 72, 73–96. https://doi.org/10.1016/j.lithos.2003.08.005

Santos-Francés, F., Martinez-Graña, A., Alonso Rojo, P., García Sánchez, A., 2017. Geochemical Background and Baseline Values Determination and Spatial Distribution of Heavy Metal Pollution in Soils of the Andes Mountain Range (Cajamarca-Huancavelica, Peru). IJERPH 14, 859. https://doi.org/10.3390/ijerph14080859

Sappa, G., Barbieri, M., Andrei, F., 2020. Assessment of trace elements natural enrichment in topsoil by some Italian case studies. SN Appl. Sci. 2, 1409. https://doi.org/10.1007/s42452-020-03214-y

Schwabe, A., Meyer, U., Grün, M., Voigt, K.D., Flachowsky, G., Dänicke, S., 2012. Effect of rare earth elements (REE) supplementation to diets on the carry-over into different organs and tissues of fattening bulls. Livest. Sci. 143, 5–14. https://doi.org/10.1016/j.livsci.2011.08.010

Serbula, S.M., Kalinovic, T.S., Ilic, A.A., Kalinovic, J.V., Steharnik, M.M., 2013. Assessment of Airborne Heavy Metal Pollution Using Pinus spp. and Tilia spp. Aerosol Air Qual. Res. 13, 563–573. https://doi.org/10.4209/aaqr.2012.06.0153

Shotyk, W., Weiss, D., Appleby, P.G., Cheburkin, A.K., Frei, R., Gloor, M., Kramers, J.D., Reese, S., Van Der Knaap, W.O., 1998. History of Atmospheric Lead Deposition Since 12,370^{14} C yr BP from a Peat Bog, Jura Mountains, Switzerland. Science 281, 1635–1640. https://doi.org/10.1126/science.281.5383.1635

Siebert, C., Möller, P., Magri, F., Shalev, E., Rosenthal, E., Al-Raggad, M., Rödiger, T., 2019. Applying Rare Earth Elements, Uranium, and^{87} Sr/^{86} Sr to Disentangle Structurally Forced Confluence of Regional Groundwater Resources: The Case of the Lower Yarmouk Gorge. Geofluids 2019, 1–21. https://doi.org/10.1155/2019/6727681

Siebert, C., Rosenthal, E., Möller, P., Rödiger, T., Meiler, M., 2012. The hydrochemical identification of groundwater flowing to the Bet She'an-Harod multiaquifer system (Lower Jordan Valley) by rare earth elements, yttrium, stable isotopes (H, O) and Tritium. Appl. Geochem. 27, 703–714. https://doi.org/10.1016/j.apgeochem.2011.11.011

Sierra, C., Ordóñez, C., Saavedra, A., Gallego, J.R., 2015. Element enrichment factor calculation using grain-size distribution and functional data regression. Chemosphere 119, 1192–1199. https://doi.org/10.1016/j.chemosphere.2014.10.024

Singh, A., Maichle, R., 2015. ProUCL Version 5.1 user guide.

Smedley, P.L., 1991. The geochemistry of rare earth elements in groundwater from the Carnmenellis area, southwest England. Geoch. Cosm. Act. 55, 2767–2779. https://doi.org/10.1016/0016-7037(91)90443-9

Soetan, K.O., Olaiya, C.O., Oyewole, O.E., 2010. The importance of mineral elements for humans, domestic animals and plants - A review. Afr J Food Sci 4, 200–222.

Sousa, T.A., Venancio, I.M., Marques, E.D., Figueiredo, T.S., Nascimento, R.A., Smoak, J.M., Albuquerque, A.L.S., Valeriano, C.M., Silva-Filho, E.V., 2022. REE Anomalies Changes in Bottom Sediments Applied in the Western Equatorial Atlantic Since the Last Interglacial. Front. Mar. Sci. 9, 846976. https://doi.org/10.3389/fmars.2022.846976

Storer, D.A., 1984. A simple high sample volume ashing procedure for determining soil organic matter. Commun Soil Sci Plant Anal 15, 759–772.

Sturges, W.T., Barrie, L.A., 1987. Lead 206/207 isotope ratios in the atmosphere of North America as tracers of US and Canadian emissions. Nature 329, 144–146. https://doi.org/10.1038/329144a0

Suresh, G., Sutharsan, P., Ramasamy, V., Venkatachalapathy, R., 2012. Assessment of spatial distribution and potential ecological risk of the heavy metals in relation to granulometric contents of Veeranam lake sediments, India. Ecotoxicol. Environ. Saf. 84, 117–124. https://doi.org/10.1016/j.ecoenv.2012.06.027

Sutherland, R. 2000. Bed sediment-associated trace metals in an urban stream, Oahu, Hawaii. Environ. Geol. 39, 611–627. https://doi.org/10.1007/s002540050473

Świsłowski, P., Kříž, J., Rajfur, M., 2020. The Use of Bark in Biomonitoring Heavy Metal Pollution of Forest Areas on the Example of Selected Areas in Poland. ECE S 27, 195–210. https://doi.org/10.2478/eces-2020-0013

Tack, F.M.G., Vanhaesebroeck, T., Verloo, M.G., Van Rompaey, K., Van Ranst, E., 2005. Mercury baseline levels in Flemish soils (Belgium). Environ. Pollut. 134, 173–179. https://doi.org/10.1016/j.envpol.2004.05.031

Tang, J., Johannesson, K.H., 2010. Rare earth elements adsorption onto Carrizo sand: Influence of strong solution complexation. Chem. Geol. 279, 120–133. https://doi.org/10.1016/j.chemgeo.2010.10.011

Tarvainen, T., Paukola, T., 1998. Use of geochemical databases to delineate risk areas for contaminated groundwater. J. Geochem. Explor. 64, 177–184. https://doi.org/10.1016/S0375-6742(98)00031-4

Taylor, S.R., McLennan, S.M., 1985. The continental crust: its composition and evolution: an examination of the geochem. record preserved in sedimentary rocks, Geoscience texts. Blackwell, Oxford.

Tian, X., Song, Y., Shen, Z., Zhou, Y., Wang, K., Jin, X., Han, Z., Liu, T., 2020. A comprehensive review on toxic petrochemical wastewater pretreatment and advanced treatment. J. Clean. Prod. 245, 118692. https://doi.org/10.1016/j.jclepro.2019.118692

Tipping, E., Lofts, S., Lawlor, A., 1998. Modelling the chemical speciation of trace metals in the surface waters of the Humber system. Sci. Total Environ. 210–211, 63–77. https://doi.org/10.1016/S0048-9697(98)00045-X

Tirumalesh, K., Ramakumar, K.L., Chidambaram, S., Pethaperumal, S., Gursharan Singh, 2012. Rare earth elements distribution in clay zones of sedimentary formation, Pondicherry, south India. J Radioanal Nucl Chem 294, 303–308. https://doi.org/10.1007/s10967-011-1606-9

Tomlinson, D.L., Wilson, J.G., Harris, C.R., Jeffrey, D.W., 1980. Problems in the assessment of heavy-metal levels in estuaries and the formation of a pollution index. Helgolander Meeresunters 33, 566–575. https://doi.org/10.1007/BF02414780

Tortorici, L., 1982. Lineamenti geologico-strutturali dell'Arco Calabro Peloritano. SIMP 4, 927–940.

Tostevin, R., Shields, G.A., Tarbuck, G.M., He, T., Clarkson, M.O., Wood, R.A., 2016. Effective use of cerium anomalies as a redox proxy in carbonate-dominated marine settings. Chem. Geol. 438, 146–162. https://doi.org/10.1016/j.chemgeo.2016.06.027

Triolo, L., Binazzi, A., Cagnetti, P., Carconi, P., Correnti, A., De Luca, E., Di Bonito, R., Grandoni, G., Mastrantonio, M., Rosa, S., Schimberni, M., Uccelli, R., Zappa, G., 2008. Air pollution impact assessment on agroecosystem and human health characterisation in the area surrounding the industrial settlement of Milazzo (Italy): a multidisciplinary approach. Environ Monit Assess 140, 191–209. https://doi.org/10.1007/s10661-007-9859-z

Turkyilmaz, A., Sevik, H., Cetin, M., 2018. The use of perennial needles as biomonitors for recently accumulated heavy metals. Landscape Ecol Eng 14, 115–120. https://doi.org/10.1007/s11355-017-0335-9

Turner, D.R., Knox, S., Penedo, F., Titley, J.G., Hamilton-Taylor, J., Kelly, M., Williams, G.L., 1991. Surface Complexation Modelling of Plutonium Adsorption on Sediments of the Esk Estuary, Cumbria, in: Kershaw, P.J., Woodhead, D.S. (Eds.), Radionuclides in the Study of Marine Processes. Springer Netherlands, Dordrecht, pp. 165–174. https://doi.org/10.1007/978-94-011-3686-0_18

Tweed, S.O., Weaver, T.R., Cartwright, I., Schaefer, B., 2006. Behavior of rare earth elements in groundwater during flow and mixing in fractured rock aquifers: An example from the Dandenong Ranges, southeast Australia. Chem. Geol. 234, 291–307. https://doi.org/10.1016/j.chemgeo.2006.05.006

USDA, 2017. USDA - United States Department of Agriculture, n.d USDA - United States Department of Agriculture. Soil Survey Manual. 2017. Handbook No. 18.

USEPA, 2024. National Primary Drinking Water Regulations. USEPA: Washington, DC, USA.

USEPA, U.S.E.P.A., 1995. Technical Factsheet on: NICKEL.

Van Den Boogaart, K.G., Tolosana-Delgado, R., 2013. Analyzing Compositional Data with R. Springer Berlin Heidelberg, Berlin, Heidelberg. https://doi.org/10.1007/978-3-642-36809-7

Varrica, D., Lo Medico, F., Zuccolini, M.V., Miola, M., Alaimo, M.G., 2024. Geochemical baseline values determination and spatial distribution of trace elements in topsoils: An application in Sicily region (Italy). Science of The Total Environment 955, 176951. https://doi.org/10.1016/j.scitotenv.2024.176951

Veysseyre, A.M., Bollhöfer, A.F., Rosman, K.J.R., Ferrari, C.P., Boutron, C.F., 2001. Tracing the Origin of Pollution in French Alpine Snow and Aerosols Using Lead Isotopic Ratios. Environ. Sci. Technol. 35, 4463–4469. https://doi.org/10.1021/es0105717

Violante, A., Cozzolino, V., Perelomov, L., Caporale, A.G., Pigna, M., 2010. Mobility and bioavailability of heavy metals and metalloids in soil environments. J. Soil Sci. Plant Nutr. 10. https://doi.org/10.4067/S0718-95162010000100005

Wang, M., Zheng, Q., Shen, Q., Guo, S., 2013. The Critical Role of Potassium in Plant Stress Response. IJMS 14, 7370–7390. https://doi.org/10.3390/ijms14047370

Wang, X., Zhang, Q., Zhou, G., 2007. National-Scale Geochemical Mapping Projects in China. Geostandard Geoanalytic Res 31, 311–320. https://doi.org/10.1111/j.1751-908X.2007.00128.x

Wei, C., Wen, H., 2012. Geochemical baselines of heavy metals in the sediments of two large freshwater lakes in China: implications for contamination character and history. Environ Geochem Health 34, 737–748. https://doi.org/10.1007/s10653-012-9492-9

Wei, S., Liu, F., Zhang, W., Zhang, H., Zhao, J., Liao, Y., Yan, X., 2022. Typical geothermal waters in the Ganzi–Litang fault, western Sichuan, China: hydrochemical processes and the geochemical characteristics of rare-earth elements. Environ Earth Sci 81, 538. https://doi.org/10.1007/s12665-022-10652-x

Wilkin, R.T., Lee, T.R., Ludwig, R.D., Wadler, C., Brandon, W., Mueller, B., Davis, E., Luce, D., Edwards, T., 2021. Rare-Earth Elements as Natural Tracers for In Situ Remediation of Groundwater. Environ. Sci. Technol. 55, 1251–1259. https://doi.org/10.1021/acs.est.0c06113

Willis, S.S., Johannesson, K.H., 2011. Controls on the geochemistry of rare earth elements in sediments and groundwaters of the Aquia aquifer, Maryland, USA. Chem. Geol. 285, 32–49. https://doi.org/10.1016/j.chemgeo.2011.02.020

Wood, S.A., Gammons, C.H., Parker, S.R., 2006. The behavior of rare earth elements in naturally and anthropogenically acidified waters. J. Alloys Compd. 418, 161–165. https://doi.org/10.1016/j.jallcom.2005.07.082

World Health Organization, 2017. Guidelines for drinking-water quality: fourth edition incorporating first addendum, 4th ed + 1st add. ed. World Health Organization, Geneva.

Worrall, F., Pearson, D.G., 2001. The development of acidic groundwaters in coal-bearing strata: Part I. Rare earth element fingerprinting. Appl. Geochem. 16, 1465–1480. https://doi.org/10.1016/S0883-2927(01)00018-X

Wysocka, I.A., Rogowska, A.M., Kostrz-Sikora, P., 2023. Investigation of anthropogenic gadolinium in tap water of polish cities: Gdańsk, Kraków, Warszawa, and Wrocław. Environ. Pollut. 323, 121289. https://doi.org/10.1016/j.envpol.2023.121289

Xu, D., Shen, Z., Dou, C., Dou, Z., Li, Y., Gao, Y., Sun, Q., 2022. Effects of soil properties on heavy metal bioavailability and accumulation in crop grains under different farmland use patterns. Sci Rep 12, 9211. https://doi.org/10.1038/s41598-022-13140-1

Xu, R., 2008. Progress in nanoparticles characterization: Sizing and zeta potential measurement. Particuology 6, 112–115. https://doi.org/10.1016/j.partic.2007.12.002

Yamamoto, J.K., 2005. Correcting the Smoothing Effect of Ordinary Kriging Estimates. Math Geol 37, 69–94. https://doi.org/10.1007/s11004-005-8748-7

Yan, Z., Liu, G., Sun, R., Tang, Q., Wu, D., Wu, B., Zhou, C., 2013. Geochemistry of rare earth elements in groundwater from the Taiyuan Formation limestone aquifer in the Wolonghu Coal Mine, Anhui province, China. J. Geochem. Explor. 135, 54–62. https://doi.org/10.1016/j.gexplo.2012.11.011

Yi, L., Gao, B., Liu, H., Zhang, Y., Du, C., Li, Y., 2020. Characteristics and Assessment of Toxic Metal Contamination in Surface Water and Sediments Near a Uranium Mining Area. IJERPH 17, 548. https://doi.org/10.3390/ijerph17020548

Yongming, H., Peixuan, D., Junji, C., Posmentier, E., 2006. Multivariate analysis of heavy metal contamination in urban dusts of Xi'an, Central China. Sci. Total Environ. 355, 176–186. https://doi.org/10.1016/j.scitotenv.2005.02.026

Zalasiewicz, J., Waters, C.N., Ellis, E.C., Head, M.J., Vidas, D., Steffen, W., Thomas, J.A., Horn, E., Summerhayes, C.P., Leinfelder, R., McNeill, J.R., Gałuszka, A., Williams, M., Barnosky, A.D., Richter, D.D.B., Gibbard, P.L., Syvitski, J., Jeandel, C., Cearreta, A., Cundy, A.B., Fairchild, I.J., Rose, N.L., Ivar Do Sul, J.A., Shotyk, W., Turner, S., Wagreich, M., Zinke, J., 2021. The Anthropocene: Comparing Its Meaning in Geology (Chronostratigraphy) with Conceptual Approaches Arising in Other Disciplines. Earth's Future 9, e2020EF001896. https://doi.org/10.1029/2020EF001896

Zeiner, M., Juranović Cindrić, I., 2021. Accumulation of Major, Minor and Trace Elements in Pine Needles (Pinus nigra) in Vienna (Austria). Molecules 26, 3318. https://doi.org/10.3390/molecules26113318

Zhang, F.-S., Yamasaki, S., Kimura, K., 2001. Rare earth element content in various waste ashes and the potential risk to Japanese soils. Environ. Int. 27, 393–398. https://doi.org/10.1016/S0160-4120(01)00097-6

Zhang, Y.-Y., Wu, W., Liu, H., 2019. Factors affecting variations of soil pH in different horizons in hilly regions. PLoS ONE 14, e0218563. https://doi.org/10.1371/journal.pone.0218563

Zsigmond, A.R., Száraz, A., Urák, I., 2021. Macro and trace elements in the black pine needles as inorganic indicators of urban traffic emissions. Environ. Pollut. 291, 118228. https://doi.org/10.1016/j.envpol.2021.118228